Development and scale-up design of a microchannel Fischer-Tropsch synthesis reactor for synthetic fuel production from biomass synthesis gas

A thesis submitted for the degree of

Master of Engineering

in Chemical and Process Engineering

Benjamin Graham

University of Canterbury

Christchurch, NZ

2016

Abstract

Today's society has become reliant of fossil energy based transportation fuels which are unsustainable and produce significant amounts of pollutants. With diminishing fossil energy reserves, an increased focus on renewable energy and growing fuel demands an alternative is required. A potential solution to this is to use a small scale Fischer-Tropsch synthesis system to produce hydrocarbon fuels as part of a biomass to liquids process.

This research investigated various cobalt catalyst formations and Fischer-Tropsch reactor designs to identify the most suitable combination to for a small scale system to convert 10 $SL \cdot min^{-1}$ of synthesis gas to hydrocarbons. Catalysts were created using washcoating, electrochemical deposition and solution combustion synthesis methods and tested in one or both of the two reactor designs. The first reactor design utilised a 2 mm x 20 mm channel which held a catalyst support structure made from wire mesh or metal foam which also created microchannel type flow spaces. The second reactor design consisted of various numbers of 0.3-3 mm wide wire-cut microchannels in a thin stainless steel shim plate.

Catalysts formed in the first reactor design using washcoating or solution combustion synthesis methods were found to agglomerate forming large particles which presented no detectable activity for the Fischer-Tropsch synthesis. Forming the catalysts for this reactor ex-situ using electrochemical deposition was successful in producing fine microstructures of catalyst which were initially active for the reaction. This activity did not last however with a complete loss after a few hours on stream.

Using the microchannel reactor design, the results were much more successful. Micro-structured catalysts were able to be created using both the washcoating and solution combustion synthesis methods. However for wider channels only the solution combustion synthesis method could produce suitable catalysts with 0.9 mm found to be the optimum channel width. The solution combustion synthesis catalyst achieved a higher average CO conversions of 40±2% than the washcoat (20±3%) when run in Fischer-Tropsch synthesis conditions. Analysing the hydrocarbon product from the solution combustion synthesis catalyst run yielded an ASF α value of 0.795 and a C_5+ selectivity of 73% which are very comparable to the literature. This combination was utilised to design a larger system which with the addition of a heat exchange system can be scaled up to run in the biomass to liquids system.

Acknowledgements

There a number of people who deserve thanks for their contributions without which this project would not have been a success.

Firstly thanks should go to Professor Shusheng Pang of the University of Canterbury and the Ministry of Business, Innovation and Employment (MBIE) who provided the scholarship and funding which made this project possible.

I would like to thank my supervisors, Chris Williamson, Chris Penniall and Aaron Marshall who provided valuable input and advice at various stages of the project. This helped to keep me on the right track to success. The technical staff of the department of Chemical and Process Engineering who provided fantastic assistance with making and operating equipment. Also Mike Flaws from the department of Mechanical Engineering for his help with the Scanning Electron Microscopy.

Finally, my wife Lisa, my parents and family who have supported and encouraged me throughout.

Table of Contents

List of Figures

List of Tables

1.0. Introduction

The fossil energy sources: coal, oil and natural gas have been used for a long time to provide fuels for heating, electricity generation and transportation. While this has been the way for several generations, today's society faces a challenge with both declining reserves and discoveries of these sources and the associated pollution problems created by their use. The first two categories, heating and electricity generation, can both be managed utilising existing technologies for the sustainable generation of electricity paired with electrical heating. The third category is the one in need of attention as there are few methods currently in commercial practice capable of producing easy-to-use transportation fuels. While substantial research efforts are being made towards futuristic technologies such as hydrogen fuel cells and high capacity, long-life batteries, these cannot meet the requirements today. So while the demand for transportation fuels continues to grow, a question remains as to what society can utilise in the short term.

The answer may lie in what is a relatively old technology, the Fischer-Tropsch synthesis, a process which converts synthesis gas (CO and H_2) into high purity hydrocarbons. This technology has existed for around 90 years and is its use and modification throughout the years is well documented in the literature. While all of the current commercial scale applications of the Fischer-Tropsch technology in operation utilise coal or natural gas for their feedstock, a solution to the sustainability problem can be found by using biomass. The resulting biomass-to-liquids (BTL) process can be carbon neutral, and can produce high quality liquid fuels from the Fischer-Tropsch synthesis products. These fuels are clean burning due to the high purity and can be used directly in unmodified engine systems unlike other biomass liquids such as pyrolysis crop oils.

This leads to the focus of this study, developing a Fischer-Tropsch synthesis reactor suitable for a small scale BTL plant, rather than an industrial scale coal or natural gas based facility. It forms part of the biomass to syngas and liquids (BTSL) research programme at the University of Canterbury who are investigating processes for the conversion of biomass to liquid fuels. The target scale of this project is defined by the upstream operations form the BTSL studies, primarily the synthesis gas generation using a dual-fluidised bed gassifier system [1, 2]. Previously the Fischer-Tropsch reactor system was considered by Penniall who developed a microchannel reactor design and proved its viability using a techno-economic analysis [3]. The scale of the reactor system developed by Penniall is too small and therefore it must be scaled up in order to reach the desired 10 $SL \cdot min^{-1}$ of synthesis gas to run on-stream with the gasifier.

Progressing on from Penniall's work, three goals were identified to move forward with the reactor design through the scale-up process to reach the desired size to operate on-stream with the gassifier:

1. Identify the best formation method for the cobalt catalyst in the microchannel reactor in order to obtain high synthesis gas conversion and product selectivity
2. Identify the best reactor design/support structure for the cobalt catalyst
3. Using the combined findings from goals 1 and 2, design an appropriate scale reactor system to process the nominal 10 $SL \cdot min^{-1}$ of synthesis gas from the gasifier.

After reviewing the literature on the reactors, catalysts and other influences on the Fischer-Tropsch synthesis, this thesis will present the progression through solving the problems behind these goals. Beginning with the recommended design from Penniall's work, the first goal around catalyst production is investigated. The produced catalysts are compared to those produced in Penniall's original design and published in the literature [3]. Continuing onward, the second goal targets the optimal design of the reactor. It is quite apparent that the two goals are interrelated and therefore needed they are best solved simultaneously. Once the catalysts and the performance of the systems have been compared, the best combination of design and catalyst formation is selected to move onto the third goal. There the scale-up of the design is considered ensuring that the properties attained in the initial scale are able to be retained in a larger scale design. To aid with the third goal numerical modelling of the system is used to allow the system to be quickly compared in a variety of conditions.

2.0. A Brief History of the Fischer-Tropsch Synthesis

The Fischer-Tropsch synthesis has a rich and detailed history with many contributors to its technology and attempts to demonstrate commercial activity all over the world. A brief description of the key developments of the Fischer-Tropsch technology are presented here while more comprehensive details on its history can be found throughout the literature [4-9]. The process for synthesising hydrocarbons was developed by Prof. Franz Fischer and Dr. Hans Tropsch whilst working at the Kaiser Wilhelm Institute for Coal Research (now the Max Planck Institute) in 1920's Germany. That process of catalytically reacting a mixture of carbon monoxide and hydrogen to create hydrocarbon chains is now known as the Fischer-Tropsch synthesis.

Early German systems were very simple packed bed reactors (Section 4.1) which ran at atmospheric to medium pressure (<20 atm) and low temperature (180-220 °C). Atmospheric reactors simply had cobalt catalyst loaded into a box with cooling tubes for temperature control. Despite its simplicity this a version of design was commercialised by Ruhrchemie in 1935 [4, 9]. These led to the development of multi-tubular fixed bed (MTFB) reactors, utilising Fischer and Pichler's "cobalt medium pressure synthesis", which formed the basis of the German synthetic fuels program during WWII [4, 7-9]. Fischer and Pichler also developed the "iron medium pressure synthesis" using a fused iron catalyst also in a MTFB reactor which was commercialised by Sasol in 1955 [4]. Similar technology using modern supported cobalt catalysts is used in Shell's Bintulu, Malaysia and "Pearl", Qatar plants which have been operating since 1993 and 2011 respectively [4, 7, 9].

After World War II the German synthetic fuels technology was investigated internationally, particularly in the United States. There, Hydrocarbon Research Inc. developed a new American version of the Fischer-Tropsch synthesis called the "hydrocol" process which was used commercially at Brownsville, Texas from 1951-57 [4, 7, 9]. This plant used newly developed fixed fluidised bed reactors operating at 340 °C with an iron catalyst and was the first usage of the iron high-temperature Fischer-Tropsch (Fe-HTFT) synthesis. The plant was shut down when the oil price dropped making it uneconomic to produce fuels from natural gas [4, 5, 9].

M.W. Kellogg Company later developed circulating fluidised bed (CFB) reactors to overcome difficulties with the "hydrocol" process [4, 5]. These new reactors were chosen to operate alongside the Arge reactors at Sasol 1 in 1955. Further improvements at Sasol lead to the Synthol reactors which were installed at Sasol Synfuels from 1979-1982 [4, 6, 9]. The same Synthol CFB reactors were also commissioned at the PetroSA complex at Mossel Bay, South Africa in 1992.

Over the years, Sasol has continued to contribute technological developments including the Sasol advanced synthol (SAS) fixed fluidised bed (FFB) reactors and the Sasol slurry phase reactors (SSBP and SPD). Today new SAS reactors remain in use having replace the CFB reactors at Sasol synfuels in the late 1990's [4, 9]. The first commercial SSBP slurry phase reactor commissioned in 1993 at Sasol remains in operation along with advanced SPD reactors used at the "Oryx" plant in Qatar and Escravos facility in Nigeria which began operation in 2007 and 2014 respectively [4, 9].

3.0. Synthesis Gas Preparation

A key element of the Fischer-Tropsch synthesis is the feedstock, synthesis gas which can be produced from a variety of sources provided they are carbon rich. The choice of feedstock has traditionally been dependent on local availability and low cost of the starting resource. Three types of material are used for Fischer-Tropsch synthesis gas: coal, natural gas and biomass, each with its own preparation technique(s). The preparation varies depending on the feedstock due to the different composition characteristics of each source. A brief description of the conversion of each feedstock is given in Sections 3.1–3.3 with gas contaminant removal in Section 3.4. More comprehensive descriptions and of the conversion processes can be found in the literature [1, 2, 10, 11].

3.1. Coal to Synthesis Gas

The most commonly used feedstock through the history of the Fischer-Tropsch synthesis has been coal derived synthesis gas, forming a coal-to-liquids (CTL) process. Coal derived synthesis gas was the feedstock for the original German Fischer-Tropsch plants during World War II. Fischer-Tropsch based CTL processes have been used by Sasol in South Africa since the 1950's [4], by Linc Energy in Queensland, Australia [12] and in trials by some US states looking to increase profits from low grade coal.

Conversion of coal to synthesis gas is most commonly done by means of gasification. This is the partial oxidation of coal in an oxidant (usually oxygen) and steam mixture to yield a gas containing: H_2, CO, CO_2 and CH_4. The reaction chemistry is complex, however details from studies on different types of gasifiers and coal mixtures can be found in the literature [10]. Coal gasification has been used for over a century for: town-gas production, combined-cycle electricity generation, fuel synthesis and chemical production and remains common today.

Advantages of coal gasification include: the availability of coal, high feedstock density (for economical transportation to CTL site) and an abundance of known technology. A weakness of coal is its high contaminant content (Table 3.1) of nitrogen and sulphur compounds which are known Fischer-Tropsch catalyst poisons and thus undesirable in the synthesis gas. Coal is also a fossil carbon source so eventually will become subject to the same unsustainability problems as oil.

Table 3.1: Typical mass composition for different coals [11], pine [13] and woody biomass [1].

MATERIAL (Coals by Grade)	**PROXIMATE ANALYSIS** (% mass*[1])				**ULTIMATE ANALYSIS** (% mass*[2])				
	Fixed Carbon	Volatiles	Water	Ash	C	H	O	N	S
Lignite	27.8	24.9	36.9	10.4	71.0	4.3	23.2	1.1	0.4
Sub-bituminous	43.6	34.7	10.5	11.2	76.4	5.6	14.9	1.7	1.4
Bituminous	45.2	32.9	7.3	14.6	81.0	5.3	10.5	1.5	1.6
Anthracite	81.8	7.7	4.5	6.0	91.8	3.6	2.5	1.4	0.7
Pine	17.2	82.5	- *[3]	0.3	49.3	6.0	44.4	<0.1	<0.1
Bio-solids	16.5	43.5	8.0	32.0	56.7	5.8	27.0	8.5	2.0
Wood Pellets	14.2	77.4	8.0	0.4	51.5	5.4	38.7	<0.2	<0.1

*[1] as arrived basis, *[2] moisture and ash free basis, *[3] proximate analysis is on dry basis

3.2. Natural Gas to Synthesis Gas

Natural gas can be reformed to synthesis gas by multiple methods of including: auto-thermal reforming (ATR), partial oxidation (POX), steam-methane reforming (SMR) and catalytic partial oxidation (CPO). Prior to reforming, the natural gas requires pretreatment to remove any sulphur compounds (e.g. H_2S) which poison downstream catalysts (S tolerances are typically <10ppb) and also any valuable heavier hydrocarbons (e.g. NGL or LPG) [10].

The simplest conversion for natural gas to synthesis gas is steam methane reforming (SMR). It is commonly used for hydrogen production as the H_2:CO ratio is typically high (>>2). The natural gas (methane) stream is reacted with steam in the catalyst filled tubes of a reactor resembling a shell and tube heat exchanger. The catalyst is usually nickel as it is cheaper than other metals with similar activity such as cobalt. Due to the high H_2:CO ratio and the large external heating required, SMR is not preferred for Fischer-Tropsch synthesis gas production.

Adiabatic oxidative reforming, including auto-thermal reforming (ATR), thermal partial oxidation (POX) and catalytic partial oxidation (CPO), is the preferred technology of producing synthesis gas for GTL. These processes are preferred as internal combustion supplies the heat to initiate the endothermic reforming and reverse water-gas shift (WGS) reactions (3.2.1 and 3.2.2). This reduces the size of the unit as no heat exchange is required. The partial combustion reaction (3.2.3) also adjusts the synthesis gas composition giving more desirable H_2:CO ratios for Fischer-Tropsch synthesis.

Gasification or partial oxidation (POX), initiates oxidation with a burner in a high temperature adiabatic reactor so that the heat of combustion is used to drive the reforming. POX in combination with secondary SMR is used to produce the synthesis gas for FTS at Shell's Bintulu, Malaysia and Pearl (Ras Laffan, Qatar) plants [9-11].

For CPO the natural gas is mixed with an oxidant before feeding to a catalyst bed. CPO typically operates very close to equilibrium conversions. ATR combines a primary POX burner section with a secondary catalytic oxidation and reforming section and has been used at many industrial scale operations in South Africa, Europe and the United States [10]. The Lurgi Combined Reforming Process, a combination of SMR and ATR is used at PetroSA's Mossgas facility [9].

Reactions in natural gas reforming [10]

3.2.1.	$CH_4 + H_2O \rightleftharpoons CO + 3\,H_2 \quad -\Delta H^{o}_{298} = -206\ kJ.mol^{-1}$	Steam Reforming
3.2.2.	$CO_2 + H_2 \rightleftharpoons CO + H_2O \quad -\Delta H^{o}_{298} = -41\ kJ.mol^{-1}$	Reverse WGS
3.2.3.	$CH_4 + \frac{3}{2}O_2 \rightarrow CO + 2\,H_2O \quad -\Delta H^{o}_{298} = +519\ kJ.mol^{-1}$	Partial Oxidation
3.2.4.	$CH_4 + 2\,O_2 \rightarrow CO_2 + 2\,H_2O \quad -\Delta H^{o}_{298} = +802\ kJ.mol^{-1}$	Oxidation

3.3. Biomass to Synthesis Gas

The third category of feedstock for synthesis gas production is biomass. The conversion is attained similarly to with coal using gasification and "wood gas" has been used since the 1900's. Different operating conditions (e.g. fluidised bed rather than fixed bed) and/or pre-treatment steps (e.g. additional drying) are applied to compensate for the change in composition. A key advantage of using biomass derived synthesis gas is the ability to have a carbon neutral fuel, where any carbon emitted during combustion is balanced by the carbon uptake during biomass growth. An additional consideration is the lower density of the biomass compared to coal. This makes it less economical to use a large centralised facility as the cost of transporting the biomass can become very high. Biomass gasification has seen a resurgence in recent years with the increased interest in renewable energy.

Several biomass gasifiers are in commercial use, although most of synthesis gas is used for purposes other than Fischer-Tropsch synthesis. These plants are located in Güssing, Austria [14]; Svenljunga, Sweden [15] and Gothenburg, Sweden [16] and primarily produce electricity and bio-natural gas. The Güssing gasification plant also has an on-site 10 $Nm{\cdot}h^{-1}$ Fischer-Tropsch demonstration plant using a slurry phase reactor. A demonstration scale dual fluidised bed gasifier is in use at the University of Canterbury and is capable of converting up to 20 $kg{\cdot}h^{-1}$ of biomass to synthesis gas. The synthesis gas produced by this system is well suited to Fischer-Tropsch synthesis as CO/H_2 ratios of up to 2.4 have been achieved [1, 2].

3.4. Gas Purification

The feedstock to synthesis gas preparation can contain high amounts of contaminants including sulphur compounds and nitrogen compounds which can influence gasification or liquefaction processes; particularly catalysts. Due to this it becomes necessary to remove the contaminants before the sections which may be influenced by them. The feedstock influences this element of the process as each unique feedstock will have a different contaminant content.

Whilst the sulphur and nitrogen content tend to be low in natural gas, the purification process must be undertaken before reforming as the same contaminants can poison both reforming and Fischer-Tropsch catalysts. Desulphurisation of natural gas is a well-known process used in all natural gas refineries, however the tolerances for Fischer-Tropsch synthesis are very sensitive so care must be taken. A brief overview of gas purification treatments is given by Aasberg-Petersen et al. [10].

For coal and biomass fed processes the purification is completed post gasification as it is easier to remove contaminants from the gas stream than the solid mass. Desulphurisation can be completed similarly to natural gas however the sulphur content can vary greatly between different feedstocks (Table 3.1) [13]. It is also desirable to remove ammonia and other nitrogen compounds which can occur in these feedstocks as they can poison the catalyst and dilute the synthesis gas.

4.0. Fischer-Tropsch Reactors

Throughout the history of the Fischer-Tropsch synthesis, many types of reactors have been used. Each choice was based on: the technology available at the time, the desired operating conditions and the product selectivity. While the selectivity is mainly controlled by the choice of catalyst (Section 5) the reactor design is important as to how well the catalyst can function by controlling things like temperature, pressure and reactant throughput. This section will look at the many types of reactor used (or being planned for use) in commercial operation including: pioneering reactors (4.1.), multi-tubular fixed bed reactors (4.2.), fluidised bed reactors (4.3.), slurry phase reactors (4.4.) and state of the art microchannel reactors (4.5). Small scale differential and tubular catalytic testing reactors which are designed to test small samples of catalyst are not designed specifically for the Fischer-Tropsch synthesis and therefore will not be considered. Each of the first four discussed reactor types has had a vast quantity of information published about the design and operation as all have been successfully operated commercially. The following are some of the many comprehensive sources of information on the design and development of the types of Fischer Tropsch reactors used in commercial practice (Sections 4.2-4.4):

- A.P. Steynberg and M.E. Dry Ed's, (2004). *Fischer-Tropsch Technology* in *Studies in Surface Science and Catalysis*, Vol 152. Elsevier-BV [4, 17, 18]
- Arno de Klerk, (2011). *Fischer-Tropsch Refining.* Wiley-VCH [9]
- Burtron H. Davis, (2005). *Fischer-Tropsch synthesis: Overview of reactor development and future potentialities*, Topics in Catalysis [5]

4.1. Pioneering Reactors

In the pioneering days of the Fischer-Tropsch synthesis in late 1920's Germany the reactors were, by modern standards, simple in design. The first commercial reactor, the "Ruhrchemie atmospheric fixed bed reactor" from 1935 consisted simply of a box, divided into sections with cooling tubes running through perpendicular to the dividers (Figure 4.1) [4, 9]. The granular catalyst (100 Co: 5 ThO_2: 8 MgO: 200 kieselghur) (see Section 6) was loaded into the box in the space around the tubes. This design may have had a simplistic approach however the most efficient cooling method for a fixed bed reactor was used. Near isothermal operation (±1°C) could be maintained by keeping the water in the cooling tubes at the correct pressure, so that any increase in temperature produced steam at the same temperature [4].

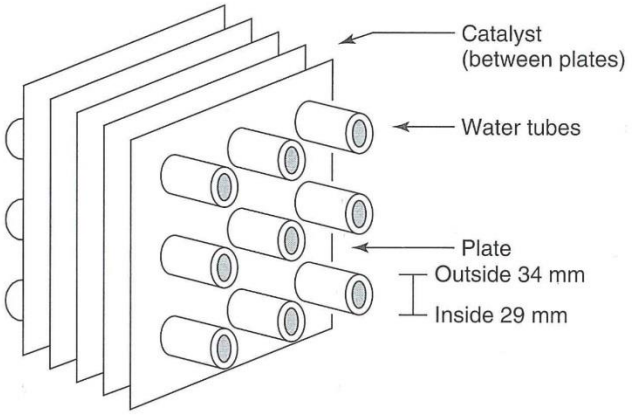

Figure 4.1: Representation of the internal structure of an early atmospheric pressure reactor showing the catalyst space, cooling tubes and dividing plates [9].

These reactors typically operated at within the 180-200°C range making them low-temperature Fischer-Tropsch (LTFT) systems. Similar technology was used in many of the Fischer-Tropsch synthesis plants built during World War II, running at both atmospheric (<0.1 MPa) and medium (0.5-1.5 MPa) pressure. Medium pressure systems utilised a different design to the atmospheric pressure reactors. The reactor design consisted of a double walled tubes inside a pressure jacket, in a similar arrangement to a shell and tube heat exchanger. The catalyst is placed in the annular space between the inner and outer tube walls and the shell side is used for the cooling (Figure 4.2). Medium pressure increased the yield of liquid and wax products and therefore became the preferred operation.

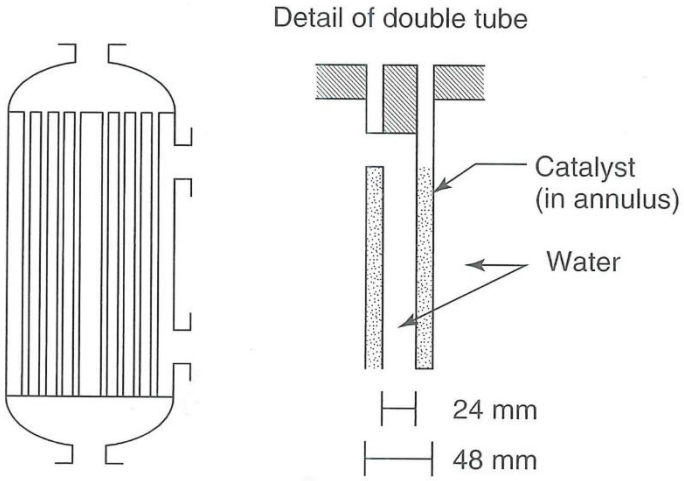

Figure 4.2: Design of medium pressure reactor used in early German LTFT plants with enlargement showing catalyst position in annulus of double-tube [9].

To achieve high conversion many of the German plants utilised 2-3 reactors in series (stages) (Figure 4.3) where after separating products and water by cooling, the outlet gas continued to a secondary stage before tail-gas treatment [9]. Normally more reactors were included in the first stage than the second, due to the higher flow.

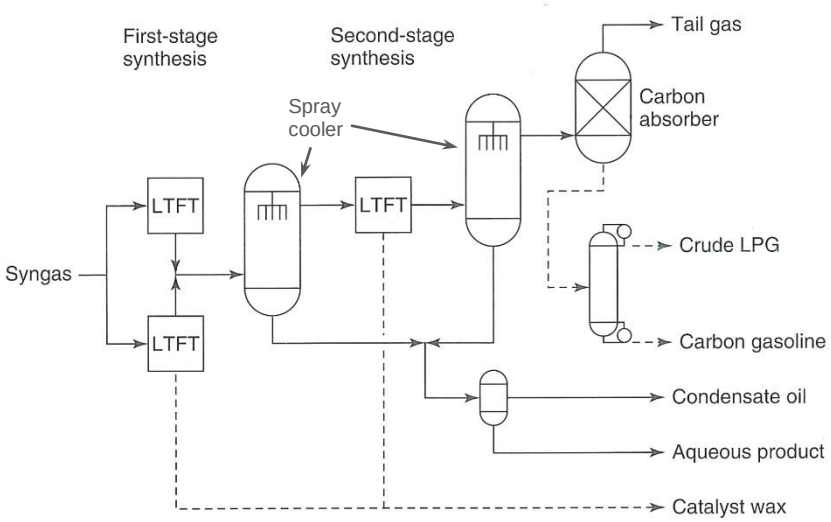

Figure 4.3: Two-Stage LTFT system as used in many of the early German plants [9]. Liquid phase product (including water) is removed by spray cooling after each stage, with the gas continuing to the subsequent stage or tail-gas treatment. Wax is periodically removed from the reactors by solvent wash or when exchanging fresh and spent catalyst.

4.2. Multi-Tubular Fixed Bed Reactors

Originating with the commercialisation of the medium pressure synthesis (Section 4.1), fixed bed reactors are the oldest style of reactors in current commercial use today. These reactors have been used at Sasol 1 in Sasolburg, South Africa and in the Shell middle-distillate synthesis (SMDS) plants in Bintulu, Malaysia and Ras Laffan, Qatar [9, 18]. The design of these reactors is typically very similar to the original medium pressure reactors with catalyst in the tubes and cooling in the shell (Figure 4.4). By making the tube diameter small, the catalyst particles are close to the wall and therefore the heat transfer is high preventing hot spots. It is normal to apply some tail gas recycle to these designs which also aids heat transfer by raising the gas flowrate [17].

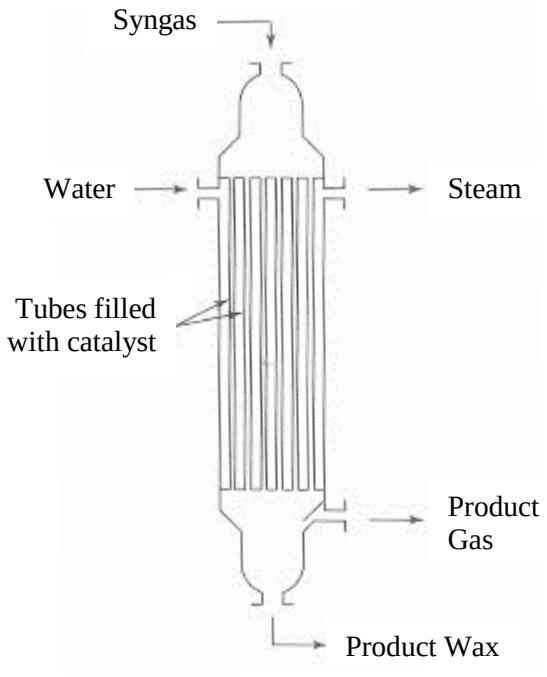

Figure 4.4: Design of a multi-tubular fixed bed reactor similar to those used at the Sasol 1, Shell Bintulu and Shell Pearl facilities [9]. Catalyst is held in the tubes and cooling water in the shell is used to generate steam which is fed back to synthesis gas production for improved efficiency. Tubes in the Sasol Arge reactors are 12 m long x 50 mm ID [19] and Shell Bintulu's reactors contain over 26000 tubes [9].

Both iron and cobalt based catalysts are used in multi-tubular fixed bed reactors with Sasol 1's Arge reactors using iron and Shell's SMDS plants utilising cobalt [9, 17]. Low temperature synthesis (LTFT) is used in these systems with the typical operating conditions summarised in Table 4.1. These reactors have a key advantage over other types in that scale up can be easily achieved as each of the thousands of tubes in the full scale reactor performs identically. This allows pilot scale experiments to be performed on a single tube with the results able to be applied directly to the full scale reactor [17]. Another advantage is that the separation of product from the catalyst is very simple as the liquid product simply trickles down and out the bottom of the bed, with no additional equipment necessary. These designs are also more resilient to damage by poisons such as H_2S than other types as the majority of the bed will be protected by the top layers [17]. Despite the many advantages, these reactors have the important drawback of not being able to replace the catalyst while the system is running resulting in periods of downtime for catalyst replacement or rejuvenation. This makes catalyst stability a priority in the development of a MTFB reactor based system in order to minimise the downtime periods. In general, these reactors have proven very successful and can be adapted to produce different products by changes in the catalyst. Provided the catalyst used has a good stability and active lifetime these reactors can provide stable, easy operation with good product yields at high CO conversions.

Table 4.1: Typical operating conditions of commercial multi-tubular fixed bed reactors [9, 17-22].

PROPERTY	SASOL 1 ARGE REACTORS	SHELL SMDS REACTORS
Temperature (°C)	200-230	200-230
Pressure (MPa)	2.5-2.7	2.5-3
Catalyst Type	Fe + K_2O	Co/Zr/SiO_2
Run Length (Days)	350+	5x 274-365
Productivity (bbl·day^{-1})	500	8000
C_{5+} Selectivity (%)	78-85	85-95

4.3. Fluidised Bed Reactors

The American Hydrocol facility was the first industrial system to use a fixed fluidised bed (FFB) reactor for the Fischer-Tropsch synthesis. It operated at 305-345 °C using a fused iron catalyst making it a high temperature synthesis (Fe-HTFT) process [19]. This represented a turning point in the evolution of the technology with the move from cobalt catalysed fixed bed reactors to iron catalysed fluidised bed reactors. Temperature control was achieved by suspending a heat exchanger in the catalyst bed to control the temperature by producing steam. Operating with a fluidised bed requires the product selectivity to be adjusted so there is no liquid phase product outside the catalyst particles, even with the elevated temperature and pressure. Liquid phase product could cause catalyst agglomeration and in turn the loss of bed fluidisation [17]. As a result of this the ASF α value for HTFT fluidised bed reactors is required to be <0.7 and the maximised range is C_5-C_{11} [9]. This was not a concern in the case of the Hydrocol facility as the aim was to produce motor gasoline (which requires mainly short chain molecules) given the oil shortage at the time.

The next evolution of the technology came with the development of the circulating fluidised bed (CFB) reactor (Figure 4.5) by the M. W. Kellogg Company in the United States. This used a similar fused iron catalyst to the Hydrocol process and was commercialised at Sasol 1 in South Africa in 1955 alongside the Arge fixed bed reactors (Section 4.2) [4, 9]. These were also high temperature synthesis processes and the 46 m tall 2.3 m diameter reactors could reliably achieve 85% conversion of CO at feed 100000 m^3·h^{-1} of syngas [19]. The three Kellogg reactors were operated successfully alongside the Arge reactors until they were decommissioned and replaced by the Sasol slurry phase reactor in 1993 (Section 4.4). These reactors were good at dealing with changes in temperature, pressure, composition and flow of the synthesis gas; the catalyst circulation rate required careful control. At low circulation rates the catalyst would block the standpipe interrupting production and at high circulation rates it would block or damage the heat exchange tubes in the reaction zone [9].

A similar CFB design was also used for the Sasol Synthol reactors installed at Sasol synfuels which began operation in the early 1980's. These remedied some of the problems found with the Kellogg design and increased the capacity from 2000 bbl·day^{-1} to 7500 bbl·day^{-1} [9]. This same reactor design with improved heat exchangers was used in the PetroSA complex at Mossel Bay, South Africa [6]. The change in feed from coal synthesis gas to reformed natural gas allowed production from a single reactor to increase to 8000 bbl·day^{-1} with identical catalyst and operation conditions [19].

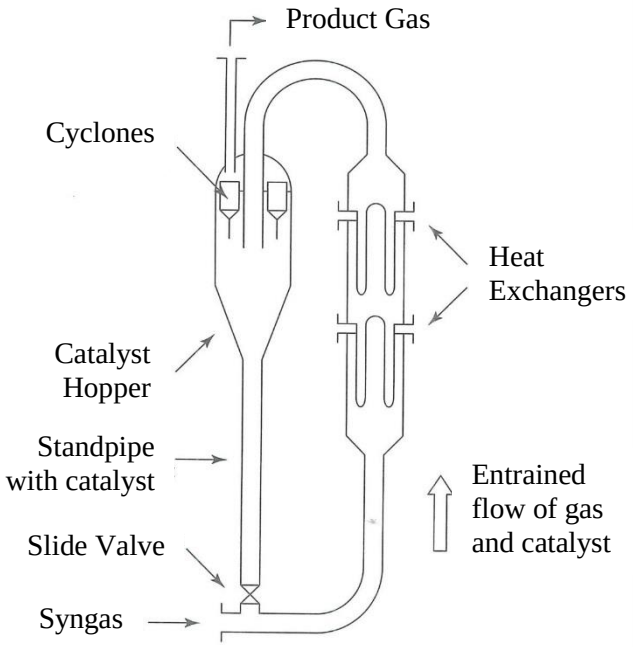

Figure 4.5: M.W. Kellogg designed CFB reactor used in the original design of Sasol 1 [9].

In the late 1990's all of the 16 Synthol CFB reactors at Sasol synfuels were replaced with new Sasol Advanced Synthol (SAS) FFB reactors (Figure 4.6) [23]. Cooling was achieved by internal heat exchange tubes running through the bed space used to generate steam, similar to the design of the Hydrocol reactors. The new SAS reactors had proven in testing to be more efficient than the Synthol CFB designs with similar product production using the same catalyst and similar conditions [Dry 1981]. The individual reactors were larger with capacities of 11000 bbl·day^{-1} and 20000 bbl·day^{-1} for 8 m and 10.7 m diameter reactors respectively [9, 23]. As a result, each of the four trains of four 7500 bbl·day^{-1} CFB reactors could be replaced by a pair (one of each size) SAS reactors without significantly adjusting the plant capacity. A comparison of the various fluidised bed reactor sizes and properties is given in Table 4.2.

The improvement from the CFB Synthol reactors to the SAS reactors comes as a result of increasing the amount of catalyst in the reaction zone at any time. The catalyst/gas ratio in the SAS reactor is about twice the amount of the CFB Synthol reactor. This occurs as less than half of the catalyst in the CFB reactors is in the reaction zone while the entirety is in the SAS reactors [17, 23]. The SAS reactors are also free of many other constraints required by the CFB reactors as outlined by Steynberg et al. [23] making them the superior choice for a new system. At an equivalent capacity, a SAS reactor also costs less than a CFB reactor as the unit is physically smaller and requires a simpler support structure. The gas velocity in the SAS reactors does not have to entrain the catalyst particles, it can be much lower. This reduces the erosion effect on the inner walls and heat exchanger tubes plus the associated maintenance is reduced [17].

A major advantage that fluidised bed designs were intended to have was the ability to exchange catalyst while the reactor was in use, preventing the downtime associated with older fixed bed designs (Section 4.2). This proved to be difficult with early designs however its applicability improved with development of the reactor designs and by the later designs of the Synthol and SAS reactors it was able to be well utilised [9]. The FFB reactors require a strict control over the catalyst particle size to ensure the correct amount of fluidisation occurs without excessive entrainment causing catalyst loss. This is not of the same importance in the CFB design where the catalyst is cycled around in the flow. The CFB reactors however require a catalyst with substantial mechanical strength as the particles are fluidised at several metres per second which can lead to excessive fines formation with a fragile catalyst. This leads to changes in the fluidisation behaviour and increases catalyst loss [23].

Table 4.2: Comparison of size and operating conditions for industrial fluidised bed reactors used at Hydrocol, Sasol and Petro SA. All systems use a fused iron catalyst promoted with one or more of K_2O, MgO or Al_2O_3 to produce a syncrude product containing mainly $C_{5\text{-}14}$ Alkenes, $C_{5\text{-}14}$ Alkanes and LPG (C_3-C_4) [9, 17, 19, 22, 23].

PROPERTY	**HYDROCOL FFB**	**SASOL**			**PETRO SA SYNTHOL**
		KELLOGG	**SYNTHOL**	**SAS**	
Temperature (°C)	305-345	290-340	330-360	340	330-360
Pressure (MPa)	2.7	1.9-2.2	2-2.5	2-4	2.5
Capacity ($bbl \cdot day^{-1}$)	-	2000	7500	11k-20k	8000
C_{5+} Selectivity (%)	≈ 68	50	51-57	57	51

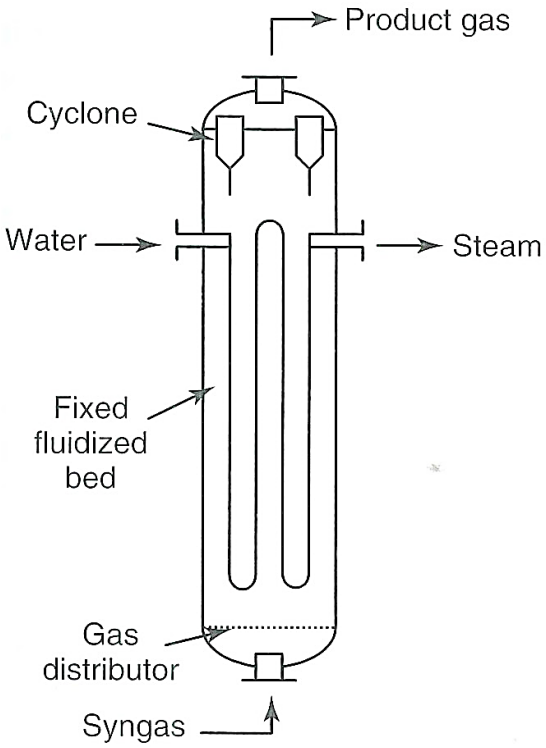

Figure 4.6: Sasol Advanced Synthol (SAS) fixed fluidised bed reactor [9]. The fluidised bed operates around the heat exchange tubing in the space between the gas distributor and the cyclones.

4.4. Slurry Phase Reactors

Slurry bubble column experiments were performed as early as the 1930's using a powdered iron catalyst suspended in oil by Fischer [7]. After additional developments in the 1950's in Germany, England and the USA, it was not until 1993 when the first commercial scale slurry phase reactor became operational at Sasol 1 [4, 5, 9, 17]. The Sasol slurry bed process (SSBP) reactor design (Figure 4.7) uses a similar precipitated Fe catalyst to the Arge (MTFB) reactors and also operates in LTFT conditions at 245 °C and 2.1 MPa [9]. In a slurry phase reactor system the solid catalyst particles are suspended in liquid-phase Fischer-Tropsch wax product and the synthesis gas is bubbled up through the wax creating a three phase system. As additional oil and wax is produced liquid phase is drawn off and solid catalyst particles are separated by filtration and returned to the reactor or exchanged with fresh catalyst. This makes the exchanging of catalyst easy with catalyst able to be continuously exchanged without having to shut-down the reactor system. Despite using the same catalyst and similar LTFT conditions the product produced by the slurry phase reactors is different to that obtained from the tubular fixed bed reactors. The amount of heavier material produced is increased compared to the tubular fixed bed reactors with an ASF α value of 0.95 and C5+ selectivity of 83.5% obtained using the SSB process. The amount of alkenes produced is also increased making the product more like the fluidised bed HTFT system product with the primary fraction being alkenes rather than alkanes [22, 24].

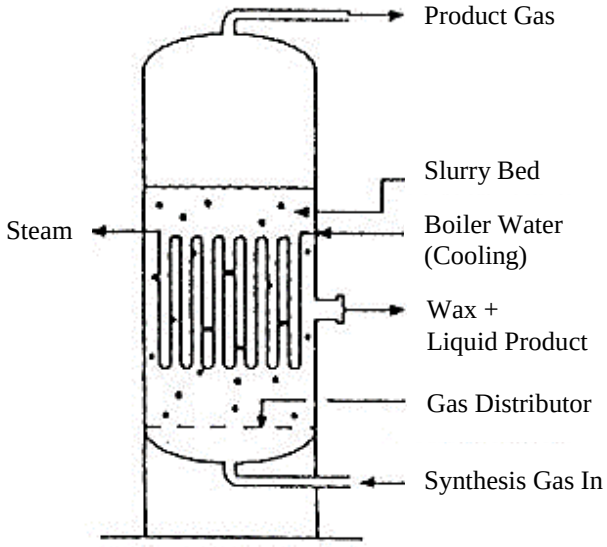

Figure 4.7: Sasol slurry phase reactor system used at Sasol 1 and the Oryx and Escravos GTL projects [6]. Catalyst is suspended in the liquid wax within the reactor forming a two-phase fluid bed which becomes a three-phase system when synthesis gas is bubbled through it.

Slurry phase systems cannot be used for HTFT as the wax forming the slurry is continually hydrocracked, requiring daily replacement, thus these reactors lead themselves to wax and chemical production rather than petrol/light liquids. While this restricts the use there are multiple advantages to using a slurry phase reactor [17]:

- The reactor train costs less than the equivalent capacity system using tubular fixed bed reactors, particularly for iron catalysts. The advantage is lesser for cobalt catalysts.
- Pressure drop is much less than a fixed bed system, often only 25%.
- Lower catalyst requirement per tonne of product than fixed bed units.
- Better heat transfer due to the liquid wax creates more isothermal conditions allowing a higher operating temperature and therefore reactant conversion.
- On-line removal and addition of catalyst can allow longer runs.

More recently slurry phase reactors have been used in the facilities for the Escravos, Nigeria and "Oryx" (Las-Raffan, Qatar) plants co-owned by Chevron Nigeria/Sasol and Qatar Petroleum/Sasol respectively. These use the same slurry reactor technology developed by Sasol which is in use at Sasol 1 in South Africa except they use a cobalt based catalyst which is more resistant to deactivation by water. The new combination is known as the Sasol slurry-phase distillate (SSPD) system. The $Co/Pt/Al_2O_3$ catalyst operates at 230 °C and 2.5 MPa [21]. The Oryx reactors are about 60 m high and 10 m in diameter making them larger than any of the previous reactors with each having a production capacity of 17000 $bbl \cdot day^{-1}$ [17].

4.5. Microchannel Reactors

Microchannel reactors are characterised by flow paths with characteristic dimensions in the 0.1-5 mm range (Figures 4.8 and 4.9) which create very high surface area to volume ratios up to 50000 m^2/m^3. The nature of the channels also provides rapid heat transfer leading to more uniform and easier to control reactor temperatures. The reduction in reactor volume also creates an inherent safety improvement by reducing the quantity of hazardous material in the system and hence the safety risk associated with the process [25]. The application of microchannel reactor technology to Fischer-Tropsch synthesis (and related reactions such as natural gas reforming) is quickly gaining popularity going from very few publications prior to 2003 to hundreds since. These publications tend to focus on one of two aspects of the microchannel system:

- Computational modelling of the gas flow and/or heat transfer in the system. [25-33]
- Catalyst creation and/or testing in the microchannels. [26, 34-48]

There are many advantages to microchannel reactors over the conventional Fischer-Tropsch reactors described in Sections 4.1-4.4. The most important of these is the improved heat and mass transfer, which can be 10-20 times higher than conventional designs [34]. As a result of this the catalyst activity, productivity and lifetime can all be improved compared to a conventional tubular reactor [39]. The smaller scale units can also be applied to smaller, localised sources of synthesis gas feedstock material such as biomass and stranded natural gas while conventional designs are optimised to run at large scales only. Microchannel reactors also present an advantage in scale-up and testing, similar to multi-tubular reactors, where a single channel or layer of channels will represent the behaviour of many identical channels used in a larger system. A comparison of reactor types is given in Table 4.3 [49].

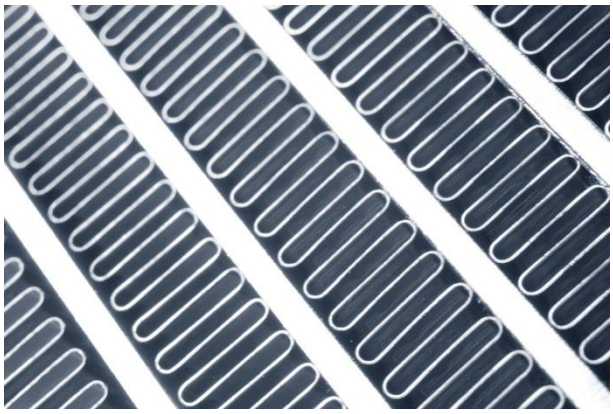

Figure 4.8: Channels in a Velocys microchannel reactor with dimensions in the 0.1-10 mm range. It is estimated that these channels are approximately 1 mm x 4 mm [49, 50].

Table 4.3: Comparison of tubular fixed bed, slurry bed and microchannel reactor types indicating their strengths and weaknesses (recreated from [49]).

Cell Colour Legend: dark grey = poor, light grey = average, white = good

PROPERTY	TUBULAR FIXED BED	SLURRY BED	VELOCYS MICROCHANNEL
Flow Patterns	Plug Flow	Well-Mixed	Plug Flow
Scale-Up Methodology	Easy	Not Well-Known	Easy
Heat Transfer Limitations	Very High	Low	Low
Mass Transfer Limitations	High	Low	Medium
Thermal Stability	Poor	Excellent	Excellent
Catalyst Reaction Rate	Low	Moderate	Very High
Volumetric Productivity	Low	Low	High
Differential Pressure (ΔP)	Moderate	Low	Moderate
Gas Recycle Requirements	High	Moderate	Low
Product-Catalyst separation	Excellent	Difficult	Excellent
Catalyst Strength Required	Low	High	Low
Regeneration Equipment	Minimal	Significant	Minimal
Regeneration Ease	Difficult	Complicated	Simple
Catalyst Replacement	Off-line, Slow	On-Stream	Off-Line, Rapid
Poisoning from Feed	Local	Global	Reasonably Local
Upset Robustness	Low	Good	High
Shutdown Robustness	Good	Poor	Excellent
Modularisation	Low	Low	High
Mass Manufacturing Economies	Low-Medium	Poor	Excellent
Required Boiler Water Quality	Low	Low	Moderate
Capital cost ($/bpd product)	High	Low (Large Scale)	Low (Distributed Plants)

While they provide many strengths, microchannel reactors present some challenges. Fabrication of the microchannels is one of these with conventional manufacturing methods often struggling at the small dimensions used in the designs. Therefore new techniques have been developed to utilise advanced technologies for the manufacture of microchannel reactors (Table 4.4). The preferred methods seem to be assembled microstructures and monolithic inserts for tubular reactors. Etching is widely used to form microstructures however most of these are in materials unsuitable for Fischer-Tropsch conditions. No publications utilising laser cut microchannels were able to be found and despite its high promise for revolutionising manufacturing 3D printed microchannels have yet to be used. Recent developments in metal/ceramic 3D printing may hold the key to unlocking this path as more durable materials can be used, making the printed structure suitable for the reaction conditions.

Table 4.4: Potential manufacturing techniques for microchannel reactors and examples utilising them for making Fischer-Tropsch and similar reactors in the literature.

MANUFACTURING TECHNIQUE	USE IN LITERATURE
Layers/plates stacked in an arrangement similar to a plate heat exchanger	[25, 30, 34, 35, 37, 38, 42, 43, 46]
Acid etching/Photolithographic etching	[31, 39, 44]
Electronic discharge machining (EDM) or wire-cutting	[3]
Monolithic structures, to form microchannels inside a larger tubular reactor	[29, 37, 38, 40, 41, 43, 45, 47, 48, 51]
Laser cutting	None Found
3D printing	Not yet applied to FT/similar reactors

The catalyst for microchannel style reactors is normally coated onto the side of the channels [25, 48], although sometimes it is loaded in as a packed bed, similar to a MTFB reactor [36, 42, 46]. This changes the types of catalyst preparation used and the nature of the catalyst (Section 5). The catalyst cannot be exchanged during operation which makes this aspect less efficient than fluidised bed designs. Recent developments have diminished this influence with high performance catalysts up to 7-15 times more active than catalysts from fixed or slurry bed reactors which are capable of long periods (>4000 h) between regeneration/replacement [34].

In terms of commercialising the technology, Velocys is leading the way. Its first commercial scale plant, a waste-to-liquids (WTL) collaboration with Waste Management, ERG energy and Ventech is under construction in Oklahoma, USA. Plans also exist for a GTL plant in Ohio, USA and a WTL plant for jet fuel in London, UK [49]. Previously a demonstration plant using the Velocys technology was installed in Güssing, Austria with the biomass gasification system [52]. Many studies have been conducted on their catalyst formation and reactor design [36, 42, 53] which have resulted in multiple patents being held for Fischer-Tropsch related technology [54-56].

5.0. Fischer-Tropsch Catalysts

Similarly to how there are multiple reactor designs and sets of operating conditions, there are multiple varieties of catalyst for the Fischer-Tropsch synthesis. Catalyst choice is influenced by many factors including the desired product type and range, reactor design, operating conditions and synthesis gas composition. Fischer-Tropsch catalysts typically consist of many components including one or more active metals, a support material and any structural or catalytic promoters used. The most common active metals are cobalt (Co) and iron (Fe) while ruthenium (Ru), nickel (Ni) and rhodium (Rh) have also been used.

Of these metals, ruthenium is the most active for the Fischer-Tropsch synthesis reaction however it is rare and consequently expensive (Table 5.1) which makes it undesirable for large scale use [57]. Despite this ruthenium has still seen considerable use as a promoter in laboratory scale experiments due to its high activity. Nickel is also a very active catalyst however it is a strong hydrogenation catalyst and therefore favours methane formation which is undesirable. It also tends to form surface carbonyls on the catalyst which cause deactivation and damage to the catalyst particles [57]. Rhodium is extremely expensive and as such has seen very limited use however those who have used it report favourable properties [58]. Excluding ruthenium and rhodium based on cost and nickel based on selectivity respectively, cobalt and iron are left as the catalysts of choice and hence there is much more literature detailing these catalysts. Ruthenium and rhodium are not forgotten however as along with many metals including rhenium (Re), platinum (Pt), potassium (K) and sodium (Na) which have been used as promoters with a cobalt or iron based catalyst.

Table 5.1: Cost comparison of common active and promoter metals used for Fischer-Tropsch catalysts with all converted to the same mass unit basis [59-62].

Catalyst Metal	**Cost ($US/kg)**
iron (Fe)	0.05
nickel (Ni)	8.60
cobalt (Co)	23.00
ruthenium (Ru)	1400.00
rhenium (Re)	2500.00
rhodium (Rh)	24000.00
platinum (Pt)	31000.00

5.1. Cobalt Based Catalysts

Cobalt based Fischer-Tropsch catalysts date back to the origins of the process in the early 1920's and were utilised in most of the German synthetic fuels plants during World War Two. Since cobalt costs considerably more than iron (Table 5.1) it is important to minimise the amount of cobalt required while maintaining a high activity. This is normally attained by generating small crystallites of Co (to maximise the active surface area per unit mass) and adding promoters such as Re, Ru, Zr or Pt [24]. Combining the desire for small Co particles and promoter addition, the best cobalt based catalysts are supported ones using a stable high surface area oxide such as Al_2O_3, SiO_2 or TiO_2 [21, 57]. Despite being small particles being desirable Fischer et al. [63] compiled some important influences that the Co particle size can have in Al_2O_3 supported Co catalysts:

- Structural effect: different crystallite sizes expose different surface sites leading to different activities and selectivities.
- Electronic effect: at different crystallite sizes the activation energy for the dissociation of H_2 is favoured over CO resulting in changes in selectivity.
- Oxidation effect: Smaller crystallites are easily re-oxidized under Fischer–Tropsch conditions leading to changes in activity due to a loss in active material.

While cobalt costs more than iron, it presents several advantages over iron as a Fischer-Tropsch catalyst. Cobalt is less active for the side water-gas shift reaction, more selective towards linear chain growth and more resistant to deactivation [64]. The Fischer-Tropsch synthesis reaction rate (Section 7) is also un-inhibited by water or CO_2 when using cobalt while it is inhibited for iron. This means that the rate for a Co catalyst will decrease less along a reactor than it will for a Fe catalyst, resulting in higher per-pass conversions [21]. Cobalt catalysts in general also deactivate more slowly than iron catalysts, which leads to fewer catalyst regenerations and replacements keeping them cost effective.

The effect of supports and promoters in these cobalt catalysts can be significant in determining the structure, activity and selectivity of the final catalyst. Despite being one of the most common support materials (Section 6), silica requires pretreatment with a non-SiO_2 layer or addition of a suitable promoter, to prevent or slow the formation of cobalt-silicate [55]. The effect of promotion by a second metal such as Re, Ru, Pt or Zr can substantially improve the reaction rate, product selectivity, activation (degree of reduction), or resistance to deactivation.

Commercially, cobalt based catalysts are in use in the Shell Bintulu plant in the form of a $Co/Zr/SiO_2$ catalyst and the Sasol/Qatar "Oryx" plant in the form of a $Co/Pt/Al_2O_3$ catalyst [20, 21]. The Shell catalyst was designed to maximise the heavier weight products formed while maintaining a high activity and long lifetime which was considered easier with Co than with iron [65]. The Sasol catalyst is said to be more productive per pass of operation due to an enhanced resistance to oxidation by the water product which is important given it is used in a slurry reactor where water removal is less rapid [21]. A supported cobalt catalyst generated by a proprietary method called the "organic matrix combustion (OMX)" is to be used in the planned joint venture plant in Oklahoma based on Velocys microchannel technology [49]. Details on the catalysts exact composition are unclear however there are several patents which suggest there is a complex mixed oxide support of titania and silica promoted with traces of rhenium and platinum [55].

5.2. Iron Based Catalysts

Iron catalysts have been used for industrial scale Fischer-Tropsch plants since the 1950's during the early days of HTFT in the USA. The use of these catalysts was later developed by Sasol in South Africa with the evolution of the high temperature CFB reactors [4, 57]. Iron catalysts require promotions with alkali (Na and K) to become useful for Fischer-Tropsch synthesis. Increasing the amount of alkali increases the amount of CO adsorbed which in turn increases the chain growth and conversion [9]. This makes promotion one of the most important elements of iron catalysts. Given that iron catalysts are mostly used in the high temperature (HTFT) synthesis which takes place in fluidised bed reactors the other important characteristic is mechanical strength. Iron catalysts require a substantial tail gas recycle to be established as the conversion is inhibited by water formation [7].This can be seen in the gas loop design used at Sasol 1 where the Kellogg CFB reactors ran with a recycle loop feeding back to the reactor and synthesis gas formation lines [9].

Advantages of iron catalysts include better operation at high temperature, a higher alkene/alkane ratio, lower average molecular weight and a lower cost for the catalyst material (Table 5.1). Weaknesses include the need for promotion with alkali to generate activity, activity for the water-gas-shift reaction and the sensitivity to water which causes de-activation [9, 57]. Therefore, iron catalysts can be beneficial to cobalt catalysts but only if run in the right conditions so that the enhanced alkene and low weight product formation can be capitalised on for chemical production.

5.3. Ruthenium, Rhodium and Nickel

Outside of cobalt and iron, there are number of metals which have been used in Fischer-Tropsch catalysts however only ruthenium, rhodium and nickel have been considered on their own. Ruthenium [66, 67] and rhodium [58] have been used in research studies however their rarity and consequently high prices (Table 5.1) prevent their use in commercial operations. Like cobalt, ruthenium catalysts are selective to longer chain products and typically operate at high α values when run at elevated pressures [68]. Very little is available about rhodium, most likely due to its cost and rarity. The study by Urquhart et al. investigated a potassium promoted Rh catalyst and found it to be effective for alcohol production in addition to the usual alkanes and alkenes.

Nickel has been studied much more however its use remains complex. It was discovered early on that it was an active catalyst for the Fischer-Tropsch synthesis. Due to producing only light hydrocarbons and kerosene which were of little value at the time (1920's/1930's) any commercialisation was abandoned and most studies shifted to Co and Fe. More recently more studies using Ni have been conducted with the aim to improve Co or Fe catalysts without utilising the expensive rare earth metals Re, Ru and Pt. The use of Ni on its own remains unfavourable due to the high methane production. A comprehensive review of the use of Ni catalysts is given by Enger and Holmen [69].

6.0 Catalyst Formation Techniques

There exists a large variety of catalyst formation techniques which can all be used to develop catalytic species for reactions. In the case of Fischer-Tropsch catalysts, the heterogeneous metallic phase is best suited to thermal and physical deposition techniques. In some situations there will be multiple techniques or repeated processes to ensure the catalyst is prepared with the desired properties. Such properties include surface area, surface structure, selectivity and durability. The focus of this section is on the most common deposition techniques for Fischer-Tropsch catalysts used in the literature and in industrial reactors. In addition techniques with a high potential for the coating of microchannel type reactors will be considered since those designs are of particular interest to this work.

6.1. Impregnation Methods

Impregnation methods are the by far the most common preparation methods used in the development of Fischer-Tropsch catalysts in the literature, with widespread use for creating supported cobalt catalysts. The most common variation, incipient wetness impregnation utilises an amount of precursor solution calculated to fill the pores of a porous support material such as silica, or alumina. The solution is mixed with the support as a slurry where the solution is adsorbed into the pores of the support material. Upon drying and calcination small particles of the desired active phase are formed inside the pores creating a well dispersed, high surface area catalyst. Since a solution is used to impregnate the pores, multiple active phases can be applied simultaneously to create a multi-metallic, promoted or doped catalyst. By correctly selecting the support material and promoters the catalyst can be tailored for use in specific conditions such as those experienced in Fischer-Tropsch reactors. Examples of the use of incipient wetness impregnation from the literature are given in Table 6.1.

6.2. Precipitation Methods

Another popular category of methods for creating Fischer-Tropsch catalysts is precipitation based formation which is most popular with iron based catalysts. There are several variants depending on the method of promoter addition and the forming of the final particles. In the simplest case, a form of the active metal (e.g. $Fe_2(CO_3)_3$) is precipitated from a solution and subsequently mixed with any promoters (e.g. K_2O) and structural support materials (e.g. Al_2O_3). The mixture is then extruded, sintered or fused before being crushed into the unreduced catalyst particles. In variations, promoters can be co-precipitated with the active metal and/or the precipitation step can occur onto the support material in a slurry. By fusing the mixture hard and durable particles of catalyst can be made. These are preferred in fluidised and circulating bed Fischer-Tropsch reactors where the stresses on the particles resulting from wall collisions are higher. An example of this is the use of fused iron catalysts in all of the commercial HTFT fluidised bed systems over the years: Hydrocol CFB, Sasol Kellogg CFB, Sasol/PetroSA Synthol CFB (also used at Petro SA) and Sasol SAS FFB [4, 9, 17].

Table 6.1: Published examples of Co Fischer-Tropsch catalysts produced by impregnation techniques.

CATALYST	APPLICATION	REFERENCES
$Co/Pt/Al_2O_3$	Sasol SPD, Research	[9, 70-72]
$Co/Zr/SiO_2$	Shell SMDS	[20]
Co/TiO_2	Research	[73, 74]
Co/Al_2O_3	Research,	[40, 71-80]
$Co/MgO/Al_2O_3$	Research	[81]
$Co/Re/Al_2O_3$	Research	[26, 43, 75-78]
$Co/Ru/Al_2O_3$	Research	[82, 83]
$Co/Ru/ZrO_2/Al_2O_3$	Research	[84]
$Co/Fe/Al_2O_3$	Research	[64]
Co/SiO_2	Research	[74, 85-92]
$Co/Ru/SiO_2$	Research	[87]
Co/Zeolite	Research	[85]
Co/bentonite	Research	[73]
Co/SiC	Research	[73, 93, 94]
Co/CNF	Research	[86]
Co/Fe/CNT	Research	[95]

In addition to being one of the most widely used commercial Fischer-Tropsch catalyst preparation methods, precipitation is also one of the oldest methods used for the Fischer-Tropsch catalyst production. Early German catalysts used in the 1930's were prepared by co-precipitation of nitrates of cobalt and thorium, or occasionally magnesium or zirconium, in the presence of kieselghur (silica). The typical component mass ratio of one of these catalysts was 100 Co:18 ThO_2:100 kieselguhr [4]. These catalysts were not mixed and extruded/fused as the modern iron catalysts are however the technique would have created a layer of precipitate particles on the surface of the silica support, ideal for exposure to the gas flow through a fixed bed. Today, a similar catalyst would most likely be produced by impregnation (Section 6.1) however the Sasol Arge tubular fixed bed reactors still use an extruded precipitated iron catalyst [21]. In the literature precipitation methods have also been examined by: Calderone et al., de Deugd et al., Fischer et al. and Morales et al. [45, 63, 96-98].

6.3. Washcoating Methods

Washcoating methods are popular for coating larger support structures (such as monoliths) with pre-prepared catalyst particles. They can also be used to directly prepare catalytic layers on the inner surfaces of microchannels, monoliths or tubular reactors. The procedure is usually very simple, after immersion in precursor solution or catalyst slurry any excess solution/slurry removed by blowing before the remaining film is dried onto the support. In the literature, washcoating has been used by Almeida et al. [43], de Deugd et al. [45], Hilmen et al. [37], Kapteijn et al. [47] and Nijhuis et al. [41] among others, primarily to coat supported catalysts prepared by impregnation onto monolithic, tubular or channel structures. Penniall [3] utilised it somewhat differently by creating the Co Fischer-Tropsch catalyst directly with the washcoat layer in microchannels. While this was a different approach it proved successful with highly active structures formed.

6.4. Combustion Synthesis Methods

One of the most promising categories of methods for preparing high surface area metallic oxide materials are the combustion synthesis methods. The self-propagating high-temperature synthesis (SHS) [cite uses], solution combustion synthesis (SCS) [cite uses] and organic matrix combustion (OMX) methods [cite uses] have all recently been applied to the preparation of catalysts or catalyst intermediates suitable for the Fischer-Tropsch synthesis. In this method the particles are produced by the combustion reaction between two different components of a salt mixture (SHS) or solution (SCS). Normally one of the components will be a metal nitrate salt as a precursor to the metal oxide with an organic fuel which reacts with the nitrate salt once ignited. Common organics used as the fuel species include amino acids, urea and organic acids such as citric acid [99]. It was found by Li et al. that the amino (NH_2) functional groups of the amino acids and urea aided in the reaction by decomposing to ammonia which in turn helped to decompose the nitrates to water and N_2 [99].

The key feature of this preparation method is that the reaction is self-sustaining providing its own heat and requiring no external heating [36, 42, 53, 99]. It has been shown that this method produces well dispersed catalysts with a small particle sizes, good structure (Figure 6.1) and high activity for the Fischer-Tropsch synthesis. The most promising aspect of the combustion synthesis methods is the use of the OMX variant for the production of Velocys catalyst used in their microchannel reactors which are now being commercialised (Section 4.5).

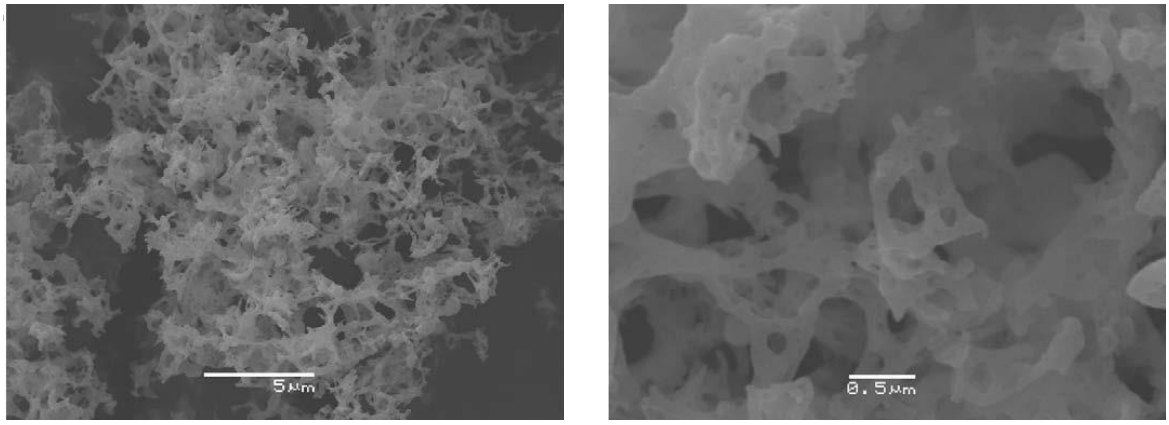

Figure 6.1: SEM images of cobalt oxide powder produced Toniolo et al. using the solution combustion synthesis method with glycine as the fuel [100].

6.5. Electrochemical Deposition Methods

The electrochemical (potentiostatic or galvanostatic) deposition of metal hydroxide thin films has been used for many applications including fuel cell electrode catalysts, battery electrodes, capacitors and passivation layers. Recently this has been adapted to produce nanostructures by using low concentrations (10^{-3}–10^{-4} mol·L^{-1}) of the metal precursor salt in solution. The formation of α-$Co(OH)_2$ films as performed by Brownson and Lévy-Clément [101] (Figure 6.2), KelpŠAitĖ et al. [102], and Gupta et al. [103, 104] shows a structure with high surface area and lots of catalytic edge sites. Provided it has the physical attributes to survive the reaction conditions such a structure would be well-suited to a Fischer-Tropsch catalyst. However based on the published literature, electrochemical deposition has not been used previously for the complete formation of Fischer-Tropsch catalysts. The closest that it has come is the electrochemical addition of alkali (Na, K) promoters to the surface of ruthenium catalysts prepared by other methods [58, 67].

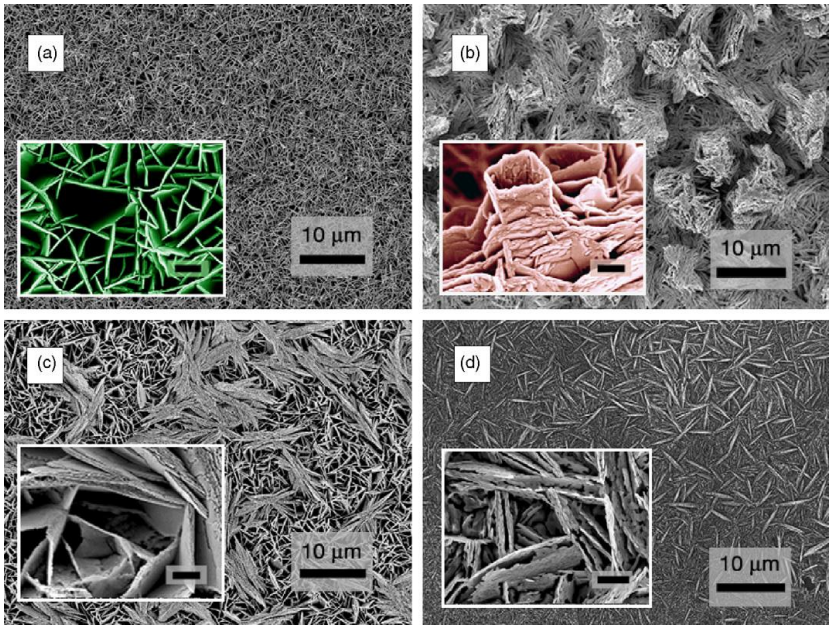

Figure 6.2: Microstructured $Co(OH)_2$ depositions created by Brownson and Lévy-Clément [101] using the electrochemical deposition technique. The area and structure of these deposits suggests potential for a Fischer-Tropsch catalyst to be created using this method.

6.7. Other Reported Formation Methods

Atomic layer deposition (ALD), freeze-drying, plasma decomposition and micro-emulsion have also been used to form the active components of Fischer-Tropsch catalysts. The cobalt catalysts produced by ALD were compared to similar catalysts produced by impregnation by Cronauer et al. [71] with the surface properties examined. ALD was found to be more effective given it can create layer-by-layer depositions although it could be difficult to apply to a large scale catalyst production (only 0.1-0.2g were tested). Eggenhuisen et al. [105] prepared a SiO_2 supported Co catalyst using freeze-drying to improve the Co particle size. By applying freeze-drying rather than conventional drying they were able to prevent particles from clustering maintaining 4-7 nm particles rather than 400 nm clusters. The plasma decomposition method used by Fu et al. [106] is complex and targets the calcination step to prevent oxidising their carbon nanotube support. Karimi et al. and Trépanier et al. [107, 108] both used micro-emulsions to apply their cobalt particles to their carbon nanotube supports to control the particle size. Overall, these techniques appear to be targeting very specific elements rather than varying the overall deposition with impregnation methods often still incorporated.

7.0. Mechanisms and Kinetics of Reactions in Fischer-Tropsch Synthesis

There are many individual reactions which occur inside a Fischer-Tropsch synthesis reactor. These reactions are all heterogeneously catalysed by the metallic catalyst. Different catalyst metals can make particular reactions or pathways more or less likely to occur. In particular, iron based Fischer-Tropsch catalysts can catalyse the water-gas-shift reaction (Section 7.3), while cobalt based ones do not. This section briefly describes the activation, mechanisms, kinetics and influence of the three most likely reactions inside a Fischer-Tropsch reactor: the hydrocarbon synthesis, water-gas-shift reaction and Boudouard reaction. The shift and Boudouard reactions are only briefly discussed for completeness and as such no mechanistic or kinetic effects were investigated for those reactions.

7.1. Mechanisms of the Fischer-Tropsch Synthesis Reaction

The target (and therefore most desirable) reaction to occur inside a Fischer-Tropsch system is the hydrocarbon synthesis reaction which can be generalised by R 7.1. In essence it is the catalytic hydrogenation of carbon monoxide to form hydrocarbon chains of the form C_nH_m and water. Many mechanisms for this reaction have been proposed over the years and there are still multiple accepted mechanisms in order to cover all of the possible products. The articles by van Santen et al. [109], Dry [6, 110], and Fontenelle and Fernandes [111] give comprehensive descriptions of the mechanisms of the Fischer-Tropsch synthesis reaction.

R 7.1 $\quad n\,CO + A\,H_2 \rightarrow C_nH_m + n\,H_2O$ Fischer-Tropsch Synthesis

In recent times surface analytical techniques have indicated that there are two pathways for molecular growth, CH_2 insertion for chain growth and CO insertion for the formation of oxygenates [110]. These pathways, the Sachtler-Biloen (CO dissociation or carbide) route and the Pichler-Schulz (CO insertion) route are described by van Santen et al. along with kinetic theory supporting each [109]. While both can support chain growth the CO insertion pathway leads to more oxygenated products which are less common and as such it will not be discussed further here. Three mechanisms are considered for chain growth. On Co catalysts, the Brady-Pettit (alkyl), Maitlis (alkenyl) and Gaube (alkyldiene) mechanisms can all be used to describe the lengthening of the hydrocarbon chain by insertion of a methylene (CH_2) unit to yield alkanes and alkenes [109, 111]. The mechanism on Fe catalysts is more complex involving iron-carbide sites which are covered elsewhere.

After the common dissociative adsorption (Figure 7.1a) and methylene formation (Figure 7.1b), the Brady-Pettit mechanism starts by the (partial) hydrogenation of a surface CH_2 to a surface methyl (CH_3) (Figure 7.2a). The subsequent insertion of adjacent CH_2 units into the metal-alkyl bond initiates (Figure 7.2b) and grows the chain length (Figure 7.2c) [109, 111]. This is the simplest mechanism and can describe the normal product distribution well with chains terminating from Figure 7.2c as either alkenes, or alkanes if hydrogenated due to the abundance of H_2 in the system.

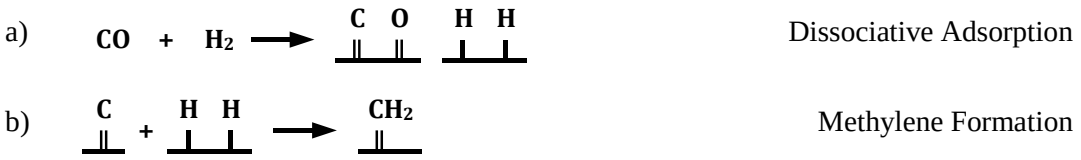

Figure 7.1: Dissociative adsorption of CO and H_2 reactants (a) and formation of methylene (CH_2) units for chain building (b) for use in all Fischer-Tropsch synthesis mechanisms.

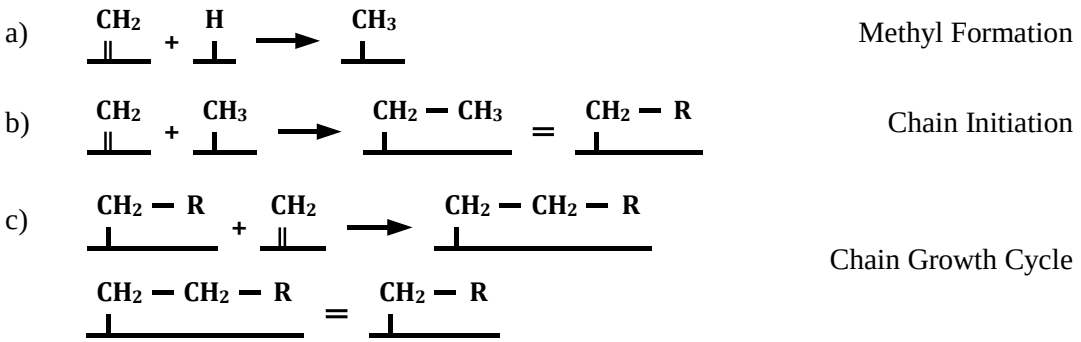

Figure 7.2: Brady-Pettit (alkyl) mechanism for chain initiation and growth in Fischer-Tropsch synthesis. Firstly a methyl group is formed (a) which combines with a CH_2 unit to form an alkyl group (b), initiating the chain. Chain growth then proceeds by the repeated insertion of CH_2 units at the base of the chain (c) until termination occurs. The surface molecule would result in an alkene however the abundance of hydrogen will result in most becoming hydrogenated to alkanes.

The Maitlis mechanism starts from an adsorbed CH_2 unit and an adsorbed CH unit. The CH_2 unit joins to the CH unit to initiate the chain (Figure 7.3a) and subsequent CH_2 units join at the base (Figure 7.3b) similarly to the Brady-Pettit mechanism to grow the chain. After a new CH_2 unit joins the molecule undergoes isomerisation (7.3c), moving the double-bond back to the end for subsequent growth steps (Figure 7.3d) [109]. It is considered by van Santen et al. [109] that the Maitlis mechanism is problematic with the intermediate species interacting too strongly with the surface and potentially forming dienes (two double bonds). In addition this mechanism does not primarily form n-alkanes which have been experimentally observed as the major products.

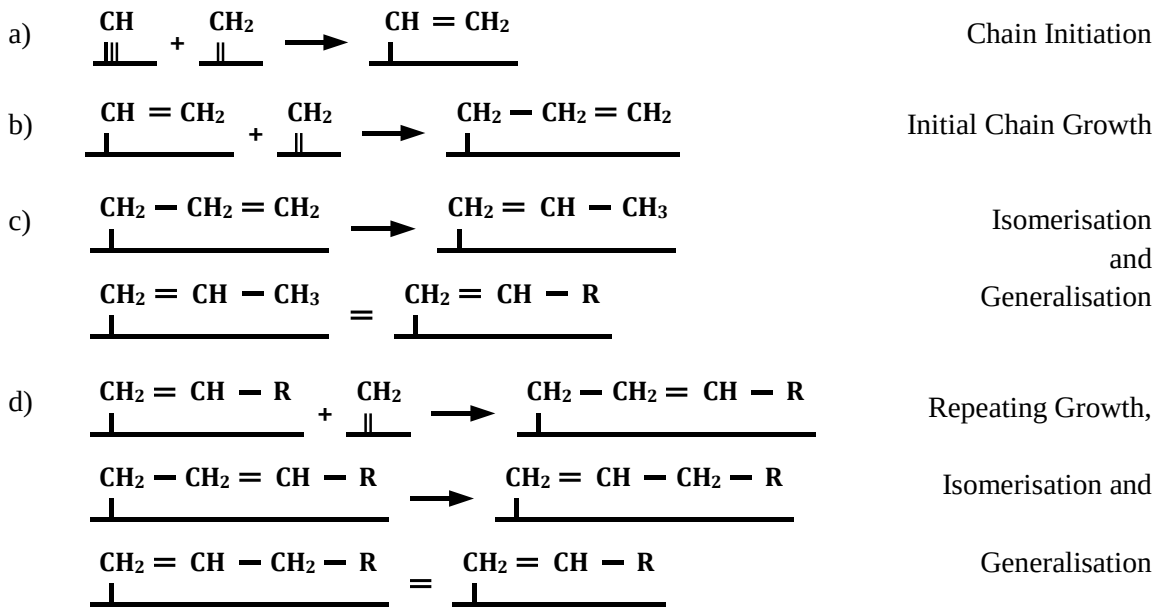

Figure 7.3: Maitlis (alkenyl) mechanism for chain growth during Fischer-Tropsch synthesis. Chain initiation (a) forms a surface alkenyl group from a CH unit and a CH_2 unit. Insertion of a CH_2 unit grows the chain (b), before isomerisation (c) moves the double bond back to the adsorbed end. Repeating the insertion and isomerisation steps lengthens the chain (d).

The Gaube mechanism is very much a variant of the Maitlis mechanism but starts with two surface CH_2 units (Figure 7.4a) which join before isomerising (Figure 7.4b) to form a CH-R unit. This CH-R unit then replaces one of the CH_2 units for subsequent insertions (Figure 7.4c) [109]. Even with this mechanism the synthesis products are predominantly linear as the insertion of CH_2 is more likely at the end without the '-R' group due to steric hindrance [110]. A similar process had been proposed by Schulz and Claeys for the continued growth of re-adsorbed olefins [111]. This olefin re-adsorption could explain the lower than expected yield of C_2 molecules (ethane/ethylene) compared to the ASF distribution. The surface C_2 molecule (Figure 7.4a) is unique as it has two equally likely ends for CH_2 insertion. This results in the rate of growth from C_2 to C_3 being much higher than the rates of desorption or hydrogenation of C_2 [110].

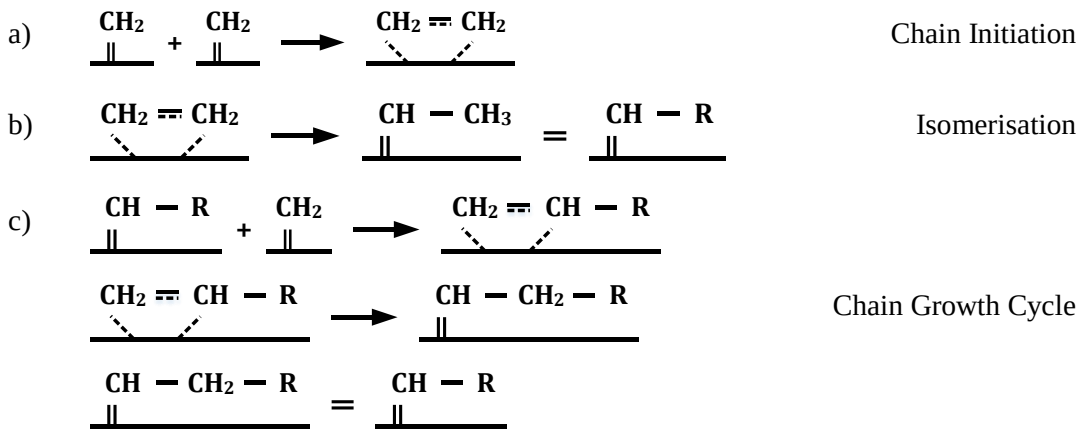

Figure 7.4: Gaube (alkyldiene) mechanism for chain growth during Fischer-Tropsch synthesis. During initiation, two CH_2 units combine to form a surface C_2 olefin (a). After isomerisation to an alkylene unit (b) this can combine with further CH_2 units to grow the chain (c).

7.2. Kinetics of the Fischer-Tropsch Synthesis Reaction

In determining the kinetic expressions a heterogeneous catalytic process there are three steps to consider: reactant adsorption, surface reactions and product desorption. For the Fischer-Tropsch synthesis this can be expanded to six steps: reactant adsorption, reactant dissociation, CH_2 formation, chain growth, chain termination and product desorption by considering the four surface phenomenon shown by the mechanisms. Fully detailed kinetic models are developed by: Fontenelle and Fernandes [111], van Santen et al. [109] and Markvoort et al. [112] using differential equation expressions to consider the propagation from one state to the next (Figure 7.5). As with any model these kinetic models come with their assumptions. Key assumptions identified by Markvoort et al. include: independent H_2 and CO chemisorption, only CH_2 as monomers and rapid desorption of O as H_2O.

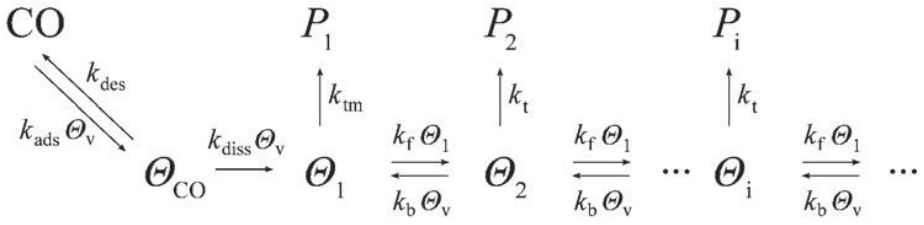

Figure 7.5: Comprehensive kinetic scheme for Fischer-Tropsch synthesis proposed by Markvoort et al. [cite]. Each arrow represents a reaction step with its own rate expression and rate constant k_x. Rate constant subscripts are: *ads* = adsorption, *des* = desorption, *diss* = dissociation, *t* = termination, *m* = methane, *f* = forward and *b* = backwards. Concentrations of adsorbed species are represented by Θ_{CO}, Θ_i and Θ_v where *i* denotes the number of carbon atoms in the species and *v* denotes vacant surface sites. The rate for the formation of CH_2 monomers from the dissociated species seems to be included in the one step here such that k_{diss} represents the kinetics for both CO dissociation and surface C hydrogenation to CH_2.

While the approach of these articles is complete and comprehensive, the more empirical approach of Yates and Satterfield for a cobalt catalyst allows for a simple and yet accurate model using a singular rate equation (Equation 7.1) [113]. This utilises only the two temperature dependent constants 'a' and 'b' representing a kinetic parameter and an adsorption co-efficient respectively. Thus an overall rate can be calculated from the reactant partial pressures of CO and H_2 in the system once 'a' and 'b' have been fitted to experimental data. Equations 7.2-7.4 can then be used to determine the generation and consumption rates of the other species using the reaction stoichiometry (from R 7.1) where 'n' and 'm' are determined from the product distribution and 'A' represents the H_2:CO consumption ratio.

CO reaction rate	$-r_{CO} = \frac{aP_{CO}P_{H_2}}{(1+bP_{CO})^2}$	(7.1)
H_2 reaction rate	$-r_{H_2} = -r_{CO} \times A$	(7.2)
FT Product formation rate	$r_P = -\frac{-r_{CO}}{n}$	(7.3)
H_2O formation rate	$r_{H_2O} = -(-r_{CO})$	(7.4)

Utilising the rate expressions (Equations 7.1-7.4) differential equations can be formed and utilised to model the reactant conversion and product generation through a reactor. This technique is used in the model developed in Section 11. The rate expression from Yates and Satterfield has been used many times indicating its viability despite the simplicity compared to the models discussed in the other literature [109, 111, 112].

7.3. The Water-Gas-Shift Reaction

The second most commonly occurring reaction in Fischer-Tropsch systems is the water-gas-shift (WGS) reaction (R 7.2). This reaction reduces the amount of CO in the feed gas and increases the amount of hydrogen making it useful in systems where the synthesis gas feed is hydrogen poor such as coal derived synthesis gas. Iron catalysts are known to catalyse this reaction making it an important consideration in the operation of an iron based system. Cobalt and ruthenium catalysts do not promote this reaction so it does not weigh as heavily in the design considerations as it does for iron.

R 7.2 $CO + H_2O \rightleftharpoons CO_2 + H_2$ Water-Gas-Shift Reaction

Given that cobalt catalysts are to be used in this work the kinetic and mechanistic effects associated with the water-gas-shift reaction have not been investigated. If iron catalysts were to be used in the reactor system it would be pertinent to include the effects of this reaction in the modelling and design of a system.

7.4. The Boudouard Reaction

The third reaction to consider is the Boudouard reaction which is converts CO to CO_2 and coke (carbon) (R 7.3). The reverse of this can be utilised along with the shift reaction to produce synthesis gas from coal or coke with low CO_2 emissions [cite: Boudouard reaction for synthesis gas]. As this consumes the CO reactant required for Fischer-Tropsch synthesis (R 7.1) it is not desirable to have high activity for this reaction.

R 7.3 $2\,CO \rightleftharpoons CO_2 + C$ Boudouard Reaction

As with the water-gas-shift reaction, the effect of the Boudouard reaction in most Fischer-Tropsch systems is not a significant consideration. It is likely to be present only when the CO content of the gas is very high and the temperature and pressure make it thermodynamically viable for this reaction to proceed forwards. Such a condition could be present in systems using coal derived synthesis gas as the carbon content of the feedstock is much higher than the hydrogen content.

8.0. Experimental Equipment and Methods

This section describes the equipment used in the microchannel reactor experiments and how the catalysts were applied to the different designs. Firstly the reactor designs will be considered, followed by descriptions of the catalyst formation methods. Finally the operation of the reactor rig during catalyst reduction and Fischer-Tropsch synthesis is described.

8.1. Experimental Reactor Designs

Two reactor designs were used in this study: a channel block with support structure and a microchannel plate system. This section describes each design in turn and highlights some of the design based advantages and disadvantages.

8.1.1. Design 1: Channel Reactor with High Surface Area Support

The first type of reactor trialled experimentally was a channel block with support structure, such as corrugated wire mesh (Figure 8.01), as recommended from the previous work by Penniall [3]. The channel block measuring 50 x 50 x 8 mm was constructed by welding together 4 pieces of steel to create a channel measuring 50 x 20 x 2 mm through the centre of the assembled block. This block was then positioned into the overall assembly by clamping between the top and bottom plates (Figure 8.02) before adding the sealing gaskets and endplates (Figure 8.03). To facilitate the heating of the reactor to achieve the desired operating temperature, two three inch long 100 W cartridge heaters (Hotwatt SC25-3) were mounted into the top plate of the reactor.

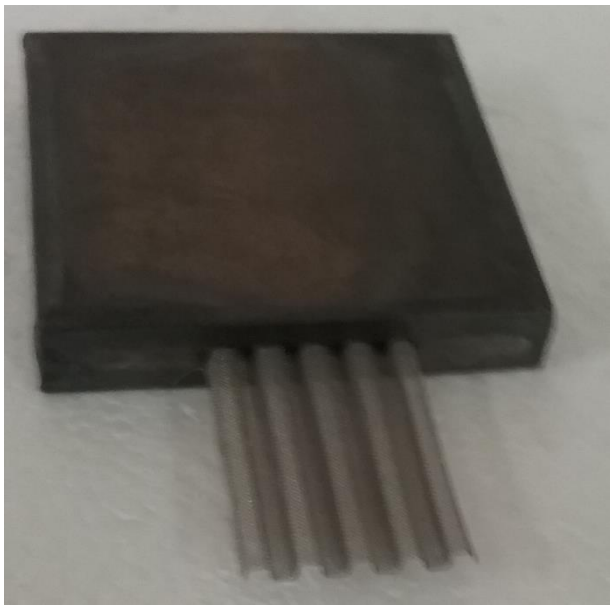

Figure 8.01: Reactor channel core with corrugated wire mesh partially inserted. Mesh corrugations are 2 mm x 2 mm and core block is 50 mm x 50 mm x 8 mm with a 20 mm x 2 mm slot through it.

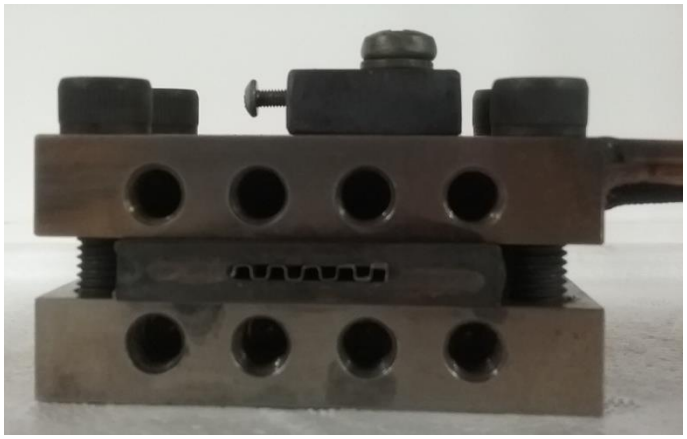

Figure 8.02: Partially assembled reactor (design 1) with the mesh in the centre. The small block on the top anchors a thermocouple when the reactor is in use for use in the temperature control loop. The plate extending out the right of the image supports the heating element wires.

Figure 8.03: Fully assembled reactor (design 1) with the endplates and sealing gaskets in place and foil caps over the fittings to prevent dust getting into the reactor.

The plates were fastened together by M8 cap screws in 35 mm (top and bottom plates) and 20 mm (endplates) lengths. The endplate screws were tightened with a torque wrench to 40.67 N·m (30 ft·lb_f) to prevent gas leaking. 1 mm copper plate was used for the sealing gaskets as it could be re-used many times by annealing between runs and it was more durable than the alternative aluminium foil. Copper is known to influence the formation of Fischer-Tropsch catalysts [57] however due to the limited amount of this exposed to the syngas it was deemed to not be of concern.

This reactor design allowed for various support structures to be inserted into the central cavity to provide a microchannel nature to the flow spaces while avoiding the manufacturing difficulty and cost associated with cutting microchannels directly into a part. Stainless steel mesh with 100 openings per square inch and 0.1 mm diameter wires (Steel and Tube NZ) was the first material used as the support structure with 2 mm square corrugations folded into it (Figure 8.04).

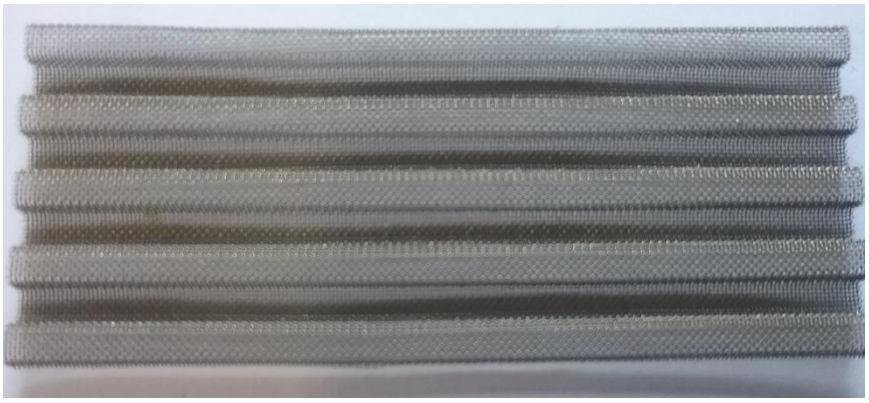

Figure 8.04: Corrugated stainless steel mesh support structure as used in reactor design #1.

These corrugations were initially made using a stamp like device made from pieces of 2 mm shim plate welded together. This technique proved problematic as the mesh became strained, unevenly folded and even broken along some fold boundaries due to stretching as the fold was formed (Figure 8.05). This problem was solved by constructing a roller device (Figure 8.06) to fold the mesh by pulling new material in from the open side of the fold as it was forming, giving an even fold with minimal strain on the mesh wires. The roller formed mesh could then be cut to size by trimming along the edge of the outside corrugation with a knife blade.

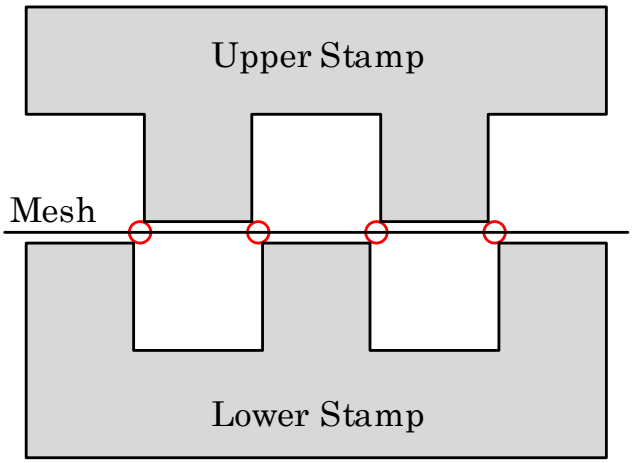

Figure 8.05: Schematic showing the stretch and strain points (marked with red circles) when forming the corrugations in the mesh using the stamp device. Strains occur as the mesh is pinched at the marked points and pulled in both directions until it yields.

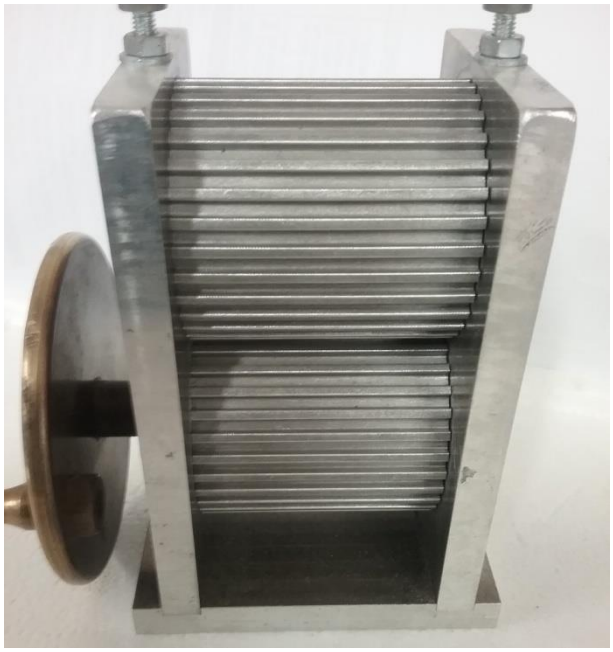

Figure 8.06: New mesh folding roller device. The mesh is fed between the two aluminium rollers which pull it into the corrugated shape without undue strain on the wires.

The second type of support utilised was Incofoam nickel foam with a pore (void) size of 600–800 μm and density of 460 g·m^{-2} (Figure 8.07). This was simply cut to size to fill the channel space in the reactor block and inserted before assembly. This had good potential for scale-up as metal foams can be purchased in large quantities (up to 300 m lengths) and the material can easily withstand typical Fischer-Tropsch operating conditions. Some difficulty was found in cutting the foam initially with the edge pores becoming crushed and blocked, which would inhibit the gas flow through the reactor. This was remedied by adjusting the cutting technique to apply minimum pressure to the metallic network in the foam. For a larger operation this could be difficult although a form of hot wire cutting, electronic discharge machining (EDM) or laser cutting may be applicable.

Figure 8.07: Reactor insert sized piece of Incofoam nickel foam with 600-800 μm pores and a density of 460 g·m^{-2} of sheet.

8.1.2. Design 2: Electronic Discharge Machining (EDM) Cut Microchannels

This reactor is based on the design used by Penniall [3] and consists of EDM cut microchannels in stainless steel shim plates which are stacked between two large outer plates made of tool steel. The large outer plates provide the physical strength to withstand warping, plus the tool steel can be hardened to provide a hard flat surface for rigid channel shape and good sealing. As with Design 1, two three inch long 100 W Hotwatt heating elements were mounted into the top plate of the reactor to provide the heating required to operate isothermally at 240 °C. Two different shapes of shim plate were cut (Figure 8.08) for the feedplates (a) and reaction channels (b). To assemble the reactor a pair (one of each shape) of plates and a set of aluminium foil gaskets were located onto the base using 4.9 mm drill bits as guides (Figure 8.09). Twelve 35 mm M8 capscrews were then used to fasten the top and base plates together with the screws fastened to 40.67 N·m (30 ft·lb) using a torque wrench.

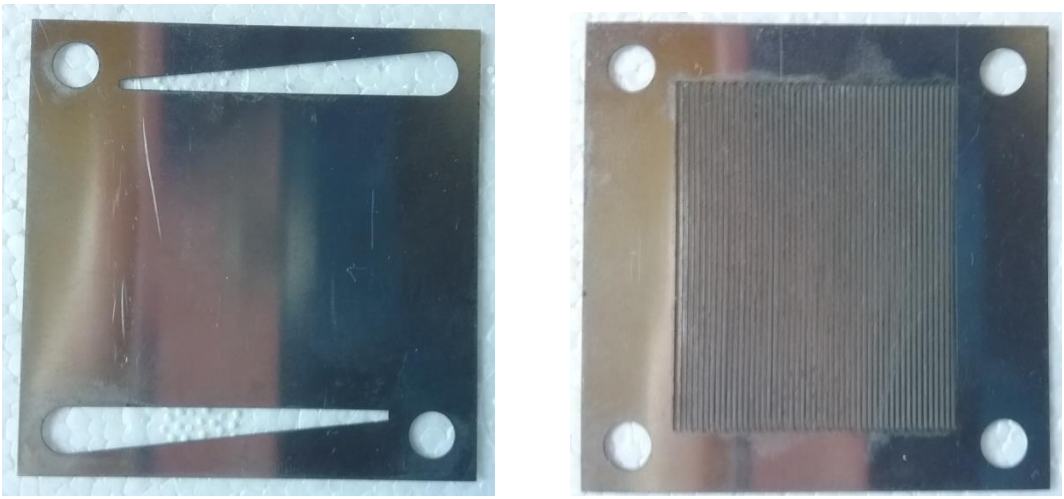

(a) (b)

Figure 8.08: Wirecut stainless steel shim plates used for the feed distribution plates (a) and 0.3 mm reaction microchannels (b) in design #2.

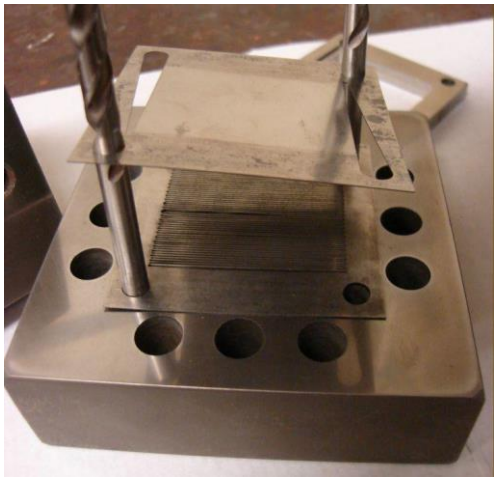

Figure 8.09: Assembling the microchannel reactor using 4.9 mm drill bits as guides [3]

A weakness of this design is that stainless steel shim plates are expensive and time consuming to manufacture using the EDM cutting even though multiple layers of shim can be cut simultaneously. Penniall [3] investigated the potential to manufacture them using alternative techniques including photolithographic etching and laser cutting however determined that the EDM cutting was more reliable for this purpose. Recent developments in 3D printing technologies such as Selective Laser Melting (SLM) create objects by melting layers of powder 30-60 μm thick [114] which could allow for the channel plates to be manufactured in shape rather than machined from shim. This could easily include the feed plate within one part thus eliminating potential leak points from the assembly, especially if multiple layers are used. Depending on the final design and manufacturing limits, this could potentially extend to the entire assembly for a stack of channels being made as one part, including heat transfer channels in alternating/adjacent layers. SLM 3D printing the entire structure as a single part may also be much faster than cutting and subsequently assembling many layers of shim.

Initially the channels for this design were only 0.3 mm wide. This had been notably difficult to manufacture, with EDM, laser cutting and etching the only technologies capable of working at such small dimensions. Penniall tested the use of photolithographic etching for forming the channels however found it unreliable. In addition he found laser cutting would quote its maximum material cutting thickness but not the minimum cut width so it was not pursued [3]. As wider channels would be easier to cut, the influence of channel width was examined by removing some dividing bars to create wider channels (Figure 8.10). These were assembled into the reactor in the same way as the un-modified plates to allow the same catalyst coating and synthesis run procedures to be used.

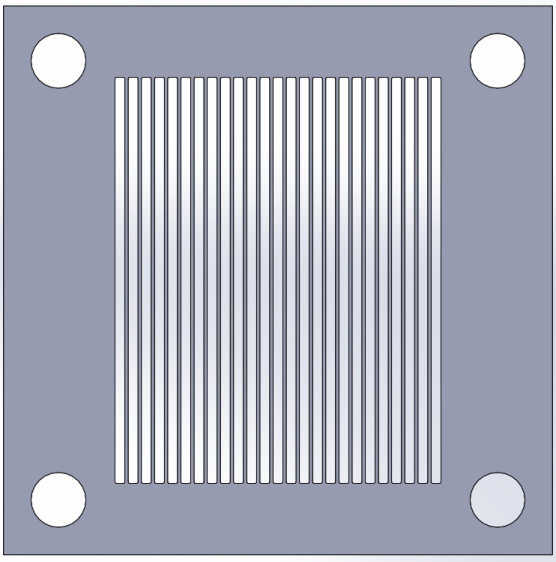

Figure 8.10: SolidWorks model of microchannel plate with every second divider bar removed creating 0.9 mm wide channels as an example of a modified channel plate

Similarly, testing of multiple layers of channels in parallel was also done in the same reactor assembly. Alternating layers of feed and channel plates were positioned in the stack, separated by appropriate gasketing. This arrangement was preferred over only gaskets between the channel plates so as to avoid damaging the gaskets by giving them a rigid support on one side. It also provided a more even distribution of both coating solution and synthesis gas through each layer.

8.2. Catalyst Deposition Methods

Three main catalyst deposition methods were used through the course of this research: washcoating, cathodic electrochemical deposition and solution combustion synthesis. Each method or variation was chosen to alleviate a weakness of the previous method or simplest variation. This enabled a systematic progression towards the overall goal of finding the optimum combination of catalyst formation and reactor design.

8.2.1. Washcoat Catalyst Formations

The first trialled coating method was the washcoating method. For this technique, the supporting structure is immersed in solution before the solvent is evaporated to leave the precursor deposited on the surface. This deposition is subsequently calcined to complete the formation process. Several variations of this technique were used over the course of the experimentation, attempting to improve the results each time.

8.2.1.1. Simple In-Situ Washcoating

This was the base technique and utilised a solution of equal parts cobalt nitrate hexahydrate ($Co(NO_3)_2 \cdot 6H_2O$) and de-ionised (DI) water by mass. This was injected to the reactor with a syringe to fill the void volume with solution. Drying (80 °C) and calcination (400 °C) then take place in-situ to (ideally) cover the entire inner surface in catalyst precursor particles.

With design 1, the reactor is assembled with the coating endplates (Figure 8.11) fitted in place of the regular endplates. 40 mm long sections of transparent flexible tube were added to each end to enable visualisation of the solution in the lines to determine when the reactor was full. The solution was injected with syringe until it became visible in the extension out the far end of the assembly. At this point the solution was pulsed back and forward a few times to remove any remaining air pockets from inside the reactor ensuring good coverage of the support. Drying is then completed at 80 °C for six hours to remove solvent before removing the flexible tubes and heating to 400 °C for four hours of calcination in air.

(a) (b)

Figure 8.11: Endplates for the support structure reactor. (a) Alternative endplate style which is attached to the support structure reactor during coating processes to prevent the precursor solution from running out the ends. (b) Standard endplate used during reactor operation.

The procedure for this technique in the microchannel reactor (design 2) is very similar. Given the design is different, the two flexible tubes are inserted to the ports rather than the endplates. This helps to keep the fittings clean to ensure a good seal when connected to the gas lines during reduction and synthesis. Drying time at 80 °C can be reduced to four hours, since the volume of solution is significantly smaller. Calcination is identical to the other design, running for four hours at 400 °C.

8.2.1.2. Ethanol Washcoating

The standard in-situ washcoating method was also trialled with ethanol as the solvent in place of DI water. The solution was still based on equal weights although the lower density of ethanol results in a lower concentration of Co. The drying temperature was also lowered to 70 °C to avoid boiling the ethanol (BP 78.3 °C) as this would create pockets in the channel with poor coating. The remainder of the coating procedure remained identical with the same durations used for drying and calcination.

8.2.1.3. Dilute Washcoating

A diluted solution was also used for in-situ washcoating. It was applied using the same methodology for drying and calcination as the standard washcoat procedure. The difference here was that the solution contained significantly less $Co(NO_3)_2 \cdot 6H_2O$ with only 0.208 g per gram in DI water. This was calculated to match the mass of cobalt precursor in the injected solution per unit surface area of the mesh and channel to that of the microchannel plate reactor with the standard solution. In theory, this ensures a similar layer thickness in the deposited catalyst on the support compared to the channel walls.

8.2.1.4. Ex-Situ Washcoating

The support structures used in design 1 could also be coated ex-situ. This process was done using the same equal mass solution of $Co(NO_3)_2 \cdot 6H_2O$ in DI water as the in-situ method. The sample to coat was firstly rinsed with DI water then submerged in the solution and agitated slightly to remove air bubbles from the surface. After 1 minute the sample was inverted and submerged for a further minute to ensure even coating across the surfaces. At the conclusion of the second minute the sample was removed from the solution and placed into an oven at 80°C for 30 minutes. Following this drying the coating process was repeated to ensure all surfaces were covered with catalyst precursor. Calcination was then completed in a tube furnace at 400°C for four hours. This method was utilised for coating both corrugated mesh and nickel foam support structures but could not be applied to the microchannel design. The incompatibility arises from two factors, the majority of the surface area being on the foil gaskets rather than the channel plates and difficulty masking the sealing faces to avoid coating them.

8.2.2. Electrochemical Deposition

This technique was adapted from that used by Brownson and Lévy-Clément [101] to accommodate a larger metallic sample as the working electrode in place of their transparent conductive oxide. A 0.005 $mol \cdot L^{-1}$ $Co(NO_3)_2 \cdot 6H_2O$ and 0.1 $mol \cdot L^{-1}$ KNO_2 solution was used to perform the coating in an electrochemical cell with the support structure placed as the cathode (Figure 8.12). Hydroxide ions are generated by reduction of nitrite and nitrate (R 8.1 and R 8.2/8.3 respectively) which attract the cobalt ions from the solution to form the deposited $Co(OH)_2$. Due to the concentration ratio used R 8.1 is expected to be the dominant hydroxide formation pathway.

R 8.1	$NO_2^- + 5\,H_2O + 6\,e^- \rightarrow NH_3 + 7\,OH^-$	Nitrite
R 8.2	$NO_3^- + H_2O + 2\,e^- \rightarrow NO_2^- + 2\,OH^-$	Nitrate (a)
R 8.3	$NO_3^- + 6\,H_2O + 8\,e^- \rightarrow NH_3 + 9\,OH^-$	Nitrate (b)

This method was used to prepare coatings on corrugated mesh and nickel foam supports which were connected to supporting wires before placing in the cell. Mesh was folded and pinched in a ‘hook’ on the end of the wires, while the nickel foam was spot-welded on. Both ensured a contact point for the current to flow through, ensuring the support was well coated. To achieve these fixings, extra tabs (Figure 8.13) were required on the sides of the support material to enable coating without damaging the main area of the structure. These tabs were trimmed off afterward so the structure was the correct shape to fit within the channel slot. This was not be used on the microchannels as masking the surface to prevent coating sealing faces was impractical.

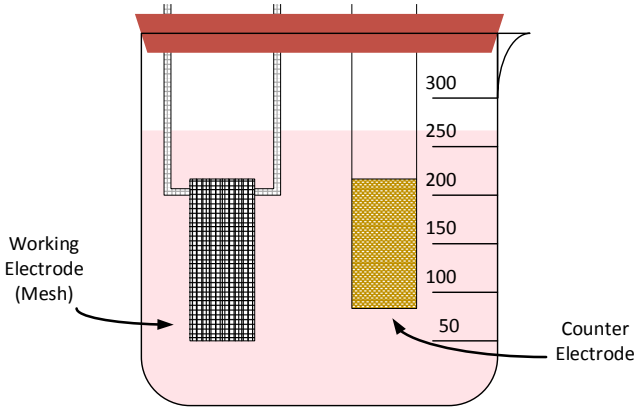

Figure 8.12: Diagram of electrochemical cell setup in a beaker showing support structure as cathode and metal plate as the counter electrode.

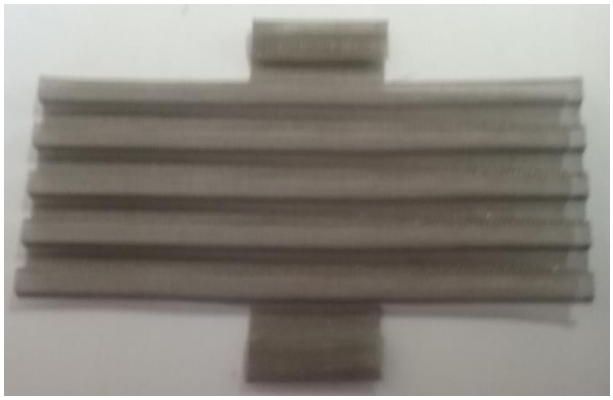

Figure 8.13: Uncoated corrugated mesh sample showing extra tabs required for attachment to the electrochemical cell.

Once connected to the support wires, the electrodes were rinsed with alcohol (ethanol or IPA) and then deionised water to ensure the surfaces were clean before coating. Cleaned electrodes were connected to a potentiostat to apply the operating potential and the cell was run with -10 mA constant current to drive the deposition over a duration of 150 minutes. The solution was stirred at 200-250 rpm using a magnetic stirrer flea to ensure ion concentrations were uniform throughout the cell. These operating conditions were later varied based on results with the best operation attained with -20 mA of constant current applied for 90 minutes with the solution stirred at 150-175 rpm.

For some trials, acid etching with 0.1 $mol \cdot L^{-1}$ nitric acid was applied to the mesh prior to deposition in an attempt to improve the bond between catalyst and mesh therefore minimising catalyst entrainment during Fischer-Tropsch synthesis. The mesh sample was placed into sufficient nitric acid to completely cover it and left for 30 minutes. After 30 minutes it was inverted and left for a further 30 minutes to attempt uniform etching. The etched mesh sample was then thoroughly rinsed with DI water and left to dry in air overnight.

Calcination of electrochemical deposition catalysts was also completed at 400 °C using the tube furnace. After a few trials had experienced difficulty a temperature interval for heating was applied to prevent excessive thermal expansion rates during the process. Initially this interval method used 75 °C intervals from 25 °C to 400 °C, however this was later adjusted to 80 °C intervals from 80 °C upward to allow it to be used for all coating methods.

8.2.3. Solution Combustion Synthesis

This coating required the same equipment as the standard washcoating procedure for completing the deposition. It was only utilised in-situ to coat the maximum useful surface possible although ex-situ coatings would be possible. For this method, urea was used as a combustion fuel to generate the desired cobalt species inside the reactor via Reactions R 8.4 – R 8.9 Urea was added to the standard washcoating solution at a 2x molar excess of the ratio defined by balancing the valencies of the fuel and the oxidant (Appendix A) to give the solution in Table 8.1.

Table 8.1: Composition of solution used for solution combustion synthesis coatings

COMPOUND/SPECIES	**MASS (G)**
$Co(NO_3)_2{\cdot}6H_2O$	5.00
DI Water	5.00
Urea	3.44

The solution was injected and dried at 80 °C per the standard washcoating method to coat the inner surfaces with the reactants. During heating to 400 °C for calcination, the mixture auto-ignites at around 300 °C, oxidising the urea fuel (R 8.4) and reducing the nitrate (R 8.5). This forms very fine Co particles due to the large number of moles of gas (23) formed in R 8.7 which helps to prevent the agglomeration seen in the washcoating. The CoO product from the combustion synthesis is then further oxidised during calcination to Co_3O_4 (R 8.8).

R 8.4 $$(NH_2)_2CO + H_2O \rightarrow CO_2 + N_2 + 6\,H^+ + 6\,e^-$$ Urea Oxidation

R 8.5 $$2\,NO_3^- + 12\,H^+ + 10\,e^- \rightarrow N_2 + 6\,H_2O$$ Nitrate Reduction

R 8.6 $$Co^{2+} + H_2O \rightarrow CoO + 2\,H^+$$ Calcination 1

R 8.7 $$5\,(NH_2)_2CO + 3\,Co(NO_3)_2 \rightarrow 3\,CoO + 8\,N_2 + 5\,CO_2 + 10\,H_2O$$ Overall SCS

R 8.8 $$3\,CoO + \frac{1}{2}\,O_2 \rightarrow Co_3O_4$$ Calcination 2

8.2.4. Catalyst Examination by Scanning Electron Microscopy

Details of the catalyst microstructure were examined using a Jeol JSM-7000F scanning electron microscope (SEM) at accelerating voltages of 10-15 keV. Samples were normally analysed in the calcined state as this was the most stable structure, however for some samples the reduced state was used. To examine samples from the inserted support reactor, only the support structure (mesh/foam) was fixed to the holder for analysis. For the EDM microchannels the channel plate and rear foil gasket were separated from the remainder of the reactor and fixed to the holder.

In contrast with the support and block reactor, the structures from the EDM microchannel reactor could not be used for Fischer-Tropsch synthesis after SEM analysis and a new sample had to be prepared. This is due to bending and tearing of the shim plate and aluminium foil gaskets respectively during disassembly of the reactor structure since the metals tended to bond together after operating at 400 °C during calcination.

8.3. Reactor Operation and Product Detection

8.3.1. The Reactor Rig

The reactor rig (Figures 8.14 to 8.16) consists of a simple setup with three available gas feeds (synthesis gas, H_2 and N_2) connected to a selection manifold used to select the reactor feed. The valve manifold is not designed for mixing and therefore the synthesis gas supply is a pre-mix of 32 mol% CO and 4 mol% N_2 in H_2 (64 mol%). Flows are monitored using a Sierra Instruments Smart-Trak 830 series mass flowmeter on the inlet and a small bubble flowmeter on the outlet. The bubble flowmeter is calibrated for each run using a syringe since the marked scale is for air. Pressure and flow are controlled using the regulator valves at the gas cylinders and the outlet needle valve respectively. Condensable products are collected in a cooled knockout vessel below the reactor which is maintained at ~5 °C by cooling it with ethylene glycol at 0 °C. Safety features include a pressure relief valve between the inlet measurements and the reactor, a fail closed solenoid valve on the synthesis gas supply (to avoid CO leaks) and a CO detector mounted above the rig. A portable CO detector is also used during operation. The gas chromatograph (GC) sampling line is connected to the vent for on-line gas analysis during synthesis runs to determine reactant conversion, and production of methane, C_2, and CO_2. A webcam was used to capture snapshots of the system at set intervals to enable the flowrate to be recorded each time the GC took a sample enabling accurate calculations afterward.

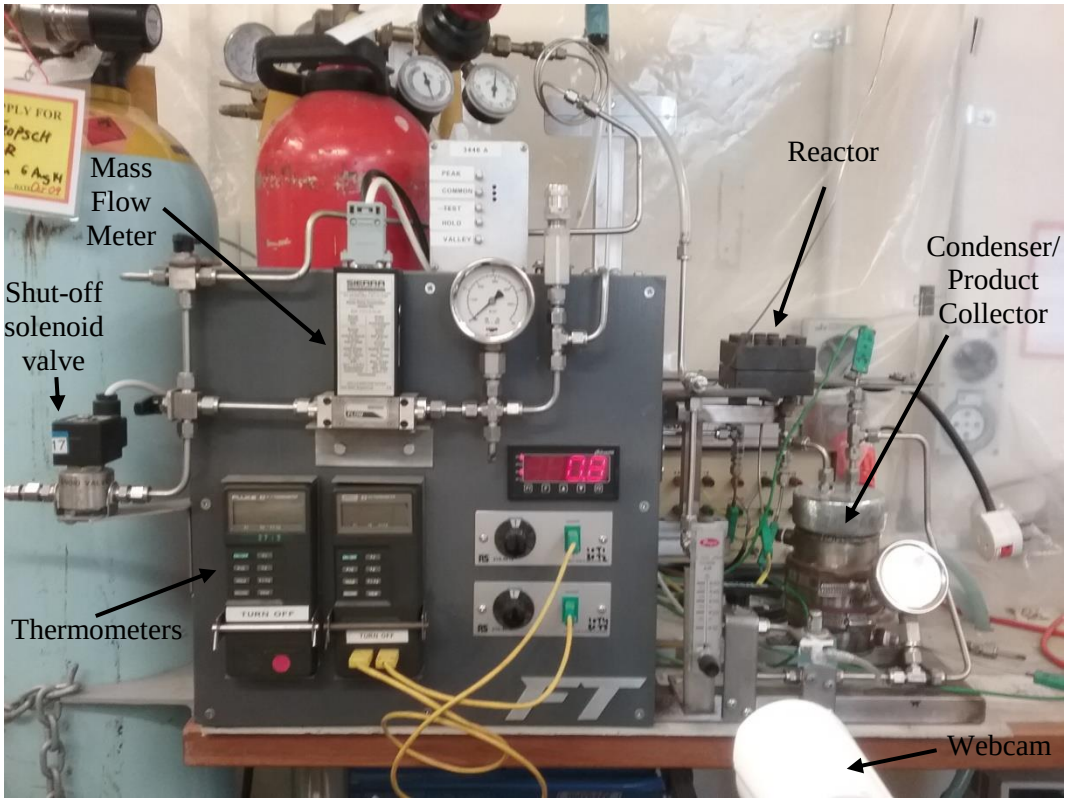

Figure 8.14: Photo of reactor operation rig used for catalyst reduction and Fischer-Tropsch synthesis with the reactor in place and the insulation removed. For additional information refer to Figure 8.16.

Figure 8.15: Web camera capture of operating system used to capture flowrates and monitor the system remotely. Values for the inlet (1) and outlet (2) flows, outlet side pressure (3) and reactor temperature (4) can all be obtained from the image and recorded against the timestamp in the top right of the image.

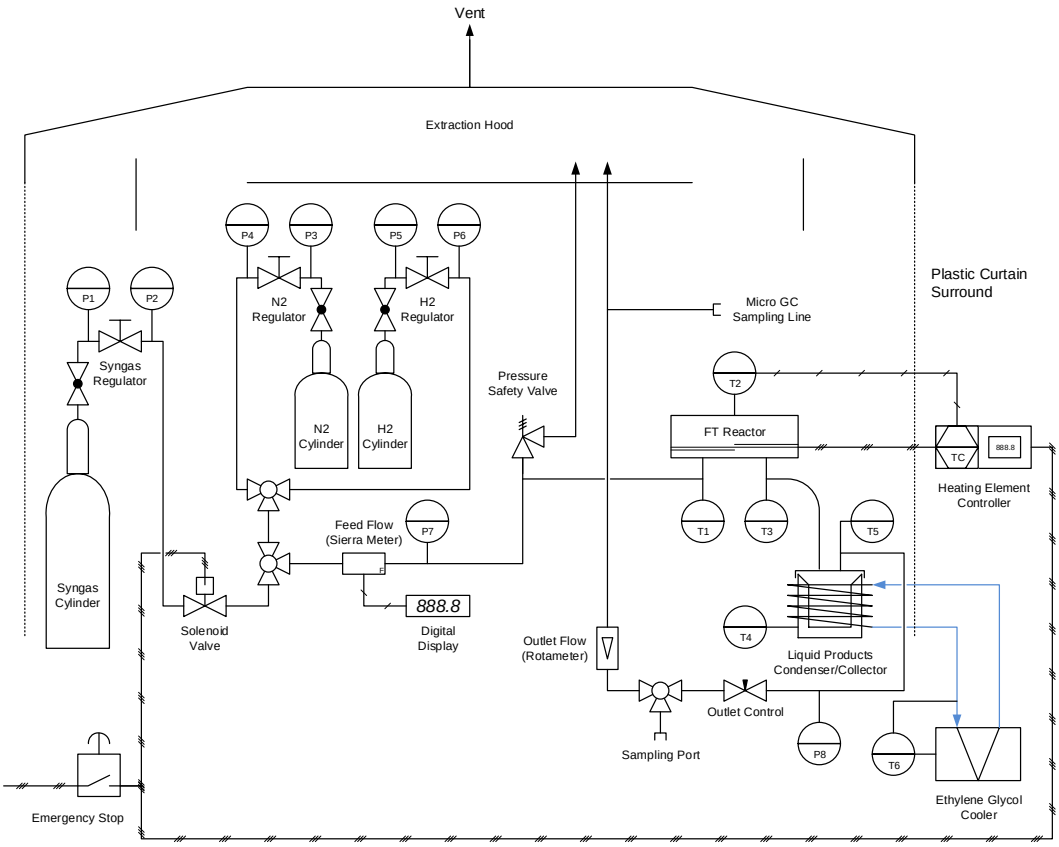

Figure 8.16: Process flow diagram (PFD) of the Fischer-Tropsch reactor rig used in the experiments. This version shows the microchannel plate reactor in place. The support filled channel reactor sits in a similar position. A larger, fully labelled version of both PFD's is included in Appendix B.

8.3.2. Catalyst Reduction Method

Prior to Fischer-Tropsch synthesis, it is necessary to reduce the catalyst to its active state. To complete reduction, the reactor containing calcined catalyst, was assembled into the rig and the fittings secured. The reactor was first pressurised to 345 kPa (50 psi) with nitrogen so that all fittings could be checked for leaks with liquid leak detector prior to exposure to any toxic or flammable gasses. Once leak testing was complete, the system could be depressurised of nitrogen and pressurised with hydrogen to 345 kPa once more. After confirming the absence of leaks in the presence of hydrogen, insulation was applied and the reactor heated in 80 °C increments (Table 8.2) up to 400 °C. Increments were used to maintain a smooth heating load to avoid burning out the heating elements. With the system at 345 kPa and 400 °C, an inlet H_2 flow of 30 standard cubic centimetres per minute (SCCM) (1.8 $L \cdot h^{-1}_{STP}$) was applied and reduction was completed for four hours. Following reduction the system was slowly depressurised and cooled. The flow during depressurisation is kept low (<100 SCCM) to avoid entraining small catalyst particles. Additionally a minimal pressure of hydrogen is retained in the system to ensure that it remains free of air as oxygen will deactivate the catalyst.

Table 8.2: Temperature increments for reactor heating during reduction and synthesis

HEATING STEP	INITIAL TEMPERATURE (°C)	FINAL TEMPERATURE (°C)
1	Ambient	80
2	80	160
3	160	240
4	240	320
5	320	400

8.3.3. Fischer-Tropsch Synthesis Method

Following reduction, the sealed system is pressurised with synthesis gas for Fischer-Tropsch synthesis. Initially 10 bar was used, however in later experiments 20 bar was used to improve the reaction rate. As with depressurisation after reduction, low flow is maintained during the pressurisation to avoid catalyst particle entrainment. Once the chosen pressure is reached and stable, the reactor is heated to the operating temperature (240 °C) using the same increments as reduction. Cooling for the collection vessel is set to 0 °C and the glycol circulation started. The inlet gas flowrate is set by adjusting the outlet needle valve and varies with reactor design (Table 8.3). With the temperature, pressure and flow, all at the desired values synthesis is run for a period of at least six hours. During this time, recordings of the inlet and outlet flows are made every 15 minutes for use in the mass balance and reactor performance calculations with the product analysis data.

Table 8.3: Operating flowrates of different reactor designs

REACTOR DESIGN	GAS FLOW (SCCM)
Mesh/Foam in Block	30
0.3mm microchannel	30
Multi-width microchannel	30
0.9mm microchannel	60

8.3.4. Product Detection Procedures

The first of the two product analysis stages is completed on-line using an Agilent 3000 micro-GC containing two columns (molecular sieve and plot-Q), both with thermal conductivity detectors (TCD). The first column (molecular sieve) was used to detect H_2, N_2, O_2, CO and CH_4 in the tail gas. From this data, the mass balance was able to be confirmed along with the reactant conversions and methane production. The second column (plot-Q) was used to detect CO_2, C_2H_4 and C_2H_6 in low concentrations. This was useful for identifying additional production and Fischer-Tropsch activity extending past methanation. Slightly larger, higher molecular weight hydrocarbons such as C_3H_6 and C_3H_8 may have also been present, however the GC detector was not calibrated for them.

The second stage of product analysis to determine the production of C_{5+} hydrocarbons and the ASF selectivity was completed post-run using a Varian CP3800 GC with a Varian Factor Four capillary column (30 m x 0.25 mm ID Part CP8912-VF-1ms). Firstly the outlet line was rinsed with 2-3 mL of n-hexane to dissolve any condensed waxes and wash them into the collection vial. The contents of the collection vial were then centrifuged to separate the non-polar organics from the aqueous phase and any particulate matter. The organic phase was then extracted by syringe and diluted in 1 mL of hexane to make the sample stock. Finally, to make each of the three analysis samples, 150 μL of the sample stock was sampled with a micro-pipette and further diluted with 1.5 mL of n-hexane in a GC sample vial. Analysis of the aqueous phase was not conducted since it is primarily water. The excess of hexane prevents accurate detection of C_5 – C_7 hydrocarbons however the detection through the subsequent range is sufficient to establish an ASF distribution. The method used on the GC is the summarised in Appendix C.

GC calibration solutions were prepared using a Restek hydrocarbon standard (CAT. 31459) diluted in hexane to a range of concentrations for forming calibration curves. The standard contained 14 paraffinic hydrocarbons ranging from C_9 – C_{36} all at 1000 $\mu g \cdot mL^{-1}$ in hexane. An additional solution containing dodecane (C_{12}) in hexane was also used to identify a reference peak. Other peaks could be determined from this one since elution times from the column increase with chain length. While the Fischer-Tropsch synthesis does produce some olefins, since the intended use of the product is as a fuel, it is the chain length distribution and not the olefin/paraffin ratio that is of interest.

9.0. Support and Block Reactor Results and Analysis

The first reactor system examined experimentally was the support and channel block micro-reactor, designed by Penniall [3]. It was thought that this reactor design posed better scale up possibilities than the microchannel plate reactor that Penniall had used himself as the manufacturing was easier and cheaper. Firstly various catalyst deposition techniques were analysed using SEM imaging in an attempt to produce a structure similar to the successful ones Penniall was able to observe in his work. Subsequently the best structures from each type of deposition were examined in Fischer-Tropsch synthesis operation to confirm the findings from the structural comparisons.

9.1. Washcoat Catalysts on Corrugated Mesh

The first type of catalyst coating used experimentally was the simple cobalt washcoat onto corrugated mesh inside design 1. This was a very simple procedure, as outlined in Section 8.2.1, and much was expected given the success of the coating in Penniall's work [3]. Landers and Reijken [115, 116] had attempted to demonstrate this on the new reactor design, however very limited success was achieved. Their experiments produced lumpy agglomerate catalyst particles which subsequently produced very little, if any, Fischer-Tropsch activity. Repeating this experiment using the mesh in block design, it was observed that the catalyst was easily deposited onto the mesh. Whilst the deposition was simple, it lacked control over layer thickness and dispersion with unevenly distributed agglomerate lumps across the surface (Figure 9.01). Based on the results obtained by Landers [115]and Reijken [116] this type of deposition provides very little activity and is therefore undesirable.

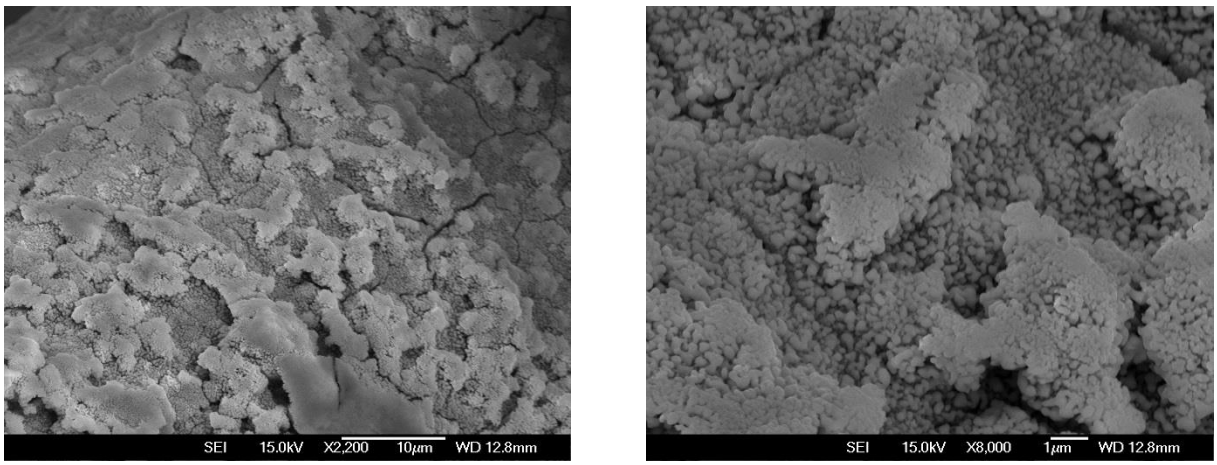

(a) (b)

Figure 9.01: SEM images of original washcoat catalyst on mesh showing the lumpy agglomerated deposition (a) and smaller constituent particles within the lumps (b). While the smaller particles can be identified, their shape and surface area is not exposed to the reactant gasses resulting in poor activity

This result contrasts with the original depositions attained by Penniall [3] in microchannels where the cobalt particles were fine spinel structures, well dispersed across the surfaces that generated a high Fischer-Tropsch activity. Given the lack of success with the simple washcoat, four variations in the technique were considered as possible improvements to avoid lumpy and uneven coatings. These variations were: a dilute solution, a higher drying temperature, doing the washcoating ex-situ and using ethanol as an alternate solvent.

With approximately 1/5th of the cobalt precursor in the solution, the coating from the dilute solution was expected to form a thinner film which was more disperse. Whilst there was less total coating, large plate structures with very little texture made up the majority of the deposition (Figure 9.02). Adjacent to these sheets there were some small spinel structures (Figure 9.03) with high surface area and a fine structure. However these were rare, with mainly agglomerate structures similar to the full concentration solution observed. The lack of improvement indicated a fundamental fault with the washcoating technique and that the catalyst caking was not simply a result of too much precursor.

Drying at a higher temperature of 90 °C rather than 80 °C was expected to give less time for agglomeration, with the water in the solution evaporating more rapidly. This also proved ineffective, with no notable difference in the produced structures. One difference was that during the drying time there was an increased amount of bubbling out the ends of the coating endplate tubes. As this only results in more cobalt precursor outside the reactor, this technique was deemed unhelpful.

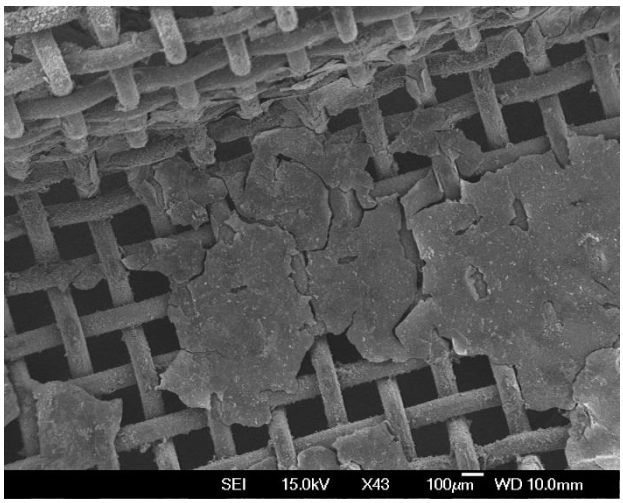

Figure 9.02: Despite the lower concentration, large sheets of deposition cover the surface of the mesh from the dilute washcoating method. While there is less caking than the full concentration the surface remains heavily covered by these thick surface layers, with little fine structure.

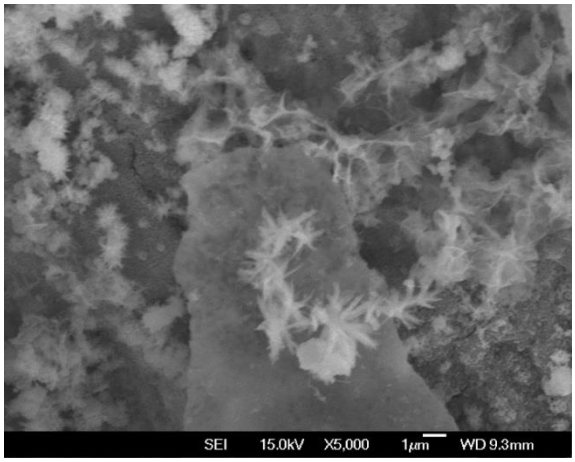

Figure 9.03: Using the dilute washcoating method some of this finer spinel type structure was formed, despite most of the deposition remaining lumpy as per the full concentration solution. This fine structure is preferable with a high surface area and lots of edges, ideal for active catalytic sites.

The third modification was to coat the mesh ex-situ rather than in-situ. This allowed the thickness of the film to be adjusted as the exposure to solution could be adjusted. Since the drying process was now completed in an oven with more air flow and less excess solution than the closed channel, only 30 minutes of drying time was found to be sufficient. The results remained disappointing, with even greater deposition and agglomeration (Figure 9.04) than the original in-situ sample (Figure 9.01).

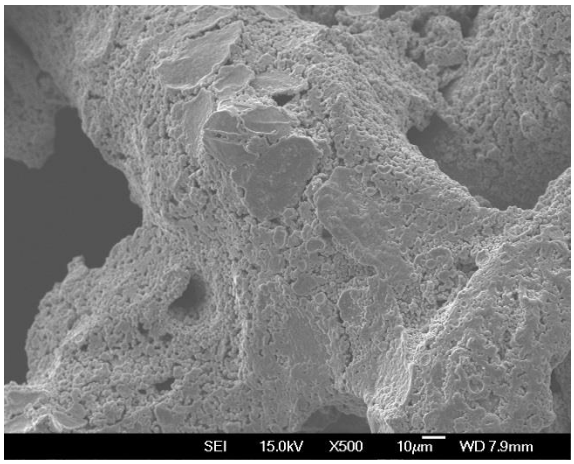

(a)

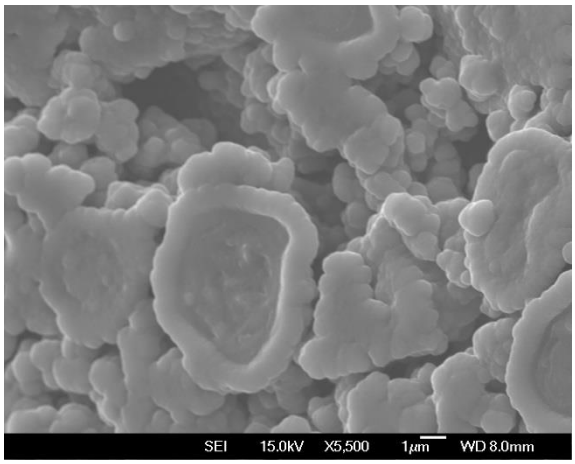

(b)

Figure 9.04: SEM images of ex-situ washcoat catalyst on mesh. An extensive layer of coating (a) was created due to the high solution concentration. Higher magnification (b) shows the constituent particles are poorly defined resulting in a lack of surface area and active sites exposed to the reactants.

Using an ethanol based solution for washcoating was able to achieve some, albeit limited, success in modifying the structure. Ethanol's increased volatility compared to water had been thought to improve the dispersion however large agglomerates continued to be present. The average particle size observed on the SEM images was smaller than for the aqueous solutions creating a rougher texture to the agglomerates of the coating layer (Figure 9.05). With this and the other variations in washcoating all failing to form the desired catalyst structure alternative depositions methods were considered.

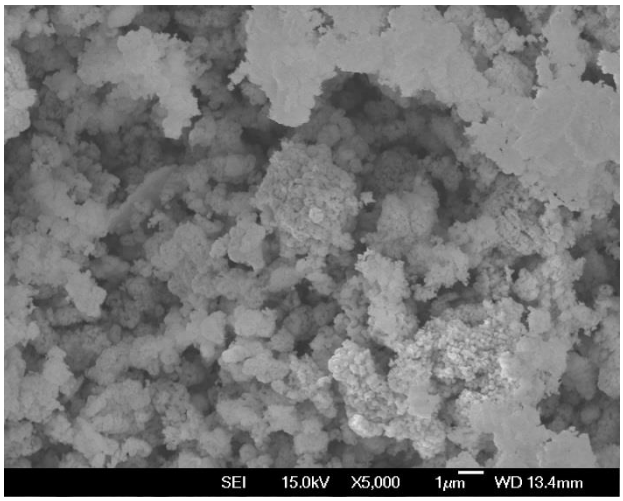

Figure 9.05: SEM image of the catalyst prepared using the ethanol washcoat. The particles appear smaller and rougher than the aqueous washcoat, however the amount of agglomeration and over-coating remains a concern.

9.2. Electrochemical Deposition Catalysts

Targeting the weaknesses of the washcoating methods, a technique which offered good control over layer thickness and dispersion was sought. Electrochemical deposition using an applied potential to drive the attraction of ions from the solution to the electrode was attractive for this purpose. Varying the potential (V) and current (I) applied to the cell, gave control of the thickness of the deposition and in the literature the nature of the depositions appeared very uniform across a sample [101]. Potentially the only question with this type of catalyst was its ability to catalyse the Fischer-Tropsch synthesis at the end with no prior use in this application. This was considered to be due to the inability to generate such a catalyst at the size required for industrial scale Fischer-Tropsch facilities.

9.2.1. Electrochemical Deposition Catalysts on Corrugated Mesh

Applying this technique to the mesh supports took some fine tuning with the first few trials failing due to insufficient stirring and/or the mesh becoming disconnected from the support wires (see Figure 8.2.2). These first trials ran at -10 mA constant current for 150 minutes. The low -10 mA current was determined by scaling the current proportional to the sample size, relative to the reference material, considering the mesh as a corrugated sheet. However, the rate of deposition observed on the mesh samples was very slow, hence the lengthy duration. By raising the current to -20 mA the duration to achieve the desired level of observable coating could be shortened to 90 minutes. Similarly, the stirring rate had to be lowered to reduce the turbulence in the cell. At 200-250 rpm the electrodes moved about too much and occasionally fell off the supports. 150-200 rpm was found to provide a good balance between mixing and turbulence and was used for the later trials.

The improvement using this technique compared to washcoating, was immediately visible to the eye with a very uniform green coloured layer deposited (Figure 9.06) compared to the large lumps formed in the grids from washcoating (Figure 9.02). Inspection by scanning electron microscopy revealed more features including similar nano-sized $Co(OH)_2$ vertically oriented platelet structures to those published by Brownson and Levy-Clement [101]. At high magnification, it could be seen that these micro-platelets had an ultra-high specific surface area with typical dimensions of <2 μm and thicknesses of only a few nanometers (Figure 9.07). This was a very positive result given the lack of success obtained using washcoating on this reactor design. The structure had very high surface area and a high amount of edges, two features often considered to be important for catalysts. These features had been present in Penniall's [3] catalysts which were successful in the microchannel plate design which gave promise to this technique.

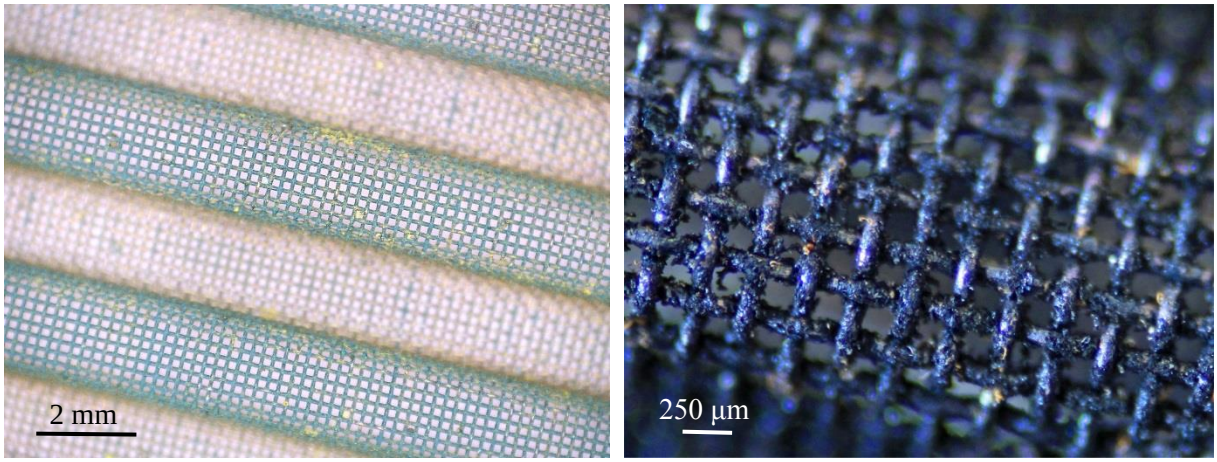

(a) (b)

Figure 9.06: (a) Electrochemical deposition sample showing a thin green layer on the mesh, much more uniform than layers attained by washcoating as evidenced by the colour consistency. Note: the corrugations in the mesh caused the rear side to be out of focus at this zoom level. (b) Post calcination the more traditional "cobalt blue" colour can be seen although the deposition looks more crystalline and less uniform.

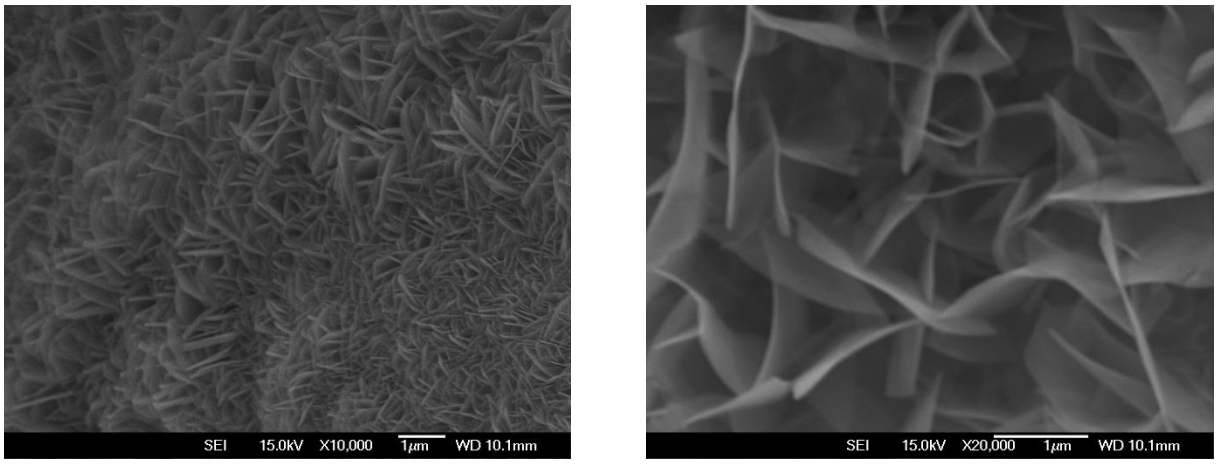

Figure 9.07: High magnification SEM images of the nano-platelets formed by the electrochemical deposition technique. The ultrafine structure created by this technique has an extremely high surface area and lots of edge sites which are desirable in the catalyst.

Given the success of this method, the potential to electrochemically coat the support inside the reactor (in-situ) was considered as it would maximise the coated area. A proposed setup for this is a counter electrode chamber connected in a fluid loop with the reactor block using non-conductive plastic endplates to isolate the charge (Figure 9.08) and a small pump to circulate the solution. Testing the setup showed that the potential (voltage) in such a setup would need to be too large in order to drive the reaction as the potentiostat was unable to supply a current.

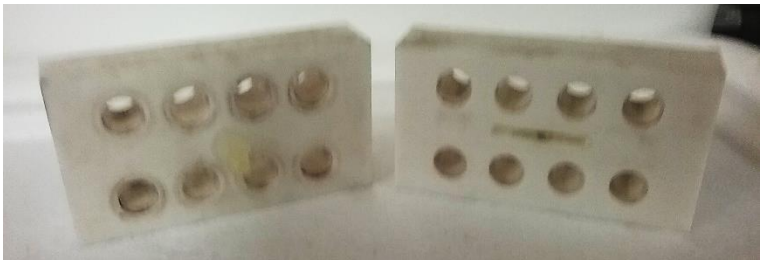

Figure 9.08: Outside (left) and inside (right) faces of the plastic endplates considered for in-situ electrochemical deposition which was abandoned due to impractical operation.

Analysing samples post calcination, some areas of the deposition seemed to be cracked and falling off the mesh (Figure 9.09), possibly due to the calcination process causing the metal wires to expand in the 400°C heat. In an attempt to improve the binding to the surface of the mesh, an acid etch with 0.1 $mol \cdot L^{-1}$ nitric acid to roughen the surface of the wires was used. This proved rather unhelpful with very little optically observable increase in surface roughness and a yellow coloured deposition layer, rather than the typical green. Electron microscopy (Figure 9.10) showed the formation of small octahedral nanoparticles, in addition to the platelets seen in the un-etched samples. These nanoparticles are thought to have been $K_3[Co(NO_2)_6]$, as it is insoluble in water and some yellow precipitate was also observed in the solution after coating.

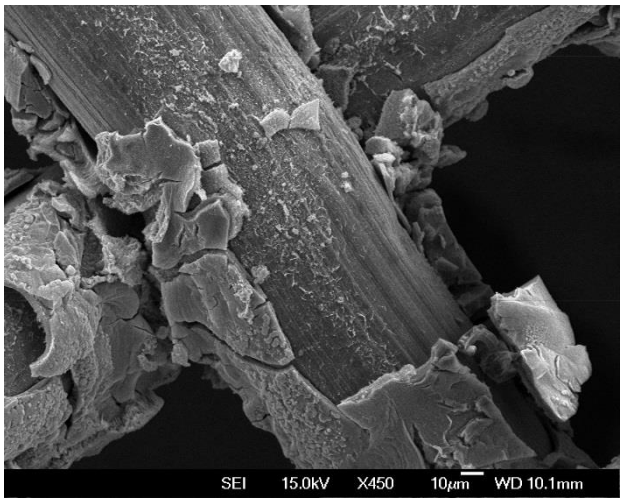

Figure 9.09: Large sections of the electrochemical deposition appear to have cracked and fallen off of the support mesh structure post calcination, potentially due to thermal expansion of the wires.

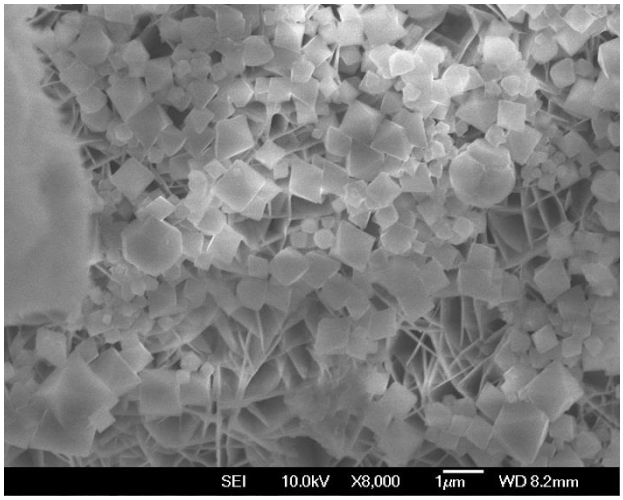

Figure 9.10: SEM image showing the octahedral nanoparticles formed on top of the nano-platelets when acid etching the mesh support structure prior to electrochemical deposition. The octahedral nanoparticles are yellow in colour although this cannot be seen in the greyscale SEM image.

A potential cause for the formation of these nanoparticles is un-neutralised H^+ ions remaining on the surface of the metal after etching. These would lower the pH near the cathode, reducing the formation of OH^- ions and therefore $Co(OH)_2$. This aligns with the $Co(OH)_2$ formation method discussed by Brownson and Levy-Clement [101] where the hydroxide formation creates a pH shift near the electrode, changing the favoured Co state from Co^{2+} to $Co(OH)_2$ (Figure 9.11). The additional H^+ ions will react with some of the OH^- ions produced by nitrite/nitrate reduction to form water. In turn this causes the pH to remain below the transition point and cobalt to remain as Co^{2+} rather than $Co(OH)_2$. The correlation between the acidity, nanoparticles and the yellow colour was able to be confirmed experimentally when the remaining solution after coating an etched sample was used to coat a second piece of mesh. This produced a coating resembling the un-etched trials.

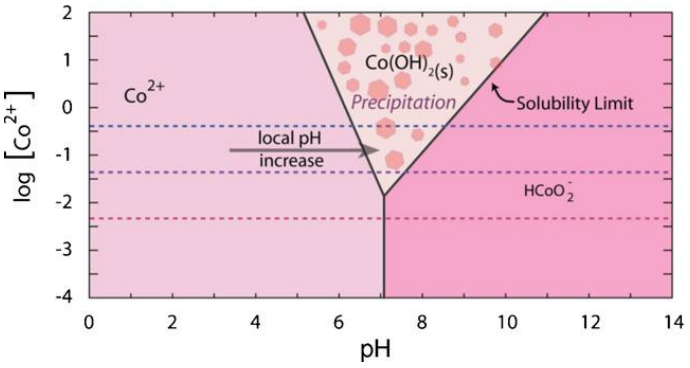

Figure 9.11: Co^{2+} concentration/pH phase diagram showing how the local pH increase caused by the formation of OH^- ions from nitrite/nitrate reduction leads to the formation of $Co(OH)_2$. Blue, purple and red dashed lines indicate Co^{2+} concentrations of 0.005, 0.050 and 0.500 $mol \cdot L^{-1}$ respectively [101].

Since etching had proved unhelpful, three additional modifications were considered to investigate the fracturing of the catalyst coating. The first of these was pre-calcining the mesh sample to achieve a more stable surface to deposit the $Co(OH)_2$ on. This proved unsuccessful with the deposition becoming lumpy and forming substantially less of the micro-platelet structure (Figure 9.12). The more dominant forms of deposition were agglomerates similar to ethanol washcoating and a foam-like structure (Figure 9.12b). Additionally there seemed to be larger regions of uncoated surface, suggesting that the pre-calcination may have hindered the adhesion of the deposition to the surface.

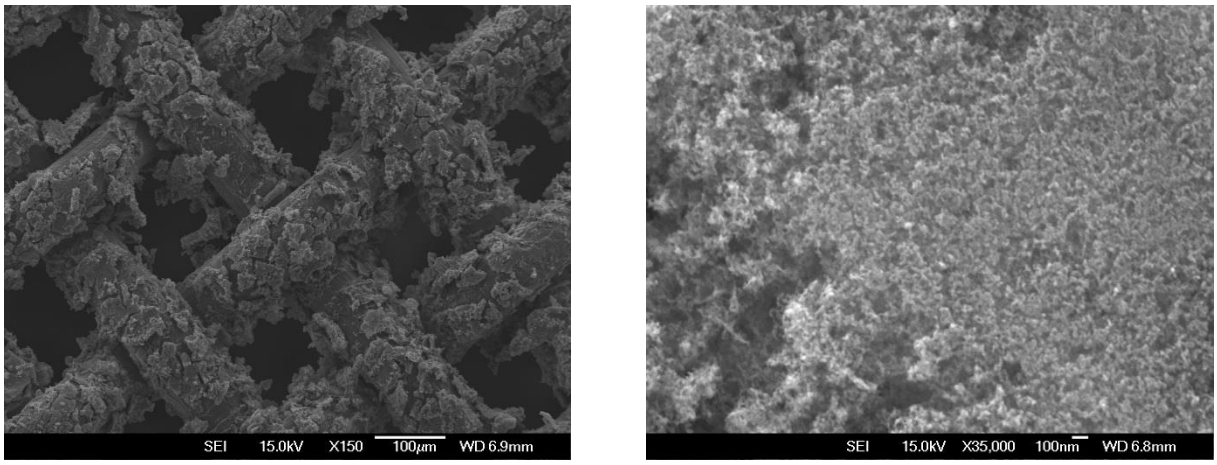

(a) (b)

Figure 9.12: Electrochemical deposition on precalcined mesh. Much of the structure deposited has cracked leaving gaps amongst the chunks remaining (a). Little of the platelet structure observed in the initial tests (Figure 9.07) was seen with a rough foam-like structure (b) and particle agglomerates as seen in washcoating (Figure 9.01) dominating.

Secondly, the calcination itself was targeted by applying temperature change intervals during heating. Previously, the temperature was raised from ambient to 400°C without applying any restriction for both the in reactor prepared washcoats or the tube furnace calcined electrochemical depositions. Now it was slowed and performed in the reactor by raising only in 75 °C intervals from 25 °C through to 400 °C. At each interval, the temperature was held for two minutes to allow the temperature to equilibrate before adjusting the setpoint to the next value. Overall this increased the heating time from about 20 minutes up to just over an hour. This changes the average temperature ramp from 25.3 $°C \cdot min^{-1}$ down to 10.8 $°C \cdot min^{-1}$. Whilst this did not prevent the cracking, almost the entire catalyst coating was retained post calcination (Figure 9.13), a substantial improvement on previous samples. Based on this success, a version of the interval heating using 80 °C adjustments was subsequently adopted for all calcination and reduction heating.

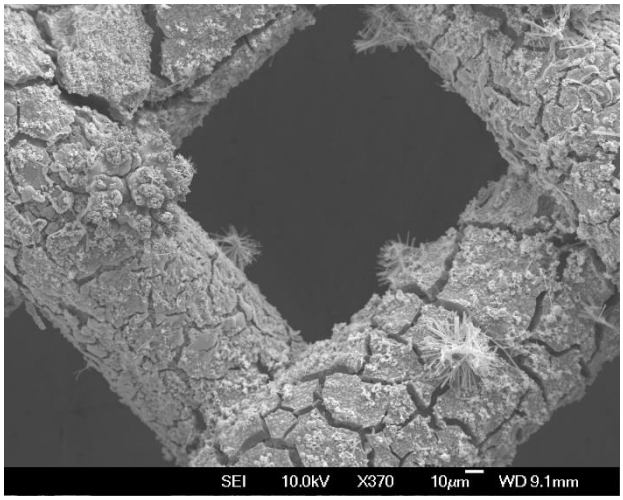

Figure 9.13: Electrochemical deposition catalyst coating produced using interval heating during calcination. Whilst cracking is still evident, almost all of the deposition is retained on the mesh.

The majority of the deposition was a foamy structure, similar to that produced in the precalcined trial, however it also featured some ultra-fine needle like structures (Figure 9.14) in the cracks. The length of the structures was less than 1 μm and the width is estimated to be less than 5 nm. The specific surface area of these would be extremely high, however this means that the durability is unlikely to be suitable for the purpose of the deposition. The interval heating deposition produced catalyst also possessed a number of previously unseen depositions consisting of long flat planes extending from a nucleation site in many directions (Figure 9.15). The cause of these structures was a mystery and the only explanation seems to be contamination of the solution. The area of the planes was very positive and the unique position protruding out from the surface gave greater exposure to the reactant gas flow. The position and high surface area of these structures is both a strength and a weakness. Whilst the structure is more exposed to the reactants, it is also more susceptible to entrainment.

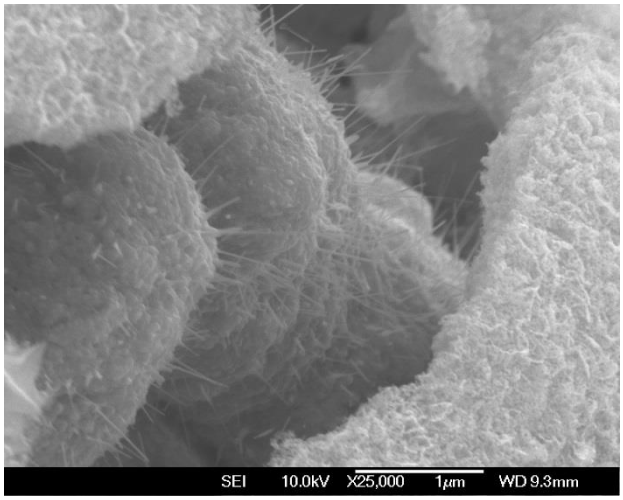

Figure 9.14: Ultra-fine needle like structures found in the cracks catalyst layer produced using the interval heating variation of electrochemical deposition. These needles are estimated at <1 μm long and 5 nm in diameter.

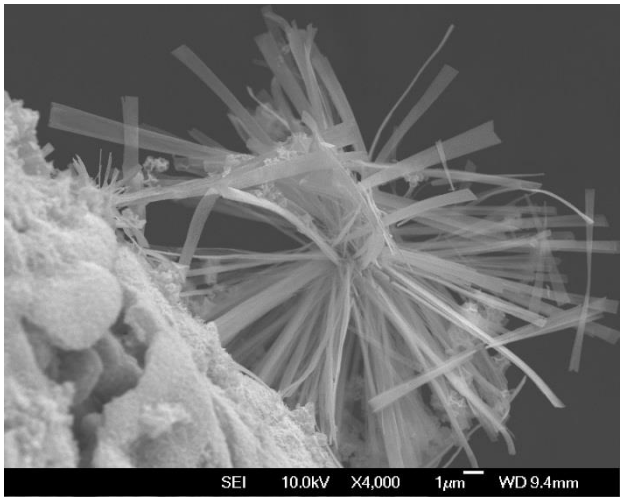

Figure 9.15: Unusual deposition found near the surface of the electrochemical deposition sample treated with interval heated calcination. Such a structure is likely to be the result of contamination causing the nucleation sites.

The third variation eliminated the calcination step altogether by directly reducing the deposition from $Co(OH)_2$ to metallic Co. Firstly, this retained the coating on the surface much better than the prior attempts suggesting that the calcination process was causing damage (Figure 9.16). On closer inspection, a very interesting structure was observed which appeared to be a network of particles where the platelets had previously existed (Figure 9.17). All of these particles seemed to be very small with no distinct shape but the specific surface area of the structure would be extremely high which is desirable in most catalytic applications. The only question would be the stability of such a structure when exposed to gas flows at elevated pressure for the Fischer-Tropsch synthesis

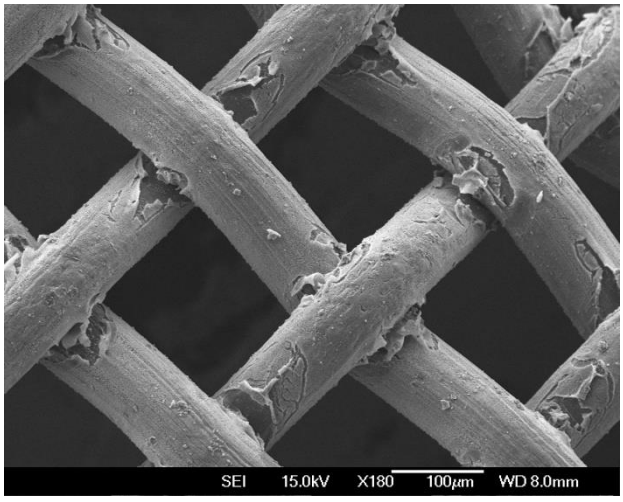

Figure 9.16: Retention of electrochemical deposition catalyst layer achieved by using direct reduction, rather than calcination followed by reduction. While some has split near the mesh intersections, along the wires is fully retained and undamaged.

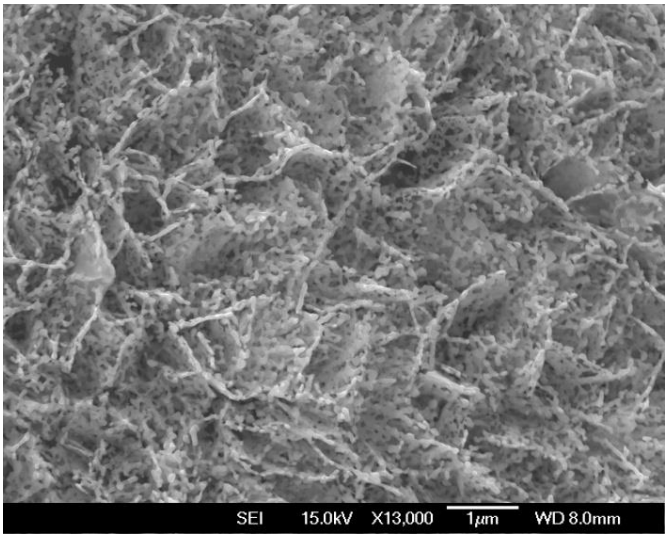

Figure 9.17: Close-up structure of directly reduced electrochemical deposition layer. Microplatelets as observed in the un-treated samples have been replaced by a network of small particles. While these particles have no distinct shape, the specific surface area of the overall structure is very high.

9.2.2. Electrochemical Deposition Catalysts on Nickel Foam

As with the stainless steel mesh, nickel foam was able to be successfully coated using the electrochemical deposition technique. The cell setup initially required some adjustment as the coating was uneven, favouring the side facing the counter electrode. It was believed that this was due to the voids through the nickel foam being longer and narrower than the equivalent in the mesh, resulting in reduced flow between sides. The successful coating contained the same green coloured micro-platelet structure (Figure 9.18) which coated all the surface of the foam well.

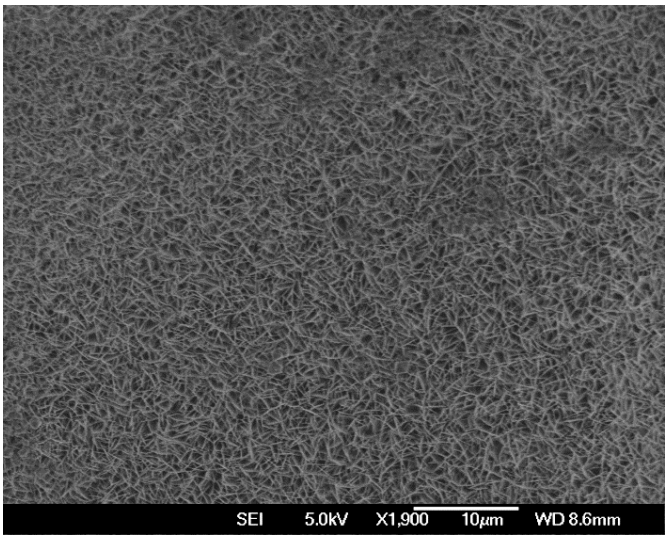

Figure 9.18: Array of microplatelet structures deposited onto the nickel foam support using the standard electrochemical deposition.

In an attempt to even the coating, a trial using a pair of counter electrode plates (Figure 9.19) was performed. However, the motion created by stirring caused the electrodes to come into contact due to the reduced spacing and this caused precipitation to occur rather than deposition onto the working electrode. The twin plates were replaced with a frame structure (Figure 9.20) to overcome the contact problem, however this interfered with the mixing and created a lot of turbulence around the sample so was considered undesirable. Perhaps the best way to conduct this would have been to have a ring around the outside of the cell acting as the counter electrode whilst sitting outside the flow created by mixing the solution.

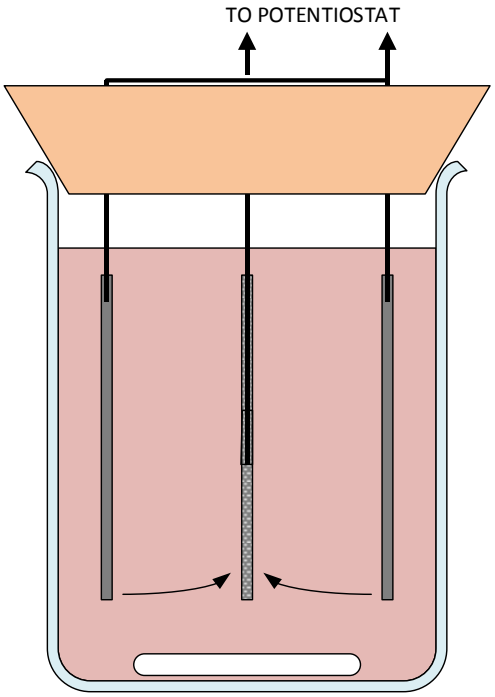

Figure 9.19: Drawing showing setup of the twin-plate setup trialled to coat both sides of foam samples more evenly. Due to poor anchoring, the stirring caused the counter electrode plates to move into contact with the working electrode as indicated by the arrows. As a result the precursor was precipitated out rather than deposited on the foam.

Figure 9.20: Frame structure adopted after failure of twin-plate setup shown in the cell with just the mesh electrode. The width of the frame is sufficient to fit outside the anchor wires for the working electrode (mesh).

9.3. Solution Combustion Synthesis Catalysts on Corrugated Mesh

Solution combustion synthesis was also used to produce a catalyst on the mesh. This coating was able to form a more uniform layer across the surface than washcoating. At low magnification (Figure 9.21) the layer looked to have a similar cracked shell to the many of the electrochemical deposition samples. Despite a promising distribution, the structure was still poor at higher magnification with particles morphed together creating a poorly defined shape (Figure 9.22). Whilst this, much like the washcoat catalysts, would make an excellent porous support structure, past experimental evidence suggests that it is not going to provide the desired Fischer-Tropsch activity.

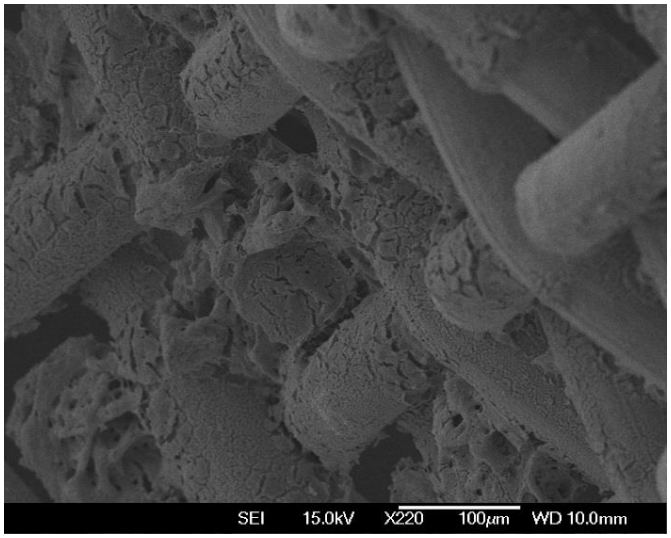

Figure 9.21: Cracked nature of solution combustion synthesis coating on mesh. While the coating is more even than washcoating method it is still very heavy. This is evidenced by the filled voids seen in several locations.

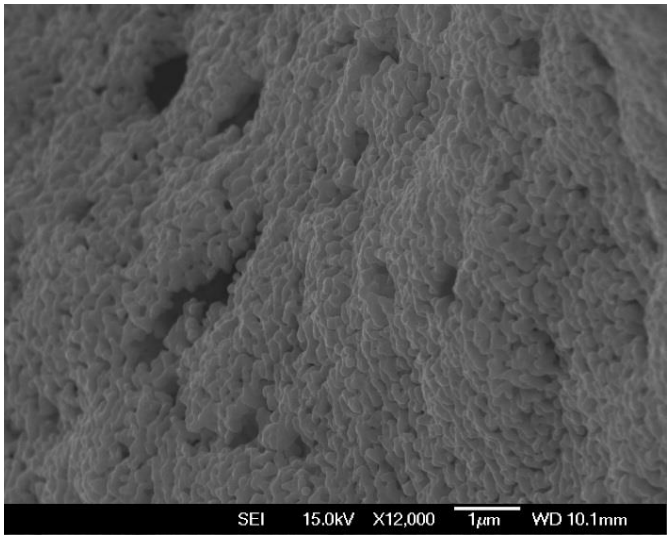

Figure 9.22: Particles produced by solution combustion synthesis on mesh. The particles have agglomerated similarly to the washcoated layers (Figure 9.01), resulting in these lumps of particles.

9.4. On-Line Performance Analysis

Several of the more successful catalyst depositions were reduced to active state and trialled in Fischer-Tropsch synthesis conditions to test their performance. None of the washcoat variations had produced suitable catalyst structures with predominantly large lumpy particles. As such these were not tested here since their lack of activity had already been demonstrated by Landers and Reijken [115, 116]. Four samples from the electrochemical deposition technique were tested, along with the combustion synthesis on mesh sample.

9.4.1. Electrochemical Deposition Catalysts

The first sample to be run in Fischer-Tropsch synthesis was the highly irregular structure observed on the electrochemical deposition sample prepared with interval heating during calcination. Given the sample's unique structure (Figures 9.13–9.15) was vastly different from anything which had been run previously and it was unknown how it would perform. As the left half of Figure 9.23 shows, the initial activity was quite promising yielding a CO conversion of over 30%. This was not to last as the activity very quickly deteriorated from this, with the conversion dropping below 20% within 45 minutes. The decline continued right down to only 2-3% after a 3-4 hours on line before becoming stable, however a conversion of this magnitude is undesirable. Had the initial activity held, the sample would have been much more promising.

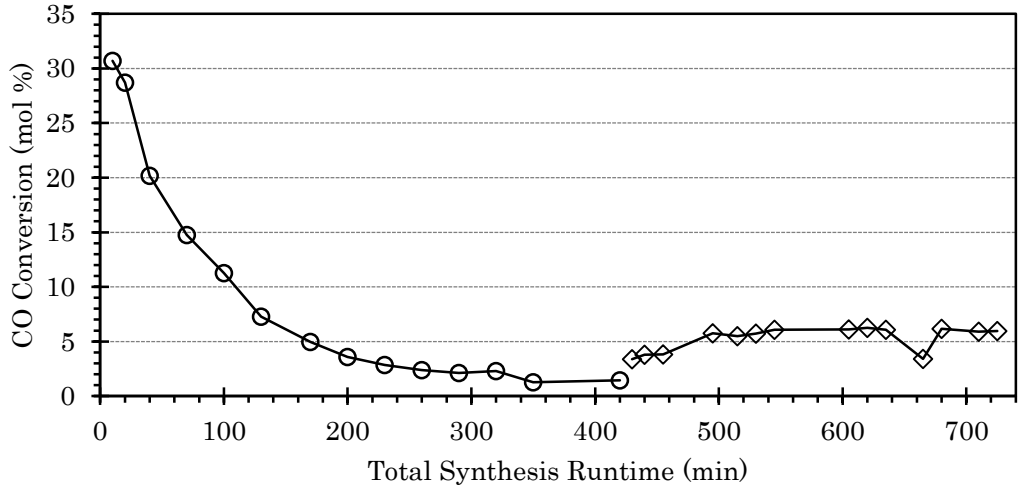

Figure 9.23: Variation in carbon monoxide conversion with time on stream for interval heating calcination variant of electrochemical deposition catalyst. An exponential decline in catalytic activity is very prominent during most of the first run (—o—), while a more consistent CO conversion of around 6% is maintained during the second run (—◇—).

After 7 hours (420 minutes) of runtime the first run with this sample was ended. The sample was re-reduced to the active phase using the standard reduction method to enable a second look at its activity. The right half of Figure 9.23 shows that the effect of reactivating the catalyst was positive, although the initial 30% conversion was not achieved again. The conversion in the second run was much more consistent than in the first with a level around 6% maintained after an initial period of increase. This indicates that there is potential for Fischer-Tropsch synthesis to be performed using this catalyst. However, firstly more work would need to be done to raise the conversion level and avoid activity declines such as that observed during the first run.

On-line analysis using the micro-GC during the first run, showed the presence of all 8 calibrated species in the reactor tail-gas stream, including methane, ethane and ethylene. The amount of ethylene was below the detector limit and therefore the C_2 olefin/paraffin selectivity ratio for the catalyst could not be calculated. Given the intended use of our product is as a fuel the ratio of olefins/paraffins is not important, but it can help to describe the catalyst's selectivity properties. After the completion of the run, only a few drops of product were present in the collection vial along with a few small drops of potential wax on the mesh. However, there was quite a significant quantity of particles, thought to be either catalyst or deposited carbon (coke).

Overall the Fischer-Tropsch performance of this sample was poor, with only light products able to be analysed. The lack of heavier products is quite likely to be a result of the rapid decline in catalyst activity, with only light products forming at very low conversions due to the lack of CH_2 units required for chain growth. This held true on the second run, with a very small quantity of methane the only hydrocarbon product detected.

The second sample to be run in Fischer-Tropsch synthesis was the first mesh sample to be coated by electrochemical deposition. The amount of coating retained on this sample had been poorer than that on the interval heating calcination sample, however it did contain more of the characteristic microplatelet structure, which was thought to have a high activity. This hypothesis was shown to be false however, as the initial activity was quite low (13%). Following the trend of the other electrochemical deposition sample, this declined away to <2% after around three hours. Beyond this point the conversion information is unreliable as the flow became unsteady and had to continually be adjusted. Periods of low flow correspond to an increase in conversion which is then lost again when the flow was stabilised to approximately 30 SCCM once more. This element of the experiment could have been improved by using an accurate flow controller, rather than manually operating valves. This would allow the system to respond in real time to fluctuations, avoiding the delays associated with adjusting and stabilising the flow manually.

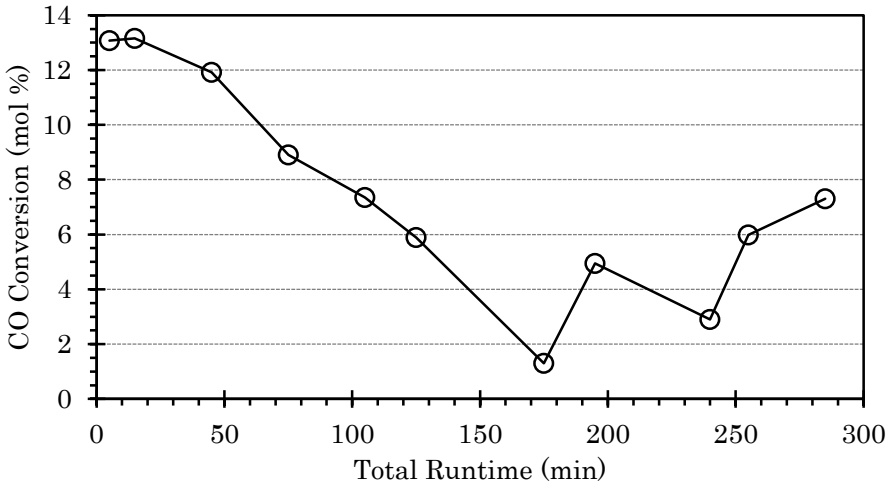

Figure 9.24: CO conversion during Fischer-Tropsch synthesis run of first electrochemical deposition catalyst. The conversion never reaches a high value, with the initial activity peaking at 13.2% before a steep decline to <2%. Low flow periods around 175 minutes and 240 minutes online resulted in steep gains in conversion. However this was lost when the flow was stabilised.

The flow was very unsteady during this run, with inlet flow measurements fluctuating between 21 and 35 normal $cm^3 \cdot min^{-1}$. This element of the experiment could have been improved by the use of an accurate flow controller, rather than adjusting the flow with manually operated valves. This would allow the system to respond in real time to fluctuations, avoiding the delays associated with adjusting and stabilising the flow manually.

Thirdly, what was thought to be the best coating of electrochemical deposition on mesh was trialled. After the previous runs, the current and coating duration had been optimised to -20 mA and 90 minutes respectively. Although it was produced using the original calcination method, without interval heating, this sample contained large quantities of microplatelets (Figure 9.07). Despite the large quantity of microplatelets, the high CO conversion seen at the beginning of the other electrochemical deposition sample runs did not occur. The resulting conversion profile (Figure 9.25) was markedly different to that of the other samples, oscillating up and down through the run rather than exponentially declining. This made it the longest lasting with a conversion of 4-5% recorded throughout the run on a level or slightly upward trend.

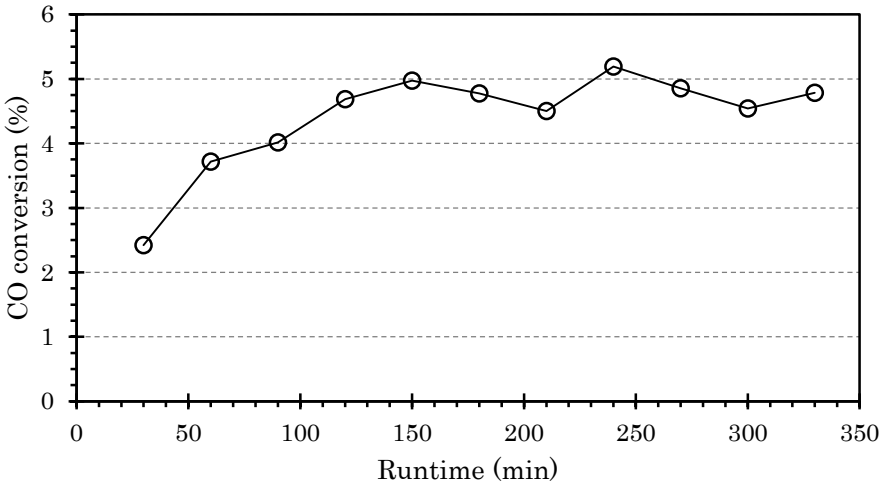

Figure 9.25: Performance of third electrochemical deposition catalyst in Fischer-Tropsch Synthesis. This variation never became very active. The conversion did rise slightly from the initial value, however the maximum it reached was barely above 5% which is too low. It did possess the best stability of the electrochemical deposition catalysts, with no decline in activity.

The final electrochemical deposition sample tested in Fischer-Tropsch synthesis was one prepared on nickel foam. The support had a high surface area and the preferable microplatelets were the dominant form of deposition, so strong performance was expected. Additionally, co-catalysts containing both cobalt and iron have been shown to be beneficial in the right ratios, so the same could be true for a combination of cobalt and nickel. Given that the ratio of the components was important, using the second metal as a support may not create the same effect(s). If this occurred, it would be expected that the resultant catalyst would exhibit a mixture of the properties of each component. Combining nickel's methane selectivity with cobalt's preference for long chain waxes in the right proportions could create a catalyst selective to alkanes in the fuel range which would be ideal for small scale Fischer-Tropsch targeting liquid fuel production.

The resulting performance however, was disappointing with a very inconsistent conversion level (Figure 9.26). After the initial low conversion period for the first 35 minutes, an average of 6.55% can be observed as a baseline. Fluctuations draw the conversion up or down periodically, after which it returns to the baseline. This stable behaviour would be ideal, if it were to accompany a baseline conversion substantially greater than 6%. The fluctuations in the conversion activity were not correlated to the flow with increases in the conversion occurring at both high and low flow rates.

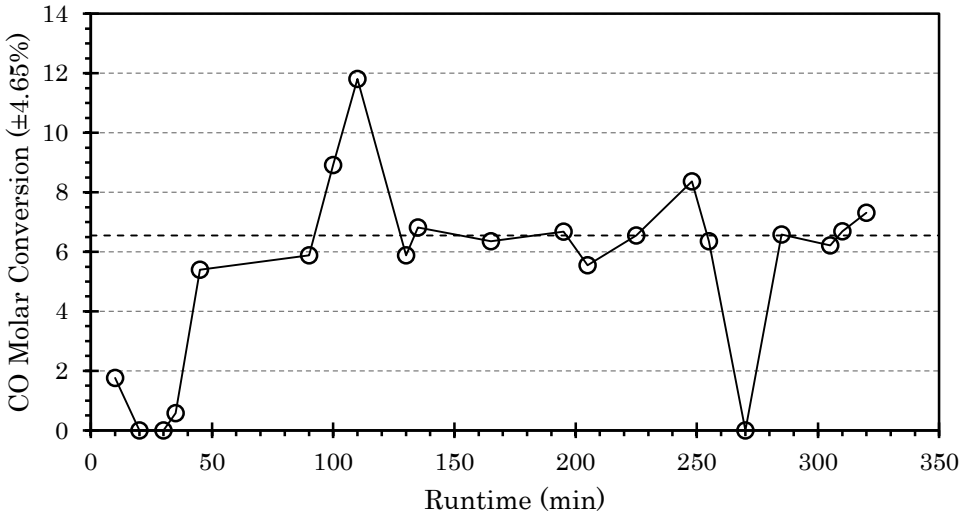

Figure 9.26: Conversion profile of electrochemically deposited cobalt catalyst on nickel foam support. The behaviour is unpredictable with oscillations from the average (– –) of up to ±100% of the value. Whilst the stability to return to average is desirable, the low conversion is not.

Overall, the electrochemical deposition catalysts exhibit a short active lifetime with CO conversions unable to be maintained above 10% for more than 2-3 hours, even in the best samples. This makes them unsuitable for a Fischer-Tropsch reactor system as multiple catalysts would be required for the duration of a single run. In addition, the low average conversion of 5% over an extended time across the tested samples is not going to provide the desired productivity for a small scale system. The low conversion, coupled with the short runtime of the samples also prevented any substantial product formation. As a result, no liquid product analysis could be performed for these catalysts. All of the samples were able to produce some methane, although some did not produce enough to exceed the minimum detector limit to be measured by the on-line GC. Most samples were able to generate ethane, although the amount of this was almost always below the detector limit. The first run of the interval heating sample was the most active in this regard, producing detectable amounts of ethane (up to 0.4%) and clearly visible peaks for ethene.

9.4.2. Solution combustion synthesis catalysts

A solution combustion synthesis coating on a woven mesh support was also trialled in the reactor. This performed better than the washcoated samples however was unable to provide lasting conversion activity (Figure 9.27). The initial readings indicated a strong conversions of 17.2% which would be suitable for a catalyst if maintained. However this catalyst declined in a very similar exponential decay curve to the interval heating electrochemical deposition sample, becoming inactive after just over two hours. This lifetime is unsuitable for the Fischer-Tropsch system as the catalyst cannot be recharged every 2 hours during a run without making operation complex and expensive.

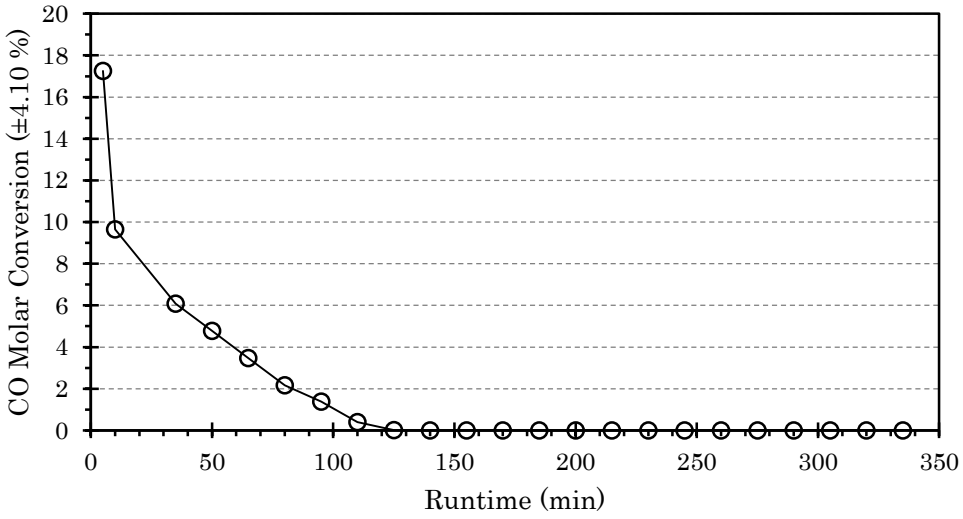

Figure 9.27: CO conversion profile of solution combustion synthesis catalyst on woven stainless steel mesh. The initial activity is promising however it declines rapidly to become inactive after 2 hours and remains inactive thereafter.

This sample also failed to produce any detectable quantities of product, with CO_2 the only one to have a visible peak in the on-line analysis. This is most likely not even a product with small amounts of CO_2 remaining in the lines from the air in them during assembly and traces existing in the model synthesis gas supply. The activity and product yield match the expectation based on the SEM imaging of the deposition which did not form the desired fine particles when applied to the mesh reactor.

9.5. Analysis of Support and Block Reactor Runs

Using the support and block reactor design, the various catalyst depositions onto the internal support structures (corrugated woven mesh and metallic foam) failed to produce a catalyst with the desired structure and activity. Given the number of different catalyst depositions trialled, the cause of failure seems to be related to the reactor design rather than the deposition techniques.

Potential faults arising from the design include: catalyst entrainment, flow distribution and channel dimension effects. The first two of these are related to or dependent on the flowrate which is able to be adjusted during operation, while channel dimension effects will have an influence at any flowrate. Given the amount of catalyst retained on the support structures after the runs and the very small quantities of particles recovered from the product collection vial, catalyst entrainment seems unlikely to be the problem. Flow distribution was considered more thoroughly, with some experiments done to examine the flow profile across the channel. To do so a second feed-plate design was manufactured utilising a different flow distribution to the original plate (Figure 9.28). The plates were then compared in a tracer study using a mock channel made of transparent acrylic, water and coloured dye.

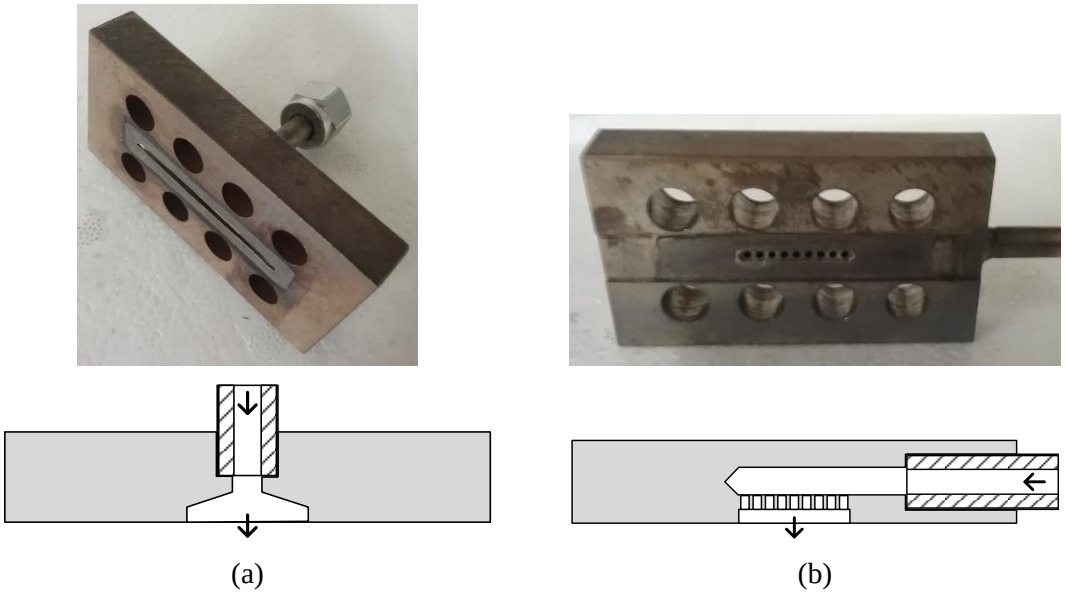

(a) (b)

Figure 9.28: Original (a) and alternate (b) feed-plate designs with the manufactured part (above) and cross-sections showing the flow distribution path (below). For the cross-section drawings of the plates: gas flows in the direction of the arrows from the feed tube (hatched) through the void space in the plate (grey) out into the channel. Cross-sections are representative only and features are not to scale.

From the tracer study it was identified that the original design was weak at elevated flowrates with significant channelling occurring down the centre of the channel and weak eddy mixing at the sides. The alternative design created an almost ideal plug flow model at moderate flow rates and it started to resemble a laminar flow profile at higher flows. An attempt was made to verify this behaviour in the gas phase using smoke as the indicator however a clear result could not be observed. While the gas phase mixing is likely to be different to that of the water, it was believed that the new design would still offer improvement. Therefore, it was used in the Fischer-Tropsch runs done after this test (Table 9.1) to maintain uniform reactant distribution across the channel.

Table 9.1: Fischer-Tropsch runs performed (by catalyst name) and the feed endplate design used. (2)* indicates the re-run of the catalyst to investigate the re-reducibility.

CATALYST DEPOSITION	ENDPLATE DESIGN
Interval Heating Electrochemical	Original
1st Electrochemical on Mesh	Original
Best Electrochemical on Mesh	New
Electrochemical on Nickel Foam	New
Interval Heating Electrochemical (2)*	New
Combustion Synthesis on Mesh	New

With the issue of flow distribution having been examined and producing no improvement in the results, the only remaining cause of poor behaviour is the channel dimensions. Compared to the previously successful microchannels with dimensions of 0.3 mm x 0.3 mm the dimensions of this channel at 2 mm x 20 mm were substantially larger. Penniall [3] had considered this however had determined that the channel diffusion effects were minimal for hydraulic diameters of up to 4-5 mm. The problem however is not with the gas reaching the catalyst but rather with the catalyst formation, when a solution based or washcoating procedure is used. In the small microchannels used by Penniall where the channel size is 0.3 mm x 0.3 mm, the maximum particle size is restricted by the dimensions. Additionally, the heat transfer through the fluid in the channel during drying and calcination processes is much faster. It is expected that this has the benefit of preventing droplet merging in the channels and the subsequent formation of large agglomerate particles. This was evidenced when the solution combustion synthesis on mesh sample was prepared. This resulted in lumpy depositions inside the channel, while outside the channel small droplets of excess solution formed a very fine crystalline powder similar to that produced by Toniolo et al. (Figure 9.29) [100]. Unfortunately this powder was too fragile to collect for SEM examination so the existence of ultra-fine particles could not be verified. Further work could examine this by testing the particle sizes formed using droplets of solution on aluminium foil to compare the particle sizes for different film thicknesses and droplet sizes.

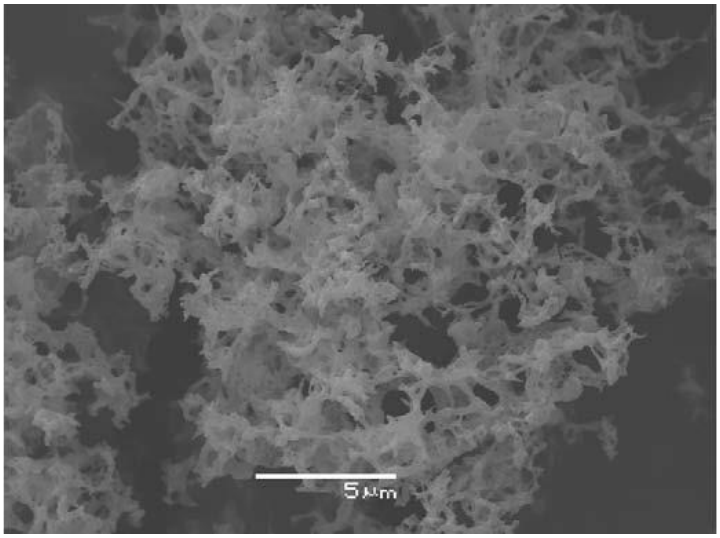

Figure 9.29: Ultra-fine cobalt oxide structure produced by Toniolo et al. [100] using solution combustion synthesis with glycine (NH_2CH_2COOH) as the organic fuel. While this is different to the urea ($(NH_2)_2CO$) used in this experiment the ultra-fine structure produced could be very similar.

10.0. Microchannel Plate Reactor Results and Analysis

Given the lack of success with the larger channel and support design, a decision was made to pursue options with the original microchannel plate design. As with the support and block design, the catalyst structures formed were analysed prior to the Fischer-Tropsch synthesis performance. For this design catalysts were formed using only the washcoating and combustion synthesis methods, with electrochemical deposition not well suited to the design. The coatings and their deposition were compared on both the original 0.3 mm wide channels and plates with a mixture of channel widths up to 3.3 mm, to determine the effects of the channel dimensions. Again, the catalysts were analysed for structure and shape using SEM in addition to testing their Fischer-Tropsch synthesis performance.

10.1. Washcoat Catalysts

The standard 1:1 mass washcoating solution was used to prepare the catalyst depositions inside the channels as per section 8.2.1.1. Penniall's work [3] showed that this simple technique could produce the desired structures on the microchannels and it was intended to initially replicate and later expand on that result with these experiments. The replication verifies that the technique is valid and gives a baseline for the modelling and scale-up calculations.

For examining the formations, a microchannel plate with a mixture of channel widths from 0.3 mm up to 3.3 mm in width (Figure 10.01) was prepared by removing divider bars from a channel plate. Forming wider channels by removing the dividers avoided the expense of cutting new plates which Penniall [3] lists at $36.80 per channel plate (on the basis of cutting 42 at once). It also fixed the widths of the possible channels to the function W = 0.3+0.6n where n is the number of dividers removed since removing a divider added the width of the divider plus the width of another channel. The resulting channel widths and the number of each width used are given in Table 10.1.

Table 10.1: Channel widths and the number of each width featured in the multi-width channel plate.

DIVIDERS REMOVED	CHANNEL WIDTH (mm)	NUMBER OF CHANNELS
0	0.3	12
1	0.9	4
2	1.5	2
3	2.1	2
4	2.7	2
5	3.3	1

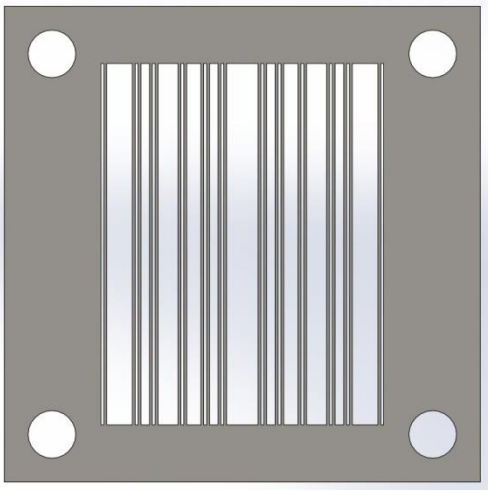

Figure 10.01: SolidWorks model of multi-width microchannel plate for washcoating. Different width channels are arranged symmetrically to ensure the flow remains even across the width of the plate.

Across the plate, various coatings were observed. In particular, the variation across the wider channels was significant (Figure 10.02), with a notable difference in the depositions observed near the channel wall (Figure 10.03a) and those observed near the centre (Figure 10.03b). The deposition near the edges forms a rough textured structure, resembling those produced by electrochemical deposition, with thin surfaces forming various size voids (Figure 10.04). In the centre however there was a complete absence of fine structure, with only bulk blocks of deposition. This suggests that of the channel dimensions, specifically the distance from an edge (Figure 10.05), are important to the catalyst formation. This supports the poor formations in the support and channel block reactor (design #1) where the distance from the channel edge is large in comparison to the microchannels in these plates.

The channel dimension cannot be considered the only factor, as the volume of solution is significantly smaller and the heat transfer (during drying and calcination) is enhanced due to the thin channels. Consideration should also be given to the fact that (most of) the deposition is occurring on aluminium foil gasket layers and not the stainless steel (mesh) or nickel (foam) surfaces used in the larger channel and a support interaction may be present. The aluminium foil effect is unlikely to be the cause however as Reijken [116] tested the deposition on corrugated aluminium foil and obtained similar results to the mesh.

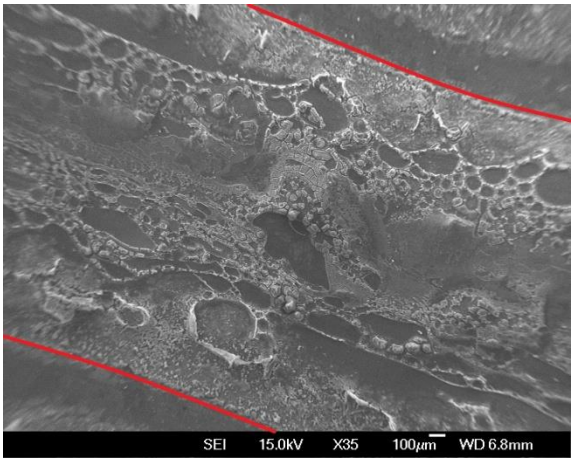

Figure 10.02: Low magnification image of washcoated catalyst from a 2.1 mm microchannel showing the variation in structures formed across the width of the channel. Red lines indicate the position of the channel wall during coating. Note: Outer regions of the image are distorted due to the low magnification.

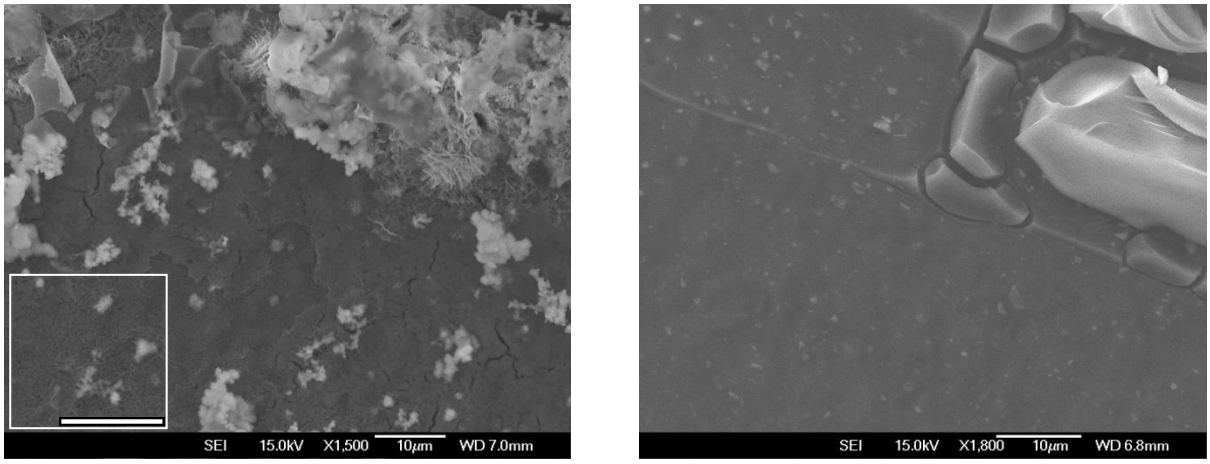

(a) (b)

Figure 10.03: SEM images of the catalyst deposition structure formed near the wall (a) and near the centre (b) of the channel in Figure 10.02. The structure near the wall (a) shows evidence of high area structures and possibly the "fibril" structures observed by Penniall [3] in the lower left (see inset). Conversely, the structure near the centre of the channel (b) shows a bulk deposit with no fine structure.

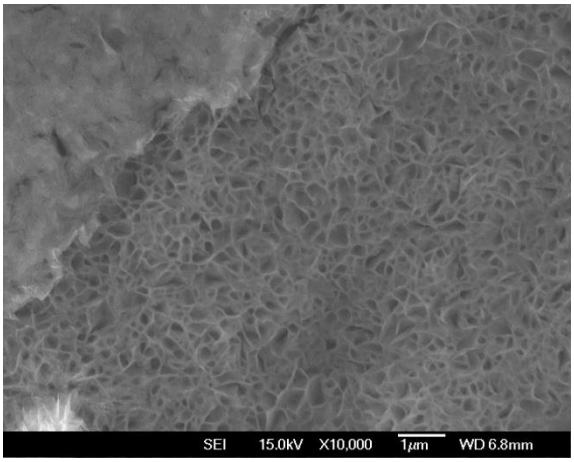

Figure 10.04: Structure of washcoat deposition near the edge of a channel in the multiple width channel plate. The structure has a rough texture and large voids somewhat similar to those in the electrochemical deposition technique used for coating the mesh support structure.

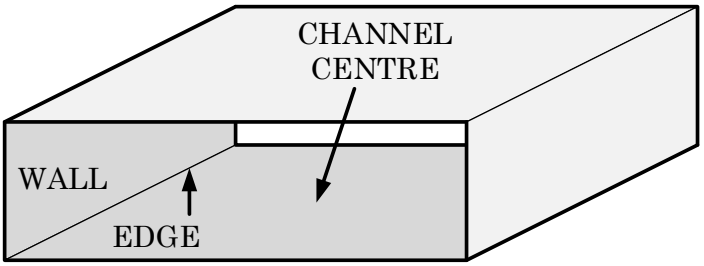

Figure 10.05: Relative position of channel wall, edge and centre as used to describe the catalyst formation positions. Most the SEM images look down at the bottom of the channel between two walls.

Firstly, a standard microchannel plate with 50x 0.3 mm channels was prepared. This design was taken directly to Fischer-Tropsch synthesis testing since it had previously been studied by Penniall [3] and many of the channels remained in the multiple width plate. A suitable visual characterisation of the structures could be determined during the SEM analysis of the multiple width plate. SEM images showed a rough textured coating (Figure 10.06a) in these channels at various positions across the plate. At higher magnification the finer "fibril" structure (Figure 10.06b) could be seen in some areas of the coating layer however it was less evident than in Penniall's work [3].

Some difficulty was encountered during the first attempt at forming the solution combustion synthesis coating as the heating elements failed during heating to the calcination/combustion auto-ignition temperature. This was initially considered wear as the element had been used many times before and so it was replaced with a new one. A problem was discovered when the new element failed in exactly the same way during its first run. It was considered that due to the large thermal mass of the outer cover plates that the heating load was exceeding the limit of the element and causing it to short. Therefore an interval heating schedule, similar to that used for the calcination of the electrochemical deposition catalysts on mesh was implemented. This prevented the problem from occurring again and did not impact on the activation of the combustion step during the synthesis, becoming the standard method.

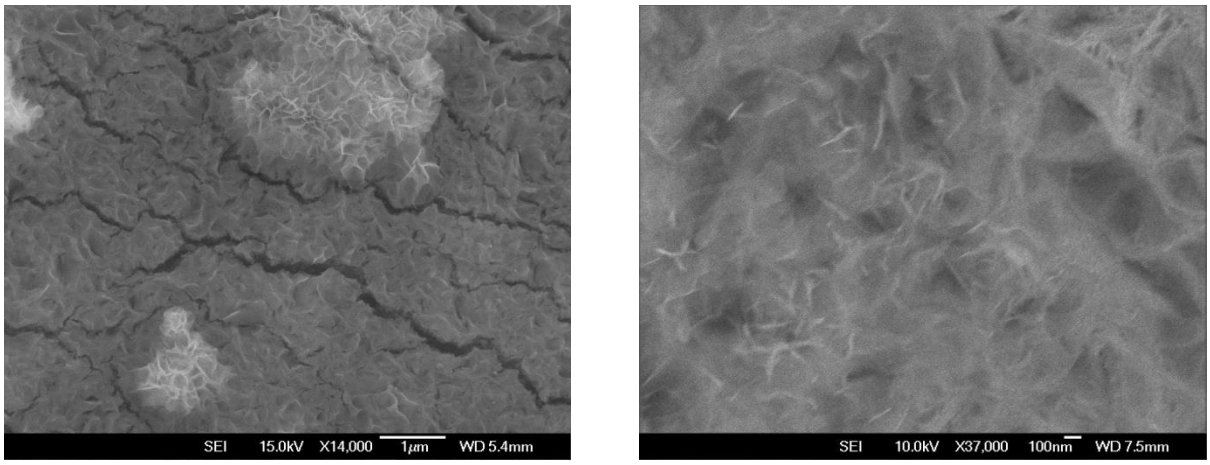

(a) (b)

Figure 10.06: SEM images of formations in 0.3 mm wide channels in the multiple width channels plate showing the general structure (a) and fine fibrils (b) of the deposition. It is assumed that these images are representative of the formation in the same width channels in a plate with channels of only this width.

As the channel width increased, the amount of high area structure (Figure 10.06) decreased and the amount of poor formation (Figure 10.03b) increased. Some of this is attributed to potential bubbling of the solution evidence by structures seen in the widest 3.3 mm channels (Figure 10.07). Nearer the wall in the same channel useful formations (Figure 10.06) could still be seen suggesting that there was limit to the distance from the edge of the channel. Figure 10.08 shows how near the edge of a channel fine structure can be seen but beyond a certain distance the solution is prone to bubbles and poor formation.

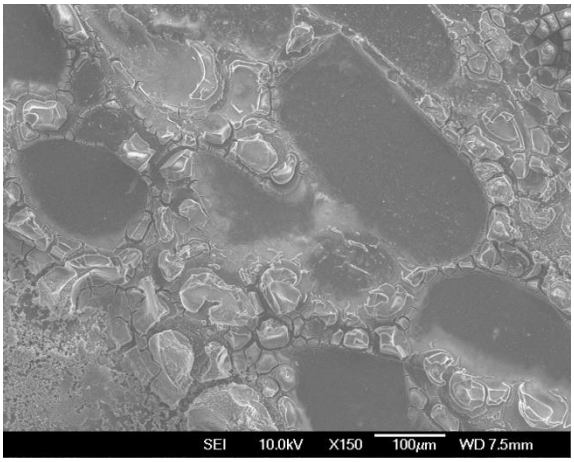

Figure 10.07: Regions of coating with thin centres and lumpy regions around the outside which suggest the presence of bubbles in the channel as seen in the middle of a 3.3 mm wide channel.

Examining the moderately sized 0.9mm channels, the edge effect became more apparent with distinct bands of formation occurring (Figure 10.09). A rough area near the wall is followed by a very uniform strip before a wide band of large blocks in the centre of the channel. It is thought that the area in the first two bands is suitable for catalyst while the central band is too lumpy and possesses little microstructure.

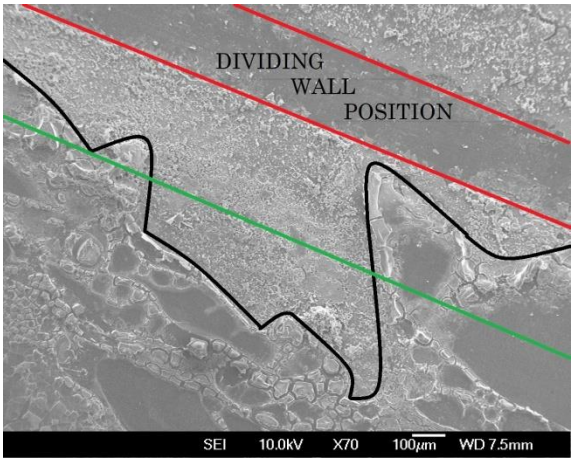

Figure 10.08: Image indicating the expected good formation distance from the channel wall position. Good formation can be seen in the area between the red wall line and the black line (plus potentially some areas beyond it). Based on this an average good formation distance (green line) can be predicted and from the image scale appears to be close to 400 µm.

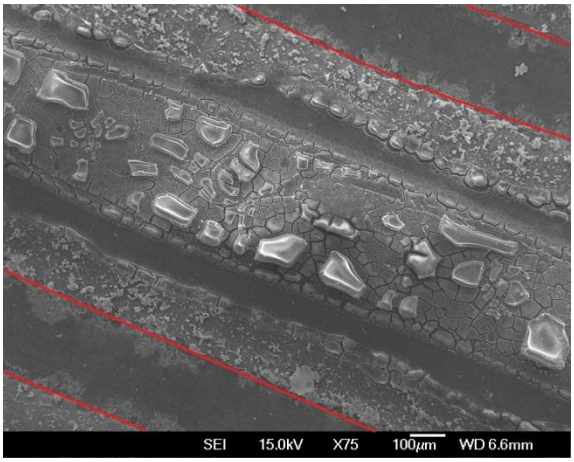

Figure 10.09: SEM image of a 0.9 mm channel in the washcoated plate. The banding in the deposition is obvious with five bands visible. The outer bands containing small particles and the narrow strips of thin coating are more desirable than the central blocks of deposit. Red lines indicate the position of the dividing bars between adjacent channels.

In general, the washcoat of the microchannels did not prove to be successful in the channels tested with a widths above 0.3 mm. This means that this coating cannot be used if the channels are widened to improve manufacturability. Therefore, scaling up the reactor using this catalyst coating method would be difficult and expensive. Increasing the flow through the reactor would require many parallel plates of channels which would drive the cost up by requiring more plates and reactors. The cost of such a reactor is even greater when including the cooling layers between the channel layers. Considering a cooling layer as a distribution plate and a cooling channel plate, the cost of a single reactor with 10 parallel layers would be approximately $690 (Appendix D).

Even with 10 channel plate layers, the total throughput at constant channel velocity would be 300 SCCM (18 $SL \cdot h^{-1}$) which is well short of the 10 $SL \cdot min^{-1}$ (600 $SL \cdot h^{-1}$) goal. This would require in excess of 30 reactors in parallel which takes the total cost to over $20 000 which is completely unfeasible, particularly considering the low CO conversion achieved of 20-25%.

10.2. Solution Combustion Synthesis Catalysts

Solution combustion synthesis was used to prepare an alternate catalyst deposition in similar microchannels to those used for the washcoating. Again the first testing was completed by coating a plate with multiple channel widths (Table 10.2) for the examination of the technique in terms of forming effective depositions. The aim of this was to confirm or the potential of this technique for coating wider channels, ideally with widths in the 1.5-2.1 mm range. Narrower 0.9 mm and 0.3 mm channels were retained for confirmation of the catalyst formation in those ranges.

Table 10.2: Number and size of microchannels formed in multiple width microchannel plate coated by solution combustion synthesis catalyst. Again dividers were removed to widen the channels rather than cutting a new plate. Channel widths were arranged evenly across the plate to ensure even flow.

DIVIDERS REMOVED	CHANNEL WIDTH (mm)	NUMBER OF CHANNELS
0	0.3	10
1	0.9	8
2	1.5	4
3	2.1	3

The results of this technique were the most pleasing yet with the coating achieving a high consistency across the plate and within most of the channels (Figure 10.10). The exception to this is in the widest 2.1 mm channels, where the same bubble influence patchy structure seen in the washcoated channels was observed. Despite the poor general appearance in the wide channels the microstructure was still promising in the centre of the bubbles (Figure 10.11).

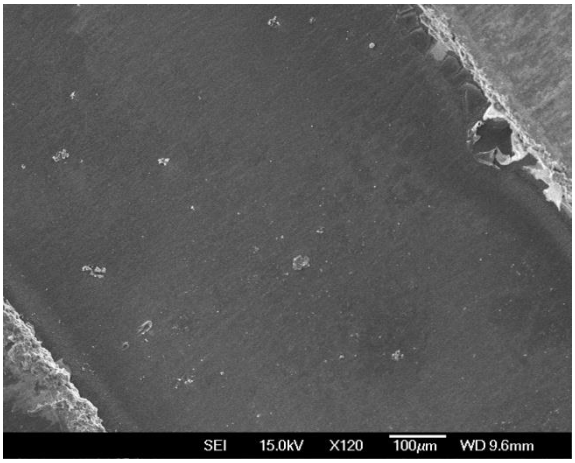

Figure 10.10: Consistency of the solution combustion synthesis catalyst deposition within a 0.9 mm wide channel representative of many of the channels across the multiple width channels plate.

While the coating was good across all of the widths, inconsistent formations were more prevalent in the wider channels (1.5 and 2.1 mm) than the narrower channels (0.3 and 0.9 mm). The narrower channels also contained the finer microstructures including fibrils and a honeycomb structure resemblant of that formed by electrochemical deposition (Figure 10.12). Based on this information it was chosen to continue with 0.9 mm wide channels for Fischer-Tropsch synthesis testing as the manufacturability should be easier and less costly than 0.3 mm channels. While channels of 1-1.5 mm were a possibility, the catalyst formation in the 1.5 mm channels was too inconsistent to be sure of its reproducibility and performance.

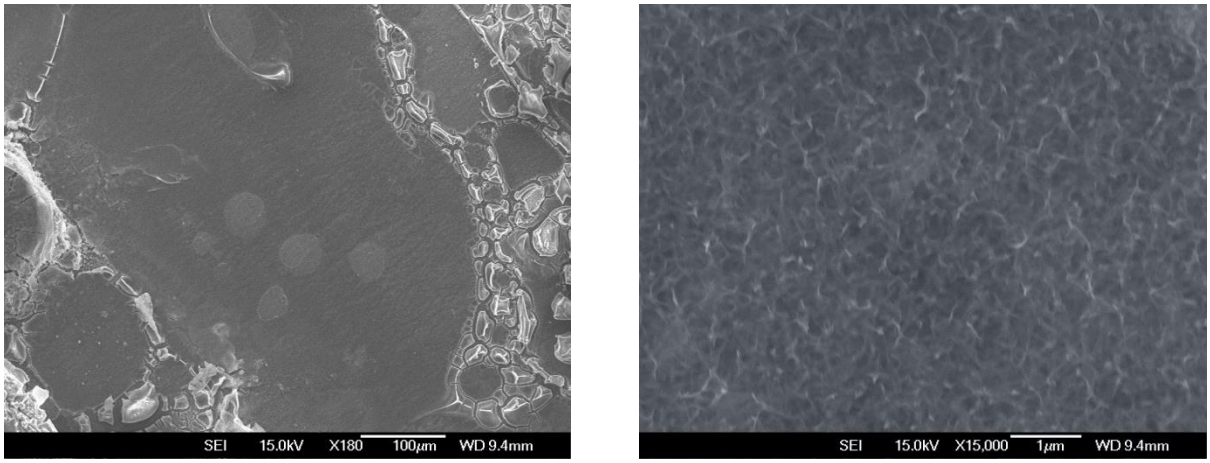

(a) (b)

Figure 10.11: Bubbles hindered the general formation of the deposition in the widest 2.1 mm channels when using solution combustion synthesis (a). However, fine microstructure (b) was still observed in the bubble centres, another indication that this technique is out-performing the washcoating.

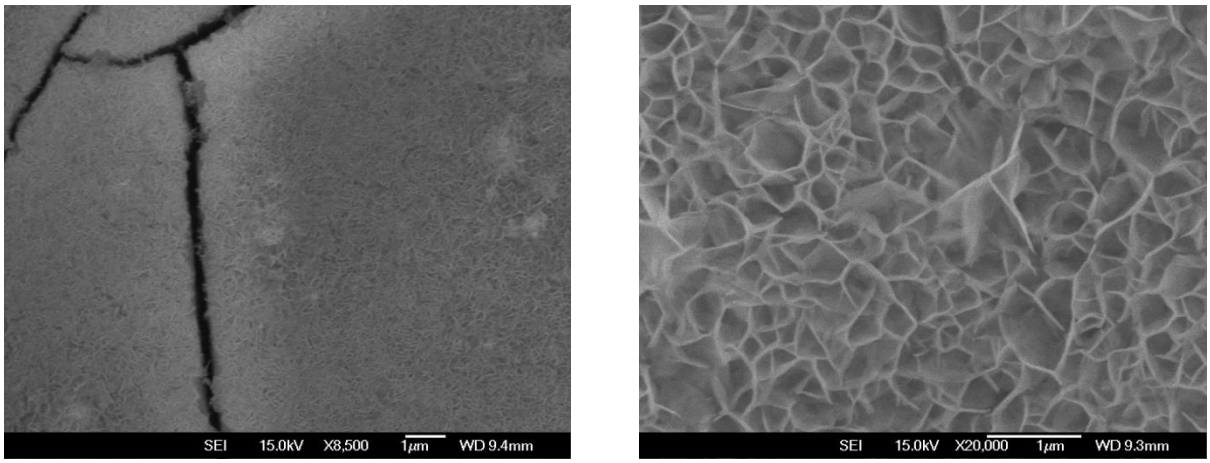

(a) (b)

Figure 10.12: Finer microstructures formed in the narrower 0.3 mm and 0.9 mm microchannels using solution combustion synthesis included fibrils (a) and a honeycomb like platelet structure similar to the electrochemical deposition catalysts (b).

The coating from the solution combustion synthesis showcased a much higher potential for scale-up than the washcoating. The distribution of catalyst throughout the channels was much more uniform and had a higher probability of containing one of the known active fine microstructures (fibrils, platelets). Given the application of a similar catalyst formation technique to Velocys commercial reactors it clearly shows significant promise as a catalyst for microchannel reactors [34, 53].

10.3. On-Line Performance

As with the catalysts formed on the support structures for design 1, the deposited catalysts were tested for Fischer-Tropsch performance. The first indicator of performance was made while the system was on-line by chromatographic analysis of the tail-gas exiting the reactor system. This analysis enabled calculation of the CO conversion and showed the production of C_1 and C_2 hydrocarbons.

10.3.1. Washcoat Catalyst

The on-line analysis of the first run with the washcoat catalyst showcased the enhancement made by using the microchannels over the alternate design with the mesh support. After a short initial settling period the production of methane and later ethane was detected, with the quantity of both increasing over the duration of the run. It is likely that some of the initial settling period was not actually inactive but simply the amount of product being produced was below the detector limit of the micro GC during that period. The CO conversion was much higher over the duration of the run than that attained by any of the catalysts in the other design, remaining above 15.00±3.13% for the entirety of two sequential runs (Figure 10.13).

The second run was completed at a higher pressure than the first to compare the performance between 10 and 20 bar of pressure in the system. The difference was small, matching the behaviour determined by Penniall [3] which fitted the same trend as that published by Yates and Satterfield [113] for a powdered catalyst in a slurry. The maximum conversion was elevated, however the general trend in conversion was similar to the first run. Unfortunately the run was cut short due to a power outage and the longer term performance could not be compared. Since a positive difference, albeit a small one, was observed the higher 20 bar operating pressure was implemented for subsequent runs. The higher pressure should also aid in experiments with wider channels by raising the partial pressure and diffusivity in the channels, thus resulting in more reactants reaching the active sites.

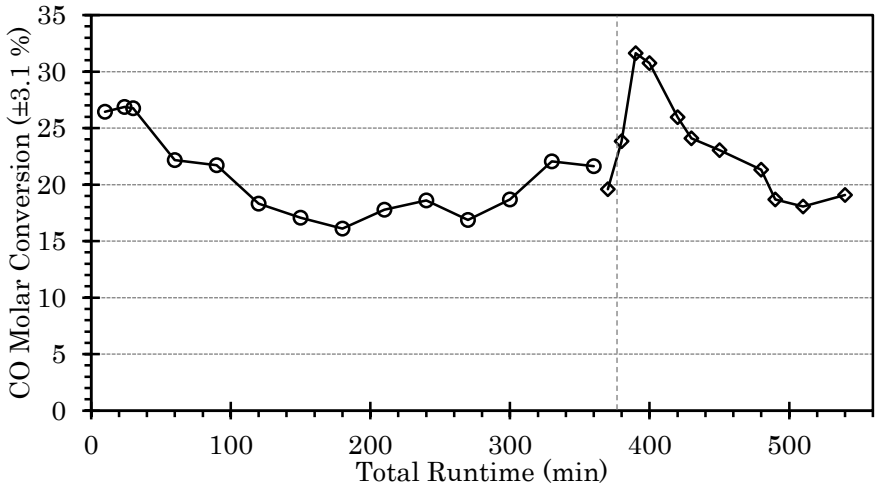

Figure 10.13: CO conversions attained for Fischer-Tropsch synthesis runs performed with the washcoat catalyst in 0.3 mm microchannels. The first run (circles) was performed at 10 bar and the second run (diamonds) was performed at 20 bar. Both generated pleasing conversions averaging over 20.0±3.1%. Stated uncertainty for conversion is the average uncertainty over the entire run.

10.3.2. Solution Combustion Synthesis Catalyst

The solution combustion synthesis catalyst was run in the modified channels with 0.9 mm widths. The resulting performance was very positive with the catalysts showing all the indicators of activity in the on-line analysis. The conversion attained by the catalyst over both of the two runs was consistent and above 30.0±2.4% for the entirety (Figure 10.14). After approximately six hour both runs finished above 40.0±2.4% conversion, with the performance holding steady.

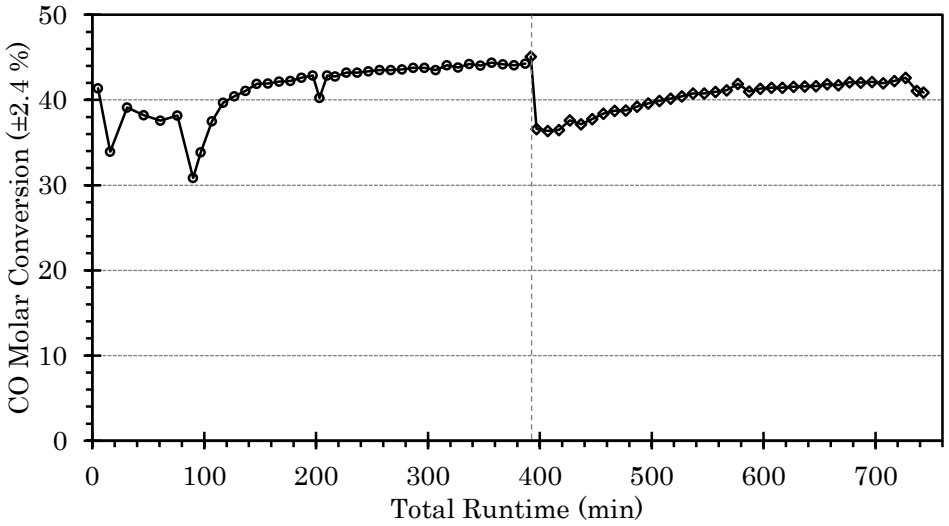

Figure 10.14: CO conversion of initial and second runs of solution combustion synthesis catalyst in 0.9 mm wide microchannels. The change between the first (circles) and second (diamonds) runs occurs after 390 minutes (dashed) and the resulting drop at the beginning of the second run is undesirable. Stated uncertainty for conversion is the average uncertainty over the entire run.

Interestingly, the conversion dipped at the beginning of the second run, dropping by nearly 10%. This is the opposite behaviour to that seen in the trials with the washcoated catalyst and with the electrochemical deposition catalyst which both increased in productivity after being taken off-line and then regenerated. This could be described by product wax condensing inside the reactor and covering the catalyst after the end of the first run when the reactor was cooled and depressurised. Since no solvent wash was applied to the reactor, this layer has remained and the conversion attainable in the second run is reduced. If the catalyst was being used for a commercial run rather than a short test run this would not be much of a problem as the duration of the run would be much longer. A potential modification to aid the prevention of this would be to mount the reactor with the channels running vertically rather than horizontally so that any condensing waxes run out the end of the channels under gravity.

Production of methane and ethane was significantly higher than any other catalyst/reactor combination reaching as high as 3.20±0.10% and 0.47±0.10% of the tail gas respectively. This is approximately five times the methane and eight times the ethane that the washcoat in 0.3 mm channels was able to produce (Table 10.3). This seems more impressive when compared to the only active catalyst from the other reactor, the electrochemical deposition, which produced only one eighth of the methane and one tenth of the ethane. A greater increase in the ethane production than methane production suggests an improved ASF α value which is desirable to decrease the yield of gaseous products while maximising the yield of liquid fuel weight products.

Table 10.3: Highest molar percentage of methane (CH_4) and ethane (C_2H_6) detected in the tail-gas stream exiting the Fischer-Tropsch reactor for different catalyst and reactor combinations.

REACTOR/CATALYST	**METHANE** ±0.10 mol%	**ETHANE** ±0.10 mol%
Mesh Support/ Electrochemical Deposition	0.41	0.04
0.3 mm microchannels/ Washcoat	0.58	0.06
0.9 mm microchannels/ Solution Combustion Synthesis	3.24	0.47

The next step for scale-up was to verify the viability of the coating on multiple stacked layers of channels. This was examined by trialling a stack of three plates with the original 0.3 mm wide channels with alternating distributing plate and channel plates in the stack. The standard process for solution combustion synthesis was used to prepare the catalyst coating which was used directly for Fischer-Tropsch synthesis testing. The performance of this coating was very pleasing with an almost constant 42.0±2.3% conversion held for the duration of the run after the first two hours of settling time (Figure 10.15). This is very similar to the second run of the 0.9 mm channels which also took a short settling period before moving into a near constant conversion above 40% (Figure 10.14).

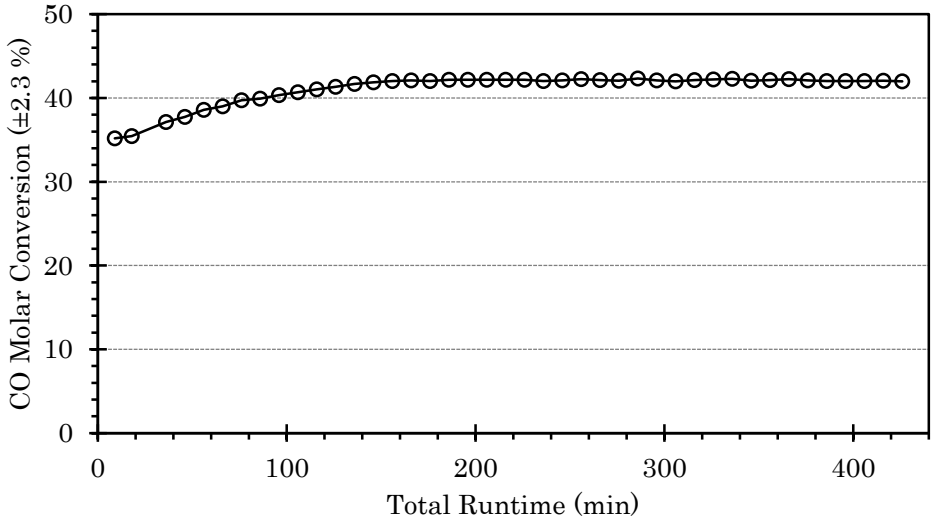

Figure 10.15: CO conversion during Fischer-Tropsch synthesis using a three plate stack of 0.3 mm microchannels coated by solution combustion synthesis. The conversion is very steady throughout the majority of the run which shows the channels can successfully stack. The stated uncertainty for the conversion is the average uncertainty over the run.

The three plate stack with 0.3 mm channels has double the total channel volume (Table 10.4) as the single plate with 0.9 mm wide channels. Given that both systems produced a catalyst giving a CO conversion of ≈ 42%, the catalyst in the 0.9 mm wide channels must be twice as active per unit volume. Since the mass of catalyst is proportional to the volume, the catalyst is also twice as active per unit mass of cobalt in the 0.9 mm channels. The difference could be the adjustment in surface area per unit volume which is 1.5 times higher for a 0.3 mm channel plate than a 0.9 mm channel plate. Therefore, a uniform coating thickness across all internal faces in the 0.9 mm channels will be 1.5 times thicker than the equivalent in the 0.3mm channels.

Table 10.4: Internal surface areas and total channel volumes of microchannel plate reactors. The increase in channel width decreases the surface area (SA) per unit channel volume (V) ratio which may explain the difference in activity.

REACTOR	SURFACE AREA (mm^2)	CHANNEL VOLUME (mm^3)	SA/V RATIO (mm^{-1})
Single plate of 0.3 mm microchannels	2280	171.0	13.33
Three plate stack of 0.3 mm microchannels	6840	513.0	13.33
Single plate of 0.9 mm microchannels	2280	256.5	8.89

From all of the runs conducted with the microchannel reactor, several important properties of the successful design for scale-up were able to be determined. Firstly, wider channels were shown to not only retain the original reaction activity demonstrated by Penniall but to actually improve it. The CO conversion was raised to over 40±2.4% at a productivity of 3.9±1.3 $g(C_{2+})\cdot g(catalyst)^{-1}\cdot h^{-1}$ compared to the up to 35% at 2.5 $g(C_{2+})\cdot g(catalyst)^{-1}\cdot h^{-1}$ obtained by Penniall [3]. This productivity is comparable to the 3.0-4.2 $g(C_{2+})\cdot g(catalyst)^{-1}\cdot h^{-1}$ recorded by Cao et al. [26] using a 150 μm powdered catalyst in a microchannel packed bed at around 5x the flowrate of synthesis gas. Secondly, the ability to stack layers without compromising the reactor performance was confirmed using three stacked 0.3 mm microchannel plates. A CO conversion of 42±2.3% and catalyst productivity of 4.9±1.7 $g(C_{2+})\cdot g(catalyst)^{-1}\cdot h^{-1}$ were attained which exceeds the performance of both Penniall's single layer [3] and the 0.9 mm channels. This places the development well for reaching a more desirable conversion of 80-90% when the channels have been lengthened. This result is made more impressive when it is considered that most industrial Fischer-Tropsch reactors run with a recycle loop creating a multiple pass system so the single pass conversion is ≈ 50% at full scale [34]. By increasing the reactor channel length and in turn the number of reaction sites this should be able to be raised to 70+% similar to what is achieved by Velocys microchannel reactors [34].

10.4. Post-Run Product Analysis

The runs utilising the solution combustion synthesis catalyst in 0.9 mm microchannels were successful enough to create a sufficient quantity of products for post run analysis. This enabled the collected liquid product to be analysed using GC to determine the product distribution and in turn the selectivity parameter, α. Once α is known then the overall product distribution can be identified using the Anderson-Schulz-Flory (ASF) distribution (Equation 10.1), where n represents the number of carbon atoms in the chain and W_n represents the mass fraction of product with chains of length 'n'.

E 10.1. $$\frac{W_n}{n} = (\alpha - 1)^2 \alpha^{(n-1)}$$ ASF Distribution

Despite the high CO conversion of over 40% and high productivity 3.9 $g(C_{2+})\cdot g(catalyst)^{-1}\cdot h^{-1}$ the volume of condensed product collected from the collection vial was small. This is due to several criteria, specifically the small reactant throughput and short run duration of only 50-60 SCCM and 6-7 hours respectively. The contents of the collection vial were split between two phases with a small amount of particles, most likely entrained catalyst fragments, also present. After centrifugation and extraction the samples for GC analysis were prepared, along with the calibration standards (Section 8.3.4 and Appendix C).

The GC analysis of the samples indicated the presence of 13 chain lengths from C_6 to C_{22} in the product, with some of the chain lengths missing. This could be a result of catalyst selectivity in the growth process or simply a loss of that molecule from the sample during extraction. The presence of the peaks through the C_5-C_8 range were entirely or partially obscured by the large peak for the C_6 (hexane) carrier however enough peaks remained in the C_9-C_{20} range that the ASF curve could be fitted to the data (Figures 10.16 and 10.17). Peaks for C_{12}, C_{14} and C_{16} appear split on the tail side while peaks for C_{13}, C_{15} and C_{17} were absent. These effects are most likely due to overlapping peaks, the absent molecules not being extracted or the presence of molecules other than the dominant linear alkanes including α-alkenes, branched alkanes and oxygenates which can all be produced by the Fischer-Tropsch synthesis.

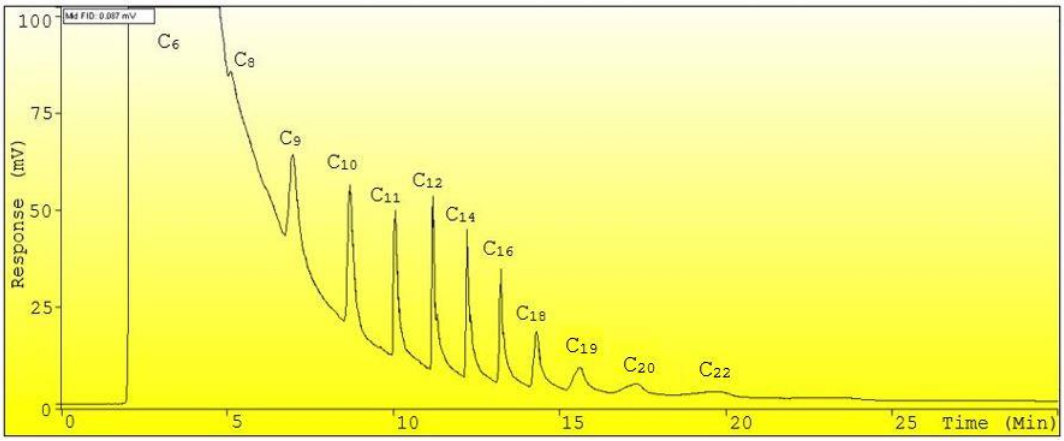

Figure 10.16: Detector response plot obtained from a liquid product GC analysis run with identified peaks labelled. Broadening could be caused by alkene presence while split peaks are likely to be poorly separated adjacent length chains, particularly on C_{12}, C_{14} and C_{16}. The obstruction effect of the carrier solvent (C_6) on C_8 is quite pronounced with the C_8 peak barely reaching above the C_6 tail.

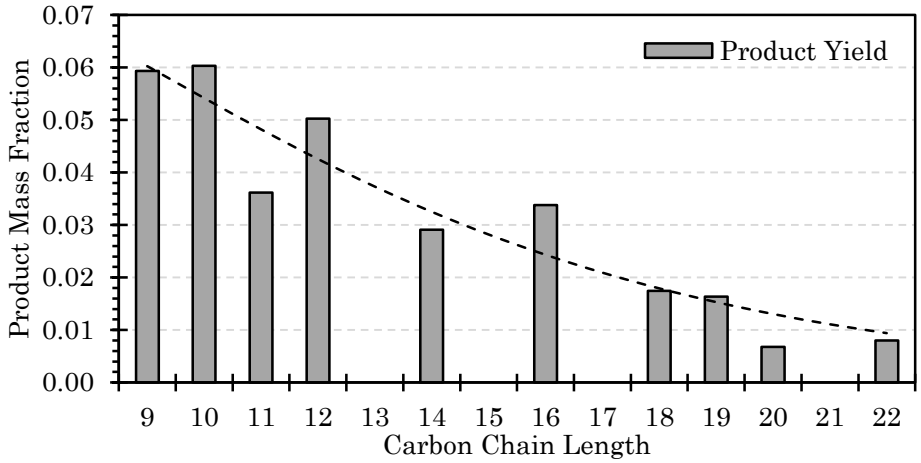

Figure 10.17: Fitted ASF product distribution with $\alpha = 0.795$ compared to the data from the liquid product analysis. The curve fits the data well except for C_{11} and C_{16} although the latter in particular may be influenced by the adjacent peaks or lack thereof.

The obtained ASF α value of 0.795 compares well to the α value of 0.78 obtained by Penniall [3] however it is lower than the 0.94-0.95 of commercial catalysts [22]. It is also lower than the 0.89-0.92 which Velocys reports for their catalyst which is prepared by a similar combustion synthesis method [34, 53]. In the model case where the entire distribution follows the ASF curve, over 67% of the product is in the C_5-C_{20} range which is ideal for the target use as a liquid fuel. This distribution gives a C_{5+} selectivity of 73%, which is higher than the Sasol/Petro SA HTFT reactors (50-68%) [9, 23] and comparable to Myrstad et al.'s $Co/Re/Al_2O_3$ coated microchannels (80%) [46] but lower than the Sasol/Shell LTFT reactors (78-95%) [9, 18, 19] and the Velocys microchannel reactors (85-90%) [49]. The selectivity of the catalyst based on the ASF distribution can be summarised by Table 10.5 which highlights the ranges for different product uses. In general, this performance supports the use of this catalyst and reactor design moving forward in the scale-up process.

Table 10.5: Product distribution characteristics using the ASF distribution for the solution combustion synthesis catalyst based on its performance in 0.9 mm wide microchannels. This is indicative only since a real system is likely to produce a higher fraction of C_1 and C_2 than what is predicted.

PRODUCT	RANGE	WEIGHT FRACTION
Fuel Gas	$C_1 - C_4$	0.273
LPG	$C_3 - C_4$	0.164
Liquids	$C_5 - C_{12}$	0.506
Liquids and Soft Waxes	$C_5 - C_{20}$	0.675
C_{5+} Hydrocarbons	$C_5 +$	0.727

A more accurate product distribution fit could be obtained by extending the analytical range using one or more of the following modifications to the analysis method:

- Utilise a smaller, more volatile solvent such as dichloromethane for the GC-FID analysis so that the compounds through the C_6-C_{10} range are not obscured by the solvent elution peak
- Adjust the method and calibration data used in the on-line GC analysis so that compounds in the C_3-C_5 range can be detected during the run in addition to the C_1-C_2 molecules.
- Change the detection type used with the GC system to one which allows more information to be gathered from the analysis. For example the use of GC-MS would show the presence of alkenes as separate peaks from alkanes and could differentiate a solvent from the FT product.

Further evidence of the productivity of this system could be seen when the channels were opened after the conclusion of the run. Many of the channels contained large depositions of waxy solid which could be identified by their cream/pale yellow colour against the dark grey/silver colour of the catalyst particles and the channels (Figures 10.18 and 10.19). Some areas of the channel seemed to have lost their catalyst coating and the shiny aluminium foil is visible (Figure 10.19). This may be due to: catalyst becoming dislodged during disassembly, catalyst entrainment and/or bubbling during coating.

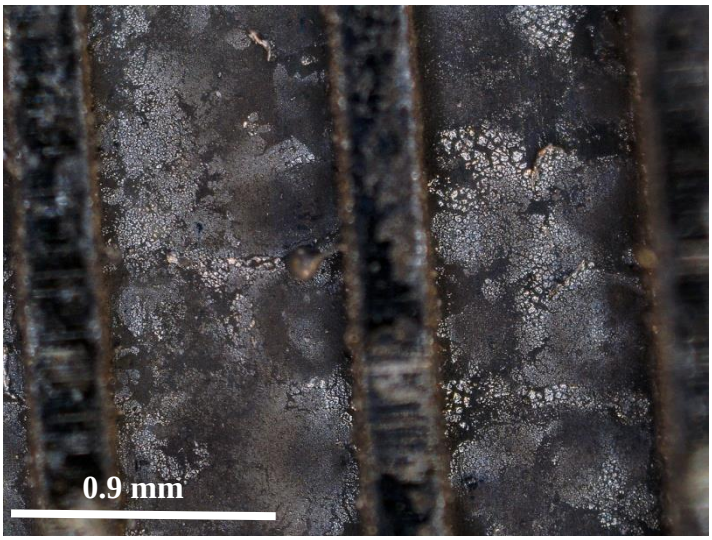

Figure 10.18: Close up photo of two 0.9 mm microchannels after the Fischer-Tropsch synthesis run showing the wax (white/yellow) and catalyst (grey/black) depositions. While the image is focussed on the depositions on the foil gasket at the base of the channel, the depositions on the channel walls can also be seen with wax deposits giving them a brown colour.

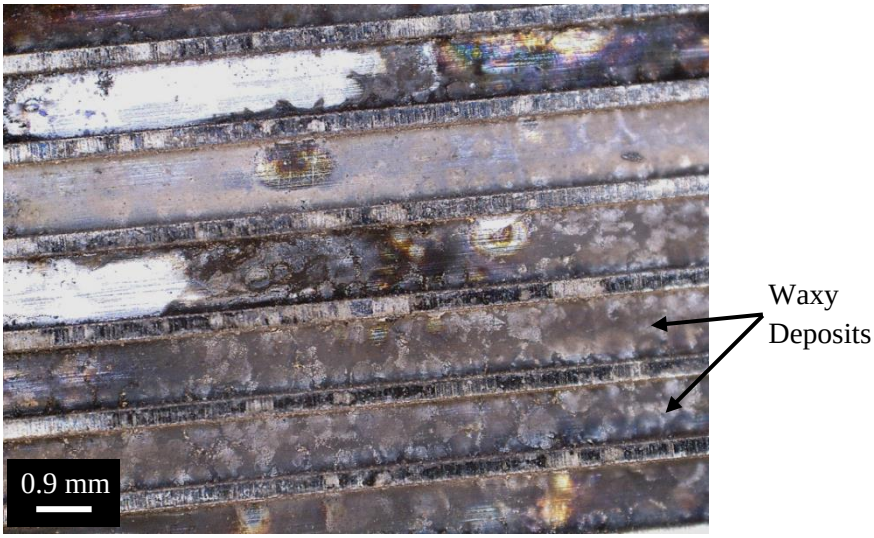

Figure 10.19: Close up photo of the deposition in the 0.9 mm microchannels after Fischer-Tropsch synthesis showing the quantity of wax depositions in the channels. A few bubble like spots can be seen to the left of the image indicating some room for improvement in the coating. The extensive waxy depositions visible in the channels elsewhere show the productivity of the sample.

11.0. Modelling the Reactor System

To gain an understanding of the reactor size required when scaled up a mathematical model of the system was constructed. This model utilised a kinetic rate expression in the form used by Yates and Satterfield [cite] (Equation 7.1) to determine the reactivity. The constants 'a' and 'b' in the equation were adjusted to obtain a fit to the experimental data from the 0.9 mm wide channels with combustion synthesis coating giving Equation 11.1. The new constants reflect the rate on a per volume basis suitable for a set of channels behaving as a plug-flow reactors (PFRs).

CO reaction rate $$-r_{CO} = \frac{3098 P_{CO} P_{H_2}}{(1+21.86 P_{CO})^2} \quad (11.1)$$

Combining this with Equations 11.2-11.4, we can calculate the expressions for the consumption of hydrogen and generation of water and FT product. The 'FT product' here is a lumped product based around forming chains of the average length 'n' which is determined from the ASF distribution. The experimental data from the 0.9 mm channels with combustion synthesis coating had an ASF α value of 0.795 (Section 10.4) which gives 'n' = 8.75. Utilising this along with the experimental observation that ≈ 20% of the CO is converted to methane gave the consumption ratio 'A' = 2.29 for a system producing linear alkanes. Constant calculations can be found in Appendix #.

H_2 reaction rate $$-r_{H_2} = -r_{CO} \times 2.29 \quad (11.2)$$

FT Product formation rate $$r_P = -\frac{-r_{CO}}{8.75} \quad (11.3)$$

H_2O formation rate $$r_{H_2O} = -(-r_{CO}) \quad (11.4)$$

There were four differential equations (Equations 11.5-11.8) to solve in parallel as the molar material balances for each of the four species in the reaction. Numerical integration was performed using an iterative Matlab function (Appendix #) solving for the species flows in each differential element along the reactor length treating the microchannel system as a plug-flow reactor. The CO flow out of each element could then be used to calculate the conversion up to that length. After calculating the new species flows, the partial pressures and element inlet flows are cycled to the input side for the next element. This calculation loop was set to cycle until a specified target conversion was reached.

CO flow $$\frac{dF_{CO}}{dV} = -r_{CO\,(i)} \quad (11.5)$$

H_2 flow $$\frac{dF_{H_2}}{dV} = -r_{H_2\,(i)} \quad (11.6)$$

FT Product flow $$\frac{dF_{Prod}}{dV} = r_{Prod\,(i)} \quad (11.7)$$

H_2O flow $$\frac{dF_{H_2O}}{dV} = r_{H_2O\,(i)} \quad (11.8)$$

To ensure the model was operating correctly the species partial pressures and reactant consumption rates were plotted along the length of the reactor in addition to the primary conversion profile plot. If the system was correctly operating the partial pressures of reactants and products would decrease and increase respectively and the rate of reaction should decline at an increasing rate (Figures 11.1 and 11.2). The conversion profile along the length of the channels (Figure 11.3) could then be accepted. Despite its linear appearance, the change in length per percent conversion added was increasing however this is not particularly apparent with this rate expression.

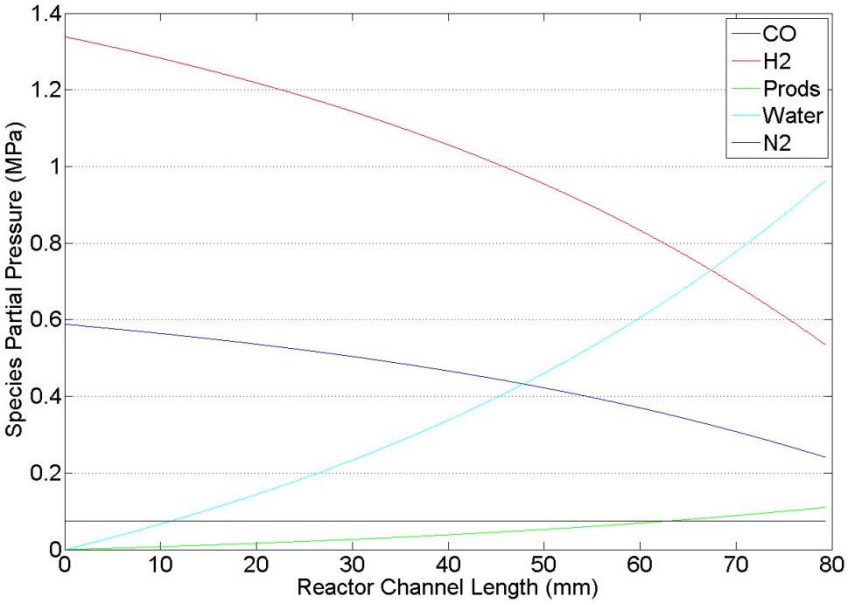

Figure 11.1: Species partial pressures in the model Fischer-Tropsch reactor over the length required to achieve 80% CO conversion. Prods represents the lumped product with average chain length n = 8.75.

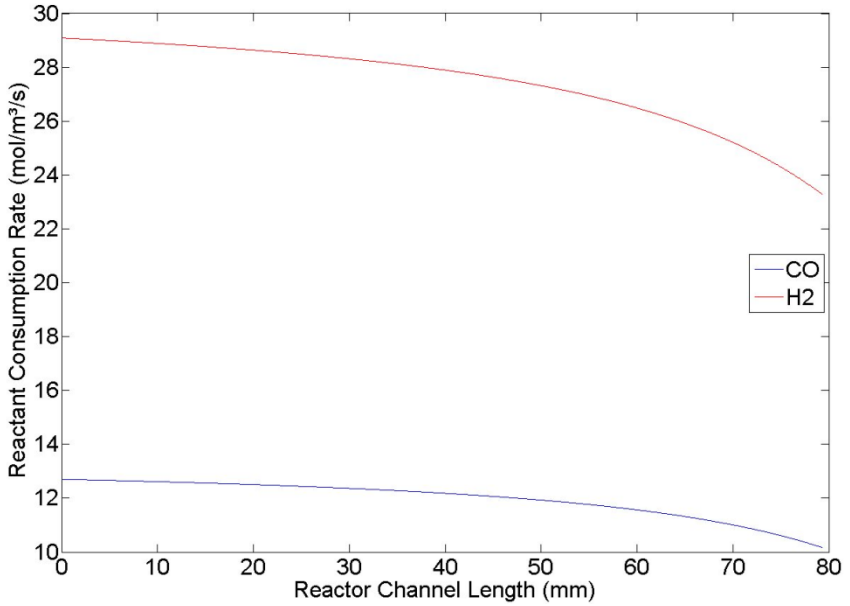

Figure 11.2: Rates of reaction for CO and H_2 in the model Fischer-Tropsch system with X_{CO} = 80%.

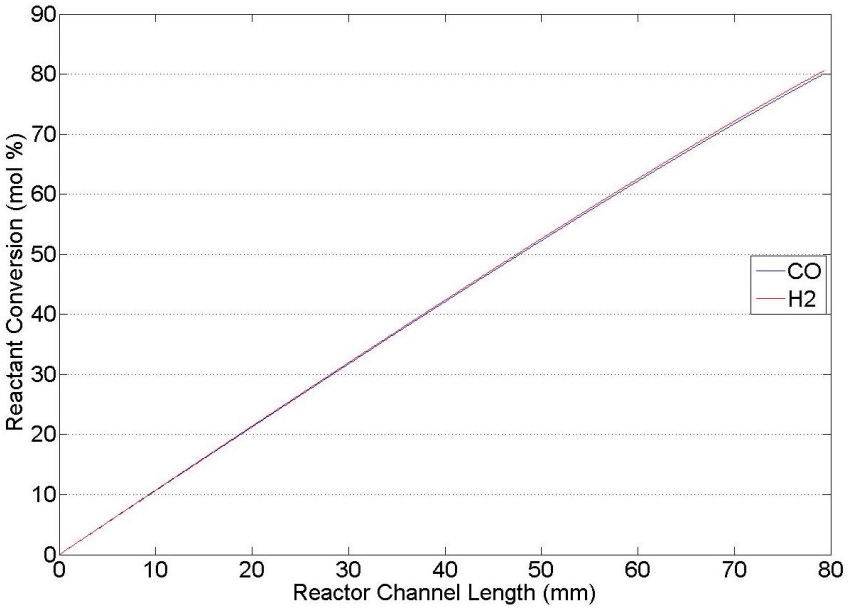

Figure 11.3: Conversion profile of the modelled Fischer-Tropsch reactor system for length up to that required to achieve a CO conversion of 80%.

It is important to recognise that the synthesis gas feed flow rate is influential in the performance of the system in the model. The above Figures 11.1-11.3 were all created with the system running at the average flowrate observed during the experiment of 39.95 SCCM. Increasing this to a higher value more suited to the larger capacity of the widened channels of around 60 SCCM the curve becomes slightly more apparent (Figure 11.4). The length required to achieve 80% conversion is also increased from 79.3 mm to 119.1 mm.

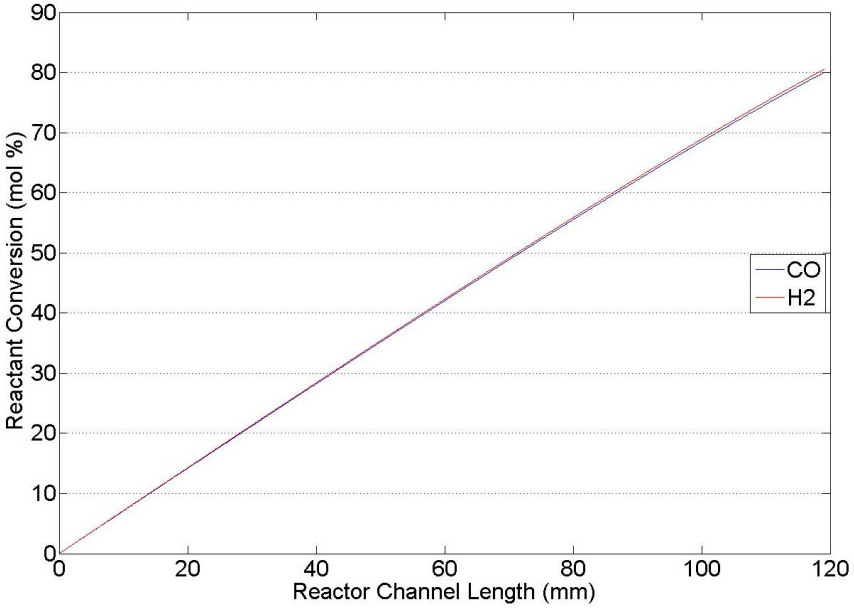

Figure 11.4: Model conversion profile with the feed flow rate raised from 39.95 SCCM to 60 SCCM.

Applying this information, a good test length for channels to examine the system running at a higher conversion is 100 mm as it can theoretically achieve a conversion near 80% across the range of flow rates expected to occur in the system. If additional plates are layered in this flow can be scaled proportionally assuming that the catalyst behaves identically in each layer however this will require experimental confirmation.

12.0. Recommendations and Potential Future Studies

Following the results of this study, several recommendations are made for future work developing this system. The most important of these is the recommended design for the next stage of experimental testing which has been designed based on the findings of the work completed in Sections 8-11. In addition there are a number of improvements which can be made to improve aspects of the analysis and modelling in order to fully optimise the system and connect it to a fresh synthesis gas feed.

12.1. Recommended Scale-Up Design

From the findings of the experimental section it was concluded that a reactor system with wider channels did not lose activity for the Fischer-Tropsch synthesis and the productivity was significantly increased without increasing the reactor size. The conversion however remained fairly low and therefore getting an accurate profile for conversion with reactor length is one of the objectives with the new design. Utilising the modelling work done in Section 11, the size of this new system was predicted however it made several assumptions which may not hold true in the physical system so experimental testing is required to confirm the validity of the model performance.

Combining the model predictions and experimental results from testing the widened channels, a new reactor channel plate (Figure 12.1) was designed. The goal of this new design was to combine the high activity demonstrated by the solution combustion synthesis catalyst in the 0.9 mm wide channels with a channel length extended to 100 mm to increase the CO conversion to hydrocarbon products. Model data showed that this combination could achieve conversions in the 70-85% range depending on the stability of the feed flowrate to the system. Applying a better control to the reactor inlet flow (likely using a mass flow controller) would allow the system to be manipulated to maintain constant conversion and stable operation by adapting the feed flow. This becomes necessary when operating at high conversions as the modelling showed exceeding 80% conversion led to a rapid decline in reaction rate.

After consulting with workshop manufacturing technicians during the design phase it was decided that it would be useful to increase the width of the dividing bars between channels in order to help prevent breakages during reactor assembly and operation. Therefore these were widened from 0.3 mm in the small scale plate to 0.5 mm in the larger scale plate in Figure 12.1. The design of the openings in the gas feed distribution plates was maintained from the design used at the smaller scale by Penniall [3] (Figure 8.08a) as this was shown by Commenge et al. [31] to be the optimal design for uniform flow in a microchannel reactor. The cost of these plates has been higher than expected costing about $180 NZ excluding GST per pair (distribution and channels) due to difficulty with the EDM cutting. Details are given in Appendix D, alongside those for the original size plates.

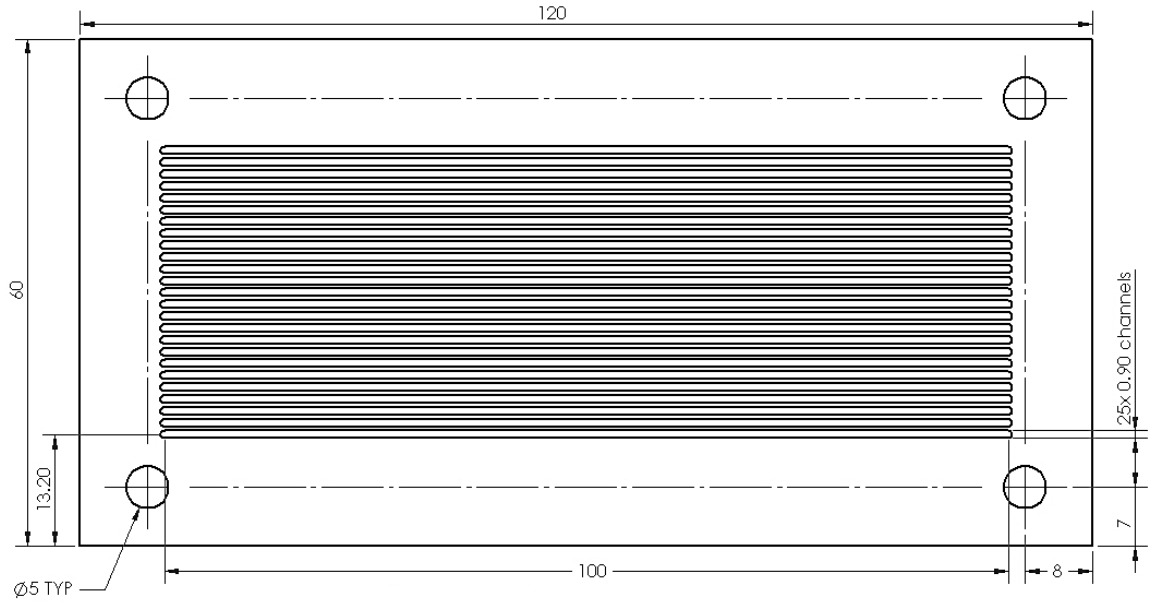

Figure 12.1: New microchannel plate design for recommended scaled up reactor system. The 25 channels are 0.9 mm wide x 100 mm long and are separated by 0.5 mm wide dividers. Multiple layers of plate can be stacked to increase the throughput after initial testing.

Experimental testing and supporting computational fluid dynamics (CFD) modelling can be used to determine the optimum number of layers to stack in a reactor core based on the gas flow and heat transfer. Since the small dimensions make heat transfer a strength of microchannel designs, the number of layers is likely to be determined by the gas flow profile between layers. Any additional capacity beyond this point will require operating parallel reactor cores. Since all of the cores will behave identically this should be a simple procedure.

12.2. Model Modifications and Enhancement

It is recommended that several modifications and enhancements are made to the model of the system. Firstly, the kinetic rate law (Equation 12.1) should be properly fitted to the new design utilising a number of reaction runs at multiple pressures (Table 12.1) to establish accurate values for the constants ‘a’ and ‘b’. This would enable the model to accurately predict the productivity of the system with the new catalyst so that the ideal flow rate, channel length and operating conversion combination can be determined.

Kinetic Rate $$-r_{CO} = \frac{aP_{CO}P_{H_2}}{(1+bP_{CO})^2} \quad (12.1)$$

Table 12.1: Suggested range of pressures and to run the system at to obtain a fit for the constants in Equation 12.1. Other conditions (gas flow, temperature, gas composition) should be kept constant.

RUN	PRESSURE (bar)
1	5
2	10
3	15
4	20
5	25

To further the model's usefulness, adapting it to include calculations for the heat transfer in the system would be very helpful for determining the design of the heat transfer system. By utilising the ASF plot of the products to determine the average chain length, the average amount of heat generated by the reaction can be predicted. Combining this with the conductive, convective and radiative heat transfers through and from the reactor will give an indication of the external heat transfer required.

From a scale-up perspective it could be useful to create a numerical or CFD simulation of the reactor layers in order to examine the flow distribution between layers when multiple layers are used. Including elements of the heat transfer and conversion models would create a comprehensive system model. This could give some valuable insight into the operation of a microchannel Fischer-Tropsch system and its benefits over traditional reactor designs such as tubular fixed beds and fluidised beds.

12.3. 3D Printing the Reactor

The wire-cutting (EDM) technique used for manufacturing the microchannels is quite expensive with a pair of (feed distribution and reaction channel) plates costing ≈ $180 NZ excluding GST. It is thought that 3D printing a reactor core as a single part rather than cutting multiple plates could reduce the cost and also present other advantages over cutting the channels. Amongst these is the ability to have a single part rather than many which would reduce the number of sealing gaskets required and in turn the number of potential leak locations. A single part would require at most gaskets on 2-4 faces of the core unit independent of the number of channel layers included. The exact arrangement may vary depending on the capability of the technology and how the block can be made.

Rapid Advanced Manufacturing, based in Tauranga, have the machinery to produce components in build sizes up to 245 mm x 245 mm x 280 mm and 280 mm x 280 mm x 350 mm from Inconel 718 (a Ni, Cr, Fe alloy) and stainless steel or titanium alloy respectively. Their selective laser melting (SLM) technology allows manufacturing detail as fine as 30-60 μm thick [114] which would enable the dimensions of the reactor to be made very exact. A cost analysis of a reactor core made using this method is highly recommended, due to the higher than expected cost of EDM cutting the larger sized channel plates (Appendix D).

A variation to inspect if a 3D printed design is pursued is to investigate the effects of channel shape on the catalyst formations. Any of the experiments conducted thus far have only used channels with square or rectangular cross-sections with the best depositions seen near the corners of the cross-sectional shape. Therefore such an investigation could consider the depositions formed in channels with a range of cross-sectional shapes such as circles, triangles, hexagons, octagons and even stars (Figure 12.2). This could determine an optimum channel shape and aspect ratio for microchannels although it would be wise to keep the shape from becoming too complex as it needs to be easily manufactured.

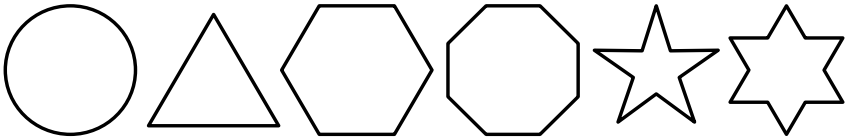

Figure 12.2: Potential channel cross-sectional shapes which could be examined in a 3D printed reactor.

12.4. Extended Product Analysis

To better understand the product produced by the microchannel Fischer-Tropsch system it is recommended that a more comprehensive product analysis is completed. To achieve this it is recommended that an extended length run of around 200 hours is completed to ensure that a sufficient volume of condensable product is to allow more analysis and to ensure all compounds are present. During this run the cooling temperature applied to the product collection chamber should also be lowered slightly from 0 °C to ≈ -10 °C. This will ensure that the inner chamber which runs approximately 8 °C warmer is at or below 0 °C to fully condense the aqueous phase and improve the collection of the C_5-C_8 range hydrocarbons. The reactor should also be flushed with solvent to remove condensed wax from inside the channels so the product analysis is fully representative. To make the subsequent analysis more complete three modifications are recommended: increase the range of the on-line analysis, adjust the analysis of the non-polar phase and add analysis of the aqueous phase.

At present the on-line micro-GC only detects H_2, CO, CO_2, N_2, O_2, CH_4, C_2H_4 and C_2H_6 which are the only products produced in large enough quantities at low conversion. At a higher conversion the levels of CO and H_2 will be substantially lower and more hydrocarbon product will be able to be detected. Given the cooled knockout separation used to collect the heavier products will leave only low boiling point species in the gas the range cannot be extended much however C_3 (normal BP -42 to -48 °C) and C_4 (normal BP -1 to -6 °C) species could be included. This could still provide valuable information on the product as the alkene/alkane ratio of the product will be able to be seen from the amount of ethene, propene and butene produced relative to ethane, propane and butane respectively. A secondary use is to determine a secondary ASF α value for the two-α model which is sometimes used to describe the short and long chain Fischer-Tropsch products separately [cite usage].

The current analysis of the non-polar phase (Section 8.3.4) is completed using n-hexane as the solvent and flame-ionisation detection (FID). This is good for identifying the relative amounts of C_9-C_{20} hydrocarbons in the non-polar phase in order to fit an ASF α value however it has a few limitations. Firstly, it is unable to detect compounds covered in the hexane peak (C_6-C_8) as their existence is completely obscured by the solvent peak. This could be remedied by applying an alternate solvent such as dichloromethane (CH_2Cl_2) which will separate from the hydrocarbon chains in the chromatographic columns due to its smaller size and lower boiling point than all C_{6+} hydrocarbons. C_5 hydrocarbons may still be difficult to detect although the C_6-C_{10} range will show the required detail from the heavier end and the on-line analysis can show the lighter side. In addition to adjusting the solvent, utilising a different detection mechanism such as mass spectroscopy (MS) could provide a better insight to the products present than FID. The peaks of alkanes and alkenes will be different and the distinction of a full product spectrum may be possible.

The final recommended adjustment to the product analysis is the addition of an analysis of the aqueous phase products. The Fischer-Tropsch synthesis can produce alcohols, ketones, aldehydes and carboxylic acids by the CO insertion mechanism and these would mostly mix into the aqueous product phase. Analysis of these could provide additional detail into the properties of the unique solution combustion synthesis catalyst which is used.

12.5. Catalyst Analysis

During these experiments two catalysts were produced for which not a large amount of detail is known: the electrochemical deposition catalyst and the solution combustion synthesis catalyst. Both of these catalysts were able to form fine microstructures and provide activity (albeit brief for the electrochemical deposition catalyst) for the Fischer-Tropsch synthesis. Therefore further investigation into the structure and composition of these catalysts is warranted. In the case of the electrochemical deposition catalyst it could also reveal the reasoning for the sudden activity decline of the catalyst under the reaction conditions, therefore enabling it to be stabilised and utilised as a Fischer-Tropsch catalyst. Experimental analysis techniques which could be used to determine the properties include: x-ray diffraction (XRD), energy-dispersive x-ray spectroscopy (EDS/EDX), Brunauer-Emmett-Teller (BET) adsorption analysis and temperature programmed reduction (TPR).

13.0. Conclusions

Solution combustion synthesis (SCS) was found to be the best catalyst formation and deposition technique. Scanning electron microscopy (SEM) revealed this method to be superior to the washcoating techniques did as it formed a catalyst with a finer more disperse structure and little agglomeration. It was found to be superior to the electrochemical deposition method as the catalyst maintained its activity for the Fischer-Tropsch synthesis reaction for a substantially longer time period.

Part of the solution to the catalyst deposition was also found to be matching it to the correct reactor design. The initial design trialled which used a support structure, such as corrugated mesh, inside a large channel was found to be unhelpful for forming microstructured catalysts. The large channel volume allowed the particles to easily agglomerate and lumpy inactive catalysts were formed using in-situ methods. While manufacturing this design would be much cheaper and easier its lack of compatibility with active catalysts makes it a poor choice. In contrast the relatively difficult and expensive to manufacture microchannel plates provided an ideal channel dimension for optimum catalyst formation.

Combining these two successes the channel dimensions of the microchannels were able to be increased in an attempt to improve manufacturability, decrease cost and improve the throughput capacity. While the throughput capacity has successfully been increased, the production of the plates still has difficulties and the cost was higher than expected. Wider channels may open up possibilities other than EDM cutting which could improve the cost element. A possible technology to consider here is 3D printing.

Product analysis of the combined system indicated that the solution combustion synthesis catalyst was highly active and had a selectivity well suited to liquid fuels. The conversion of CO was able to be increased to over 40% which was stable over the entirety of the short runs completed and modelling indicates that around 80% is possible in the larger design. Liquid product analysis showed good production of hydrocarbons in the C_9-C_{20} range, a positive ASF α value of 0.795 and a C_{5+} selectivity of 73%.

Overall, the combination of solution combustion synthesis catalyst and 0.9 mm wide microchannels proved successful in an attempt to increase the capacity of the microchannel Fischer-Tropsch reactor. Further studies are still required to achieve the final design of a 10 $SL \cdot min^{-1}$ however this combination should be able to provide the physical capacity. The remaining work will pertain to the cooling layers and accompanying operations.

14.0. References

1. Saw, W., et al., *Production of hydrogen-rich syngas from steam gasification of blend of biosolids and wood using a dual fluidised bed gasifier.* Fuel, 2012. **93**: p. 473-478.
2. Saw, W.L. and S. Pang, *Co-gasification of blended lignite and wood pellets in a 100 kW dual fluidised bed steam gasifier: The influence of lignite ratio on producer gas composition and tar content.* Fuel, 2013. **112**: p. 117-124.
3. Penniall, C., *Fischer-Tropsch Based Biomass to Liquid Fuel Plants in the New Zealand Wood Processing Industry Based on Microchannel Reactor Technology*, in *Chemical and Process Engineering*2013, University of Canterbury: Christchurch, New Zealand. p. 265.
4. Steynberg, A.P., *Introduction to Fischer-Tropsch Technology*, in *Fischer-Tropsch Technology*, A.P. Steynberg and M.E. Dry, Editors. 2004, Elsevier B.V.: Amsterdam, The Netherlands. p. 1-63.
5. Davis, B., *Fischer–Tropsch synthesis: Overview of reactor development and future potentialities.* Topics in Catalysis, 2005. **32**(3-4): p. 143-168.
6. Dry, M.E., *The Fischer–Tropsch process: 1950–2000.* Catalysis Today, 2002. **71**(3–4): p. 227-241.
7. Schulz, H., *Short history and present trends of Fischer–Tropsch synthesis.* Applied Catalysis A: General, 1999. **186**(1–2): p. 3-12.
8. Anderson, R.B., H. Kolbel, and M. Ralek, *The Fischer-Tropsch Synthesis*. 1984, Orlando: Academic Press.
9. de Klerk, A., *Fischer-Tropsch Refining*. 2011, Weinheim: Wiley-VCH.
10. Aasberg-Petersen, K., et al., *Synthesis Gas Production for FT Synthesis*, in *Fischer-Tropsch Technology*, A.P. Steynberg and M.E. Dry, Editors. 2004, Elsevier B.V.: Amsterdam, The Netherlands. p. 258-405.
11. Higman, C. and M. van der Burgt, *Gasification*. Vol. 2nd. 2008, Amsterdam;Boston;: Gulf Professional Pub./Elsevier Science.
12. Linc Energy. *Clean Energy in Australia*. 2012 [cited 2016 30/3/]; Available from: http://www.lincenergy.com/clean_energy_australia.php.
13. Gaur, S. and T.B. Reed, *Thermal Data for Natural and Synthetic Fuels*. 1998: Taylor & Francis.
14. Rauch, R., *Gasification of biomass - Biomass CHP Güssing*, 2008: Vienna University of Technology.
15. Jonsson, P. and Elmia AB. *Gasification gives lower emissions, less dust and a broader feedstock*. 2010 [cited 2016 30/3/]; Available from: http://www.mynewsdesk.com/se/elmia/pressreleases/foergasning-ger-laegre-utslaepp-mindre-stoft-och-bredare-braenslebas-nyhet-paa-elmia-recycling-to-energy-2010-381629.
16. Erdalen, C. and Göteborg Energi. *Göteborg Energi´s biogas plant GoBiGas is now fully operational*. 2009 [cited 2016 30/3/]; Available from: http://gobigas.goteborgenergi.se/English_version/News/Goteborg_Energi_s_biogas_plant_GoBiGas_is_now_fully_operational.
17. Steynberg, A.P., et al., *Fischer-Tropsch Reactors*, in *Fischer-Tropsch Technology*, A.P. Steynberg and M.E. Dry, Editors. 2004, Elsevier B.V.: Amsterdam, The Netherlands. p. 64-195.
18. Dry, M.E. and A.P. Steynberg, *Commercial FT Process Application*, in *Fischer-Tropsch Technology*, A.P. Steynberg and M.E. Dry, Editors. 2004, Elsevier B.V.: Amsterdam, The Netherlands. p. 406-481.
19. Dry, M.E., *The Fischer-Tropsch Synthesis*, in *Catalysis: science and technology*, J.R. Anderson and M. Boudart, Editors. 1981, Springer-Verlag: Berlin.
20. Moodley, D.J., et al., *The Formation and Influence of Carbon on Cobalt Based Fischer-Tropsch Synthesis Catalysts: An Integrated Review*, in *Advances in Fischer-Tropsch Synthesis, Catalysts and Catalysis*, B.H. Davis and M.L. Occelli, Editors. 2010, CRC Press.
21. Espinoza, R.L., et al., *Low temperature Fischer–Tropsch synthesis from a Sasol perspective.* Applied Catalysis A: General, 1999. **186**(1–2): p. 13-26.

22. Jager, B. and R. Espinoza, *Advances in low temperature Fischer-Tropsch synthesis.* Catalysis Today, 1995. **23**(1): p. 17-28.
23. Steynberg, A.P., et al., *High temperature Fischer–Tropsch synthesis in commercial practice.* Applied Catalysis A: General, 1999. **186**(1–2): p. 41-54.
24. Dry, M.E., *Chemical Concepts used for Engineering Purposes*, in *Fischer-Tropsch Technology*, A.P. Steynberg and M.E. Dry, Editors. 2004, Elsevier B.V.: Amsterdam, The Netherlands. p. 196-257.
25. Gumuslu, G. and A.K. Avci, *Parametric analysis of Fischer-tropsch synthesis in a catalytic microchannel reactor.* AIChE Journal, 2012. **58**(1): p. 227-235.
26. Cao, C., et al., *Intensified Fischer–Tropsch synthesis process with microchannel catalytic reactors.* Catalysis Today, 2009. **140**(3–4): p. 149-156.
27. Cao, C., et al., *Catalyst screening and kinetic studies using microchannel reactors.* Catalysis Today, 2007. **125**(1–2): p. 29-33.
28. Cao, C., et al., *Kinetic studies of methanol steam reforming over Pd/ZnO catalyst using a microchannel reactor.* Applied Catalysis A: General, 2004. **262**(1): p. 19-29.
29. Visconti, C.G., et al., *Monolithic catalysts with high thermal conductivity for the Fischer–Tropsch synthesis in tubular reactors.* Chemical Engineering Journal, 2011. **171**(3): p. 1294-1307.
30. Kshetrimayum, K.S., et al., *CFD Simulation of Microchannel Reactor Block for Fischer–Tropsch Synthesis: Effect of Coolant Type and Wall Boiling Condition on Reactor Temperature.* Industrial & Engineering Chemistry Research, 2016. **55**(3): p. 543-554.
31. Commenge, J.M., et al., *Optimal design for flow uniformity in microchannel reactors.* AIChE Journal, 2002. **48**(2): p. 345-358.
32. Sotowa, K.-I., S. Sugiyama, and K. Nakagawa, *Flow Uniformity in Deep Microchannel Reactor under High Throughput Conditions.* Organic Process Research & Development, 2009. **13**(5): p. 1026-1031.
33. Arzamendi, G., et al., *A CFD study on the effect of the characteristic dimension of catalytic wall microreactors.* AIChE Journal, 2012. **58**(9): p. 2785-2797.
34. Atkinson, D. and J. McDaniel, *Microchannel reactors in fuel production*, in *Petrochemical Technology Quarterly (PTQ)*2010: online.
35. Deshmukh, S.R., et al., *Scale-Up of Microchannel Reactors For Fischer−Tropsch Synthesis.* Industrial & Engineering Chemistry Research, 2010. **49**(21): p. 10883-10888.
36. LeViness, S., et al., *Velocys Fischer–Tropsch Synthesis Technology—New Advances on State-of-the-Art.* Topics in Catalysis, 2014. **57**(6-9): p. 518-525.
37. Hilmen, A.M., et al., *Fischer–Tropsch synthesis on monolithic catalysts of different materials.* Catalysis Today, 2001. **69**(1–4): p. 227-232.
38. Holmen, A., et al., *Monolithic, microchannel and carbon nanofibers/carbon felt reactors for syngas conversion by Fischer-Tropsch synthesis.* Catalysis Today, 2013. **216**: p. 150-157.
39. Mehta, S., et al., *Comparative Studies of Silica-Encapsulated Iron, Cobalt, and Ruthenium Nanocatalysts for Fischer–Tropsch Synthesis in Silicon-Microchannel Microreactors.* Industrial & Engineering Chemistry Research, 2014. **53**(42): p. 16245-16253.
40. Visconti, C.G., et al., *An experimental investigation of Fischer–Tropsch synthesis over washcoated metallic structured supports.* Applied Catalysis A: General, 2009. **370**(1–2): p. 93-101.
41. Nijhuis, T.A., et al., *Preparation of monolithic catalysts.* Catalysis Reviews, 2001. **43**(4): p. 345-380.
42. Robota, H., et al., *High Activity and Selective Fischer–Tropsch Catalysts for Use in a Microchannel Reactor.* Catalysis Surveys from Asia, 2014. **18**(4): p. 177-182.
43. Almeida, L.C., et al., *Fischer–Tropsch synthesis in microchannels.* Chemical Engineering Journal, 2011. **167**(2–3): p. 536-544.
44. Tagawa, T., et al., *Evaluation of catalyst prepared in microchannel with in situ FT-IR microscopy.* Chemical Engineering Journal, 2011. **167**(2–3): p. 427-430.
45. de Deugd, R.M., F. Kapteijn, and J.A. Moulijn, *Using monolithic catalysts for highly selective Fischer–Tropsch synthesis.* Catalysis Today, 2003. **79–80**(0): p. 495-501.

46. Myrstad, R., et al., *Fischer–Tropsch synthesis in a microstructured reactor*. Catalysis Today, 2009. **147, Supplement**(0): p. S301-S304.
47. Kapteijn, F., R.M. de Deugd, and J.A. Moulijn, *Fischer–Tropsch synthesis using monolithic catalysts.* Catalysis Today, 2005. **105**(3–4): p. 350-356.
48. Kapteijn, F., et al., *New non-traditional multiphase catalytic reactors based on monolithic structures.* Catalysis Today, 2001. **66**(2–4): p. 133-144.
49. McDaniel, J. *Velocys GTL Technology*. in *GTL Technology Forum 2014*. 2014. Houston, Texas.
50. Velocys. *Image Library*. [website page] 2016; Available from: http://www.velocys.com/media_image_library.php.
51. Liu, W., et al., *A compact and high throughput reactor of monolithic-structured catalyst bed for conversion of syngas to liquid fuels.* AIChE Journal, 2012. **58**(9): p. 2820-2829.
52. Eisberg, N., *Portuguese renewable energy investment specialist SGC Energia is to provide $5.9m in funding to Velocys, the US-based subsidiary of UK catalyst specialist Oxford Catalysts, to facilitate the demonstration and commercialisation of its Fischer-Tropsch microchannel reactor technology*, 2009, Wiley Subscription Services, Inc. p. 13.
53. Richard, L.A., et al., *Fischer-Tropsch performance correlated to catalyst structure: Trends in activity and stability for a silica-supported cobalt catalyst.* Applied Catalysis A: General, 2013. **464–465**(0): p. 200-206.
54. Litt, R.D. and W.W. Simmons, *Process and apparatus for converting natural gas to higher molecular weight hydrocarbons using microchannel process technology*, 2009, Google Patents.
55. Daly, F., L. Richard, and S. Rugmini, *Catalysts*, in *Google Patents*2012: United Kingdom.
56. Xiao, T. and Y. Qian, *Promoted carbide-based Fischer-Tropsch catalyst, method for its preparation and uses thereof. WO2008104793A2.*, in *Google Patents*2008: United Kingdom.
57. Dry, M.E., *FT Catalysts*, in *Fischer-Tropsch Technology*, A.P. Steynberg and M.E. Dry, Editors. 2004, Elsevier B.V.: Amsterdam, The Netherlands. p. 533-600.
58. Urquhart, A.J., F.J. Williams, and R.M. Lambert, *Electrochemical Promotion by Potassium of Rh-Catalysed Fischer–Tropsch Synthesis at High Pressure.* Catalysis Letters, 2005. **103**(1-2): p. 137-141.
59. London Metals Exchange. *LME Cobalt*. 2016 [cited 2016 24/03]; Available from: http://www.lme.com/metals/minor-metals/cobalt/.
60. London Metals Exchange. *LME Nickel*. 2016 [cited 2016 24/03]; Available from: http://www.lme.com/metals/non-ferrous/nickel/.
61. Stevens, C. and Quandtl. *Industrial Metals Prices and Charts*. 2016 [cited 2016 24/03]; Available from: https://www.quandl.com/collections/markets/industrial-metals.
62. Catalysts Division - BASF Corporation. *Engelhard Industrial Bullion (EIB) Prices*. 2016; Available from: https://apps.catalysts.basf.com/apps/eibprices/mp/.
63. Fischer, N., E. van Steen, and M. Claeys, *Structure sensitivity of the Fischer–Tropsch activity and selectivity on alumina supported cobalt catalysts.* Journal of Catalysis, 2013. **299**(0): p. 67-80.
64. Ali, S., N. Mohd Zabidi, and D. Subbarao, *Correlation between Fischer-Tropsch catalytic activity and composition of catalysts.* Chemistry Central Journal, 2011. **5**(1): p. 68.
65. Sie, S.T., M.M.G. Senden, and H.M.H. Van Wechem, *Conversion of natural gas to transportation fuels via the shell middle distillate synthesis process (SMDS).* Catalysis Today, 1991. **8**(3): p. 371-394.
66. Liu, L., et al., *Aqueous phase Fischer–Tropsch synthesis in a continuous flow reactor.* Catalysis Today, 2012. **183**(1): p. 136-142.
67. Williams, F. and R. Lambert, *A study of sodium promotion in Fischer–Tropsch synthesis: electrochemical control of a ruthenium model catalyst.* Catalysis Letters, 2000. **70**(1-2): p. 9-14.
68. Van Der Laan, G.P. and A.A.C.M. Beenackers, *Kinetics and Selectivity of the Fischer–Tropsch Synthesis: A Literature Review.* Catalysis Reviews, 1999. **41**(3-4): p. 255-318.
69. Enger, B.C. and A. Holmen, *Nickel and Fischer-Tropsch Synthesis.* Catalysis Reviews, 2012. **54**(4): p. 437-488.

70. Moodley, D.J., et al., *Carbon deposition as a deactivation mechanism of cobalt-based Fischer–Tropsch synthesis catalysts under realistic conditions.* Applied Catalysis A: General, 2009. **354**(1–2): p. 102-110.
71. Cronauer, D., et al., *Fischer–Tropsch Synthesis: Preconditioning Effects Upon Co-Containing Promoted and Unpromoted Catalysts.* Catalysis Letters, 2012. **142**(6): p. 698-713.
72. Chu, W., et al., *Cobalt species in promoted cobalt alumina-supported Fischer–Tropsch catalysts.* Journal of Catalysis, 2007. **252**(2): p. 215-230.
73. de la Osa, A.R., et al., *Influence of the catalytic support on the industrial Fischer–Tropsch synthetic diesel production.* Catalysis Today, 2011. **176**(1): p. 298-302.
74. Storsæter, S., et al., *Characterization of alumina-, silica-, and titania-supported cobalt Fischer–Tropsch catalysts.* Journal of Catalysis, 2005. **236**(1): p. 139-152.
75. Borg, Ø., *Role of Alumina Support in Cobalt Fischer-Tropsch Synthesis*, in *Department of Chemical Engineering, Faculty of Natural Sciences and Technology*2007, Norwegian University of Science and Technology (NTNU): Trondheim. p. 140.
76. Borg, Ø., et al., *Fischer–Tropsch synthesis: Cobalt particle size and support effects on intrinsic activity and product distribution.* Journal of Catalysis, 2008. **259**(2): p. 161-164.
77. Borg, Ø., et al., *Fischer–Tropsch synthesis over γ-alumina-supported cobalt catalysts: Effect of support variables.* Journal of Catalysis, 2007. **248**(1): p. 89-100.
78. Borg, Ø., et al., *Fischer–Tropsch synthesis over un-promoted and Re-promoted γ-Al2O3 supported cobalt catalysts with different pore sizes.* Catalysis Today, 2009. **142**(1–2): p. 70-77.
79. Tavasoli, A., et al., *Cobalt loading effects on the structure and activity for Fischer-Tropsch and water-gas shift reactions of Co/Al2O3 catalysts.* Iranian Journal of Chemistry & Chemical Engineering-International English Edition, 2007. **26**(1): p. 9-16.
80. Xiong, H., et al., *Fischer–Tropsch synthesis: the effect of Al2O3 porosity on the performance of Co/Al2O3 catalyst.* Catalysis Communications, 2005. **6**(8): p. 512-516.
81. Zhang, Y., et al., *Effect of magnesia on alumina-supported cobalt Fischer–Tropsch synthesis catalysts.* Journal of Molecular Catalysis A: Chemical, 2005. **237**(1–2): p. 172-181.
82. Martínez, A.n., et al., *Fischer–Tropsch synthesis of hydrocarbons over mesoporous Co/SBA-15 catalysts: the influence of metal loading, cobalt precursor, and promoters.* Journal of Catalysis, 2003. **220**(2): p. 486-499.
83. Ma, C., et al., *Synthesis and application of γ-Al2O3 supported CoRu-based Fischer–Tropsch catalyst.* Chemical Engineering Journal, 2012. **191**(0): p. 534-540.
84. Li, C., et al., *Effects of Impregnation Solvents on Catalytic Performance of Co-Ru-ZrO2/γ-Al2O3 Catalyst for Fischer-Tropsch Synthesis.* Petroleum Science and Technology, 2008. **26**(6): p. 704-716.
85. Concepción, P., et al., *Characterization and catalytic properties of cobalt supported on delaminated ITQ-6 and ITQ-2 zeolites for the Fischer–Tropsch synthesis reaction.* Journal of Catalysis, 2004. **228**(2): p. 321-332.
86. den Breejen, J.P., et al., *Design of supported cobalt catalysts with maximum activity for the Fischer–Tropsch synthesis.* Journal of Catalysis, 2010. **270**(1): p. 146-152.
87. Girardon, J.S., et al., *Cobalt dispersion, reducibility, and surface sites in promoted silica-supported Fischer–Tropsch catalysts.* Journal of Catalysis, 2007. **248**(2): p. 143-157.
88. Girardon, J.-S., et al., *Effect of cobalt precursor and pretreatment conditions on the structure and catalytic performance of cobalt silica-supported Fischer–Tropsch catalysts.* Journal of Catalysis, 2005. **230**(2): p. 339-352.
89. Jung, J.-S., S.W. Kim, and D.J. Moon, *Fischer–Tropsch Synthesis over cobalt based catalyst supported on different mesoporous silica.* Catalysis Today, 2012. **185**(1): p. 168-174.
90. Ming, H. and B.G. Baker, *Characterization of cobalt Fischer-Tropsch catalysts I. Unpromoted cobalt-silica gel catalysts.* Applied Catalysis A: General, 1995. **123**(1): p. 23-36.
91. Sun, S., N. Tsubaki, and K. Fujimoto, *The reaction performances and characterization of Fischer–Tropsch synthesis Co/SiO2 catalysts prepared from mixed cobalt salts.* Applied Catalysis A: General, 2000. **202**(1): p. 121-131.
92. Yang, J.-I., et al., *Highly effective cobalt catalyst for wax production in Fischer–Tropsch synthesis.* Fuel, 2010. **89**(1): p. 237-243.

93. Lacroix, M., et al., *Silicon carbide foam composite containing cobalt as a highly selective and re-usable Fischer–Tropsch synthesis catalyst.* Applied Catalysis A: General, 2011. **397**(1–2): p. 62-72.
94. Lillebø, A., et al., *Fischer–Tropsch Synthesis on SiC-Supported Cobalt Catalysts.* Topics in Catalysis, 2013. **56**(9-10): p. 730-736.
95. Tavasoli, A., et al., *Fischer–Tropsch synthesis on mono- and bimetallic Co and Fe catalysts supported on carbon nanotubes.* Fuel Processing Technology, 2009. **90**(12): p. 1486-1494.
96. Calderone, V.R., et al., *De Novo Design of Nanostructured Iron–Cobalt Fischer–Tropsch Catalysts.* Angewandte Chemie International Edition, 2013. **52**(16): p. 4397-4401.
97. Morales, F., et al., *Effects of manganese oxide promoter on the CO and H2 adsorption properties of titania-supported cobalt Fischer–Tropsch catalysts.* Journal of Catalysis, 2007. **246**(1): p. 91-99.
98. Morales, F., et al., *X-ray Absorption Spectroscopy of Mn/Co/TiO2 Fischer−Tropsch Catalysts: Relationships between Preparation Method, Molecular Structure, and Catalyst Performance.* The Journal of Physical Chemistry B, 2006. **110**(17): p. 8626-8639.
99. Li, F., et al., *Combustion synthesis of γ-lithium aluminate by using various fuels.* Journal of Nuclear Materials, 2002. **300**(1): p. 82-88.
100. Toniolo, J.C., A.S. Takimi, and C.P. Bergmann, *Nanostructured cobalt oxides (Co3O4 and CoO) and metallic Co powders synthesized by the solution combustion method.* Materials Research Bulletin, 2010. **45**(6): p. 672-676.
101. Brownson, J.R.S. and C. Lévy-Clément, *Nanostructured α- and β-cobalt hydroxide thin films.* Electrochimica Acta, 2009. **54**(26): p. 6637-6644.
102. KelpŠAitĖ, I., J. BaltruŠAitis, and E. Valatka, *Electrochemical Deposition of Porous Cobalt Oxide Films on AISI 304 Type Steel.* Materials Science / Medziagotyra, 2011. **17**(3): p. 236-243.
103. Gupta, V., S. Gupta, and N. Miura, *Al-substituted α-cobalt hydroxide synthesized by potentiostatic deposition method as an electrode material for redox-supercapacitors.* Journal of Power Sources, 2008. **177**(2): p. 685-689.
104. Gupta, V., et al., *Potentiostatically deposited nanostructured α-Co(OH)2: A high performance electrode material for redox-capacitors.* Electrochemistry Communications, 2007. **9**(9): p. 2315-2319.
105. Eggenhuisen, T.M., et al., *Freeze-drying for controlled nanoparticle distribution in Co/SiO2 Fischer–Tropsch catalysts.* Journal of Catalysis, 2013. **297**(0): p. 306-313.
106. Fu, T., et al., *Fuel production through Fischer–Tropsch synthesis on carbon nanotubes supported Co catalyst prepared by plasma.* Fuel, 2014. **121**(0): p. 225-231.
107. Karimi, A., et al., *Functional group effect on carbon nanotube (CNT)-supported cobalt catalysts in Fischer–Tropsch synthesis activity, selectivity and stability.* Fuel, 2014. **117, Part B**(0): p. 1045-1051.
108. Trépanier, M., A.K. Dalai, and N. Abatzoglou, *Synthesis of CNT-supported cobalt nanoparticle catalysts using a microemulsion technique: Role of nanoparticle size on reducibility, activity and selectivity in Fischer–Tropsch reactions.* Applied Catalysis A: General, 2010. **374**(1–2): p. 79-86.
109. Santen, R.A.v., et al., *Mechanistic Issues in Fischer–Tropsch Catalysis.* Advances in Catalysis, 2011. **54**: p. 127-187.
110. Dry, M.E., *Practical and theoretical aspects of the catalytic Fischer-Tropsch process.* Applied Catalysis A: General, 1996. **138**(2): p. 319-344.
111. Fontenelle, A.B. and F.A.N. Fernandes, *Comprehensive Polymerization Model for Fischer-Tropsch Synthesis.* Chemical Engineering & Technology, 2011. **34**(6): p. 963-971.
112. Markvoort, A.J., et al., *Kinetics of the Fischer–Tropsch Reaction.* Angewandte Chemie, 2012. **124**(36): p. 9149-9153.
113. Yates, I.C. and C.N. Satterfield, *Intrinsic kinetics of the Fischer-Tropsch synthesis on a cobalt catalyst.* Energy & Fuels, 1991. **5**(1): p. 168-173.
114. Rapid Advanced Manufacturing (RapidMan) Limited. *3D Printing*. 2016; Available from: http://www.rapidman.co.nz/.

115. Landers, L.E., *Generating Fischer-Tropsch fuels using corrugated stainless steel mesh as a microchannel reactor*, 2013, University of Canterbury: Christchurch, New Zealand. p. 1-25.
116. Reijken, E., *Implementation of a Novel Plug Flow Reactor for Fischer-Tropsch Synthesis to generate Biofuels from the Gassification of Wood*, in *Department of Chemical and Process Engineering (UC) & Institute of Thermal Separation Processes (TUHH)*2014, University of Canterbury (UC) & Hamburg University of Technology (TUHH).

15.0. Appendices

Appendix A – Balanced Valencies method for Combustion Synthesis Solution

Theory for balanced valencies comes from propellant chemistry and is somewhat similar to the oxidation states of the elemental species within the molecules. Table A1 shows the valencies of the species occurring in the combustion synthesis solution:

Table A1: Valencies of species for balancing

Species	Valence
Carbon (C)	+4
Nitrogen (N)	±0
Hydrogen (H)	+1
Oxygen (O)	-2
Cobalt II (Co^{2+})	+2

Applying these to the molecular species in the reaction solution:

$$Co(NO_3)_2 \cdot 6H_2O = Co^{2+} + 2(N + 3O) + 6(2H + O)$$
$$= +2 + 2(\pm 0 - 6) + 6(2 - 2)$$
$$= -10$$

$$(NH_2)_2CO = 2(N\ +\ 2H) + C + O$$
$$= 2(\pm 0 + 2) + 4 - 2$$
$$= +6$$

Balancing these species:

$$1\ CO(NO_3) + n\ (NH_2)_2CO = 0$$
$$\rightarrow \quad -10 + 6n = 0$$
$$\rightarrow \quad n = 10/6 = 5/3$$

Therefore at a 2:1 excess 10/3 or 3 1/3 moles of urea is required per mole of $Co(NO_3)_2 \cdot 6H_2O$. Given a single preparation of the standard washcoating solution used contained 5g of $Co(NO_3)_2 \cdot 6H_2O$ the combustion synthesis solution should contain:

$$\frac{5\ g\ Co(NO_3)_2 \cdot 6H_2O}{291\ \frac{g}{mol}} = 0.0172\ mol\ Co(NO_3)_2 \cdot 6H_2O$$

$$\rightarrow \frac{10}{3} \times 0.0172 = 0.0572$$

$$\rightarrow 0.0572\ mol\ Urea \times 60\ \frac{g}{mol} = 3.436\ g\ Urea$$

Appendix B – Process Flow Diagrams

Original PFD with support channel reactor

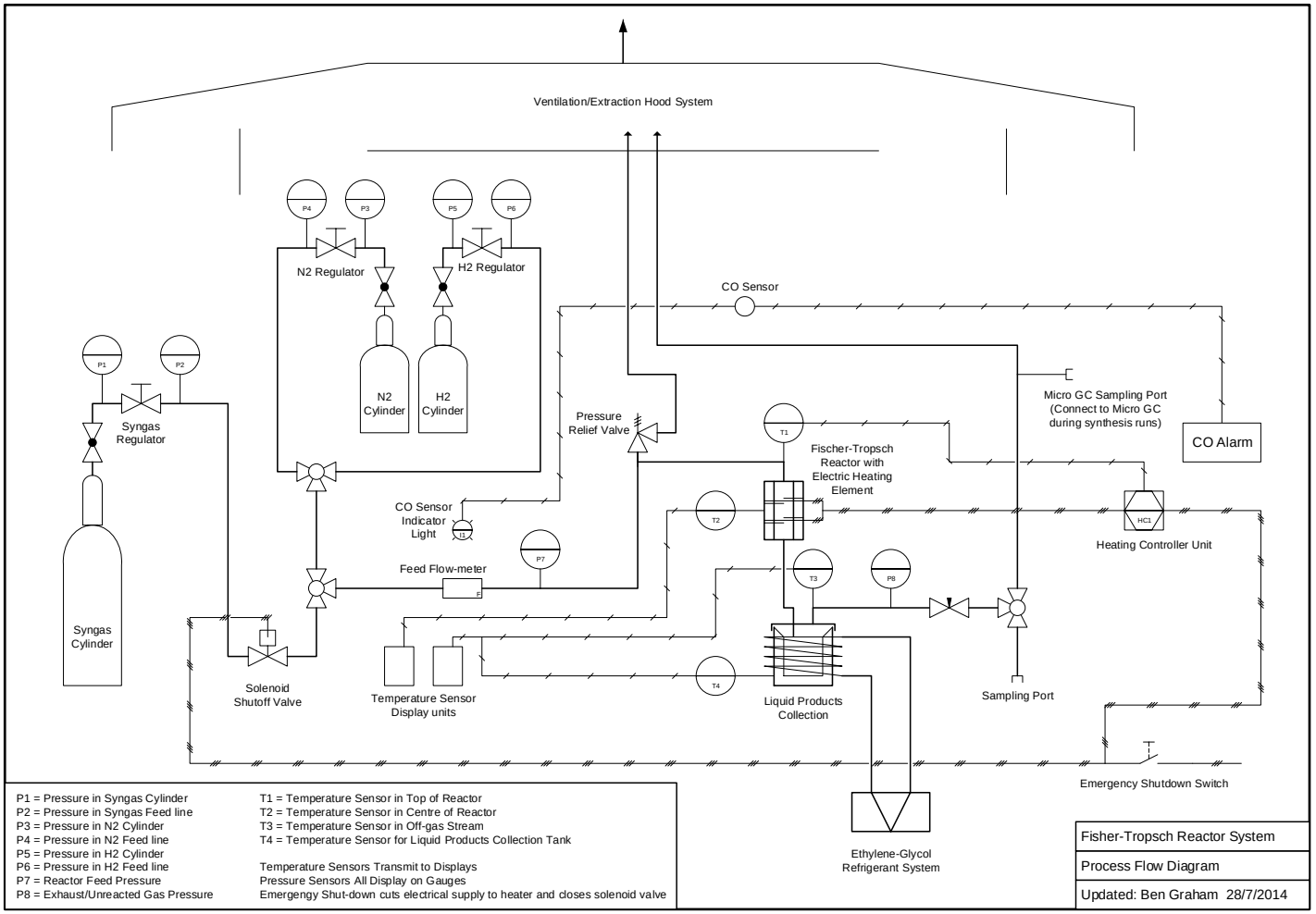

Updated PFD using Microchannel Reactor

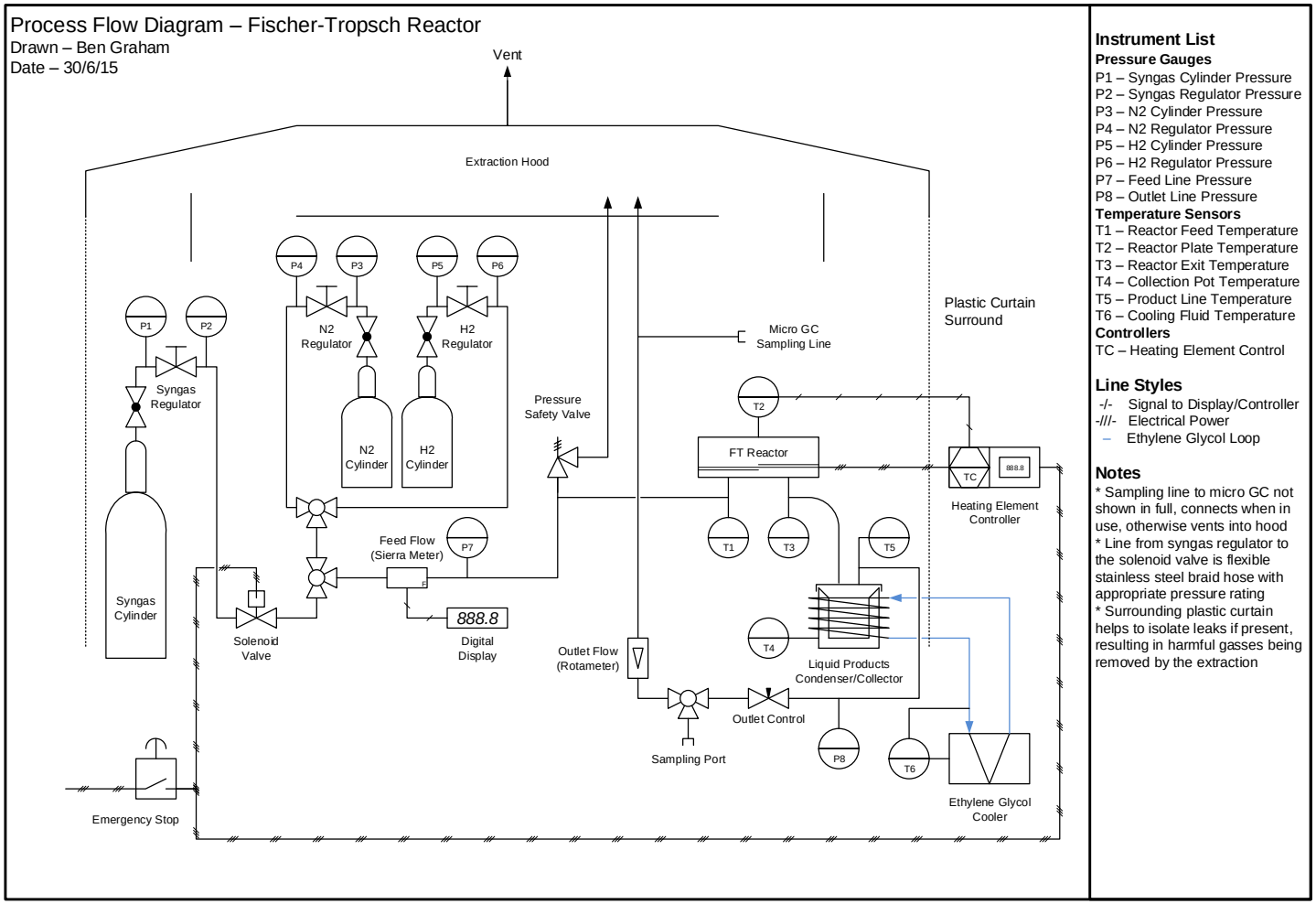

Instrument List

Pressure Gauges
P1 – Syngas Cylinder Pressure
P2 – Syngas Regulator Pressure
P3 – N2 Cylinder Pressure
P4 – N2 Regulator Pressure
P5 – H2 Cylinder Pressure
P6 – H2 Regulator Pressure
P7 – Feed Line Pressure
P8 – Outlet Line Pressure

Temperature Sensors
T1 – Reactor Feed Temperature
T2 – Reactor Plate Temperature
T3 – Reactor Exit Temperature
T4 – Collection Pot Temperature
T5 – Product Line Temperature
T6 – Cooling Fluid Temperature

Controllers
TC – Heating Element Control

Line Styles
-/- Signal to Display/Controller
-///- Electrical Power
– Ethylene Glycol Loop

Notes
* Sampling line to micro GC not shown in full, connects when in use, otherwise vents into hood
* Line from syngas regulator to the solenoid valve is flexible stainless steel braid hose with appropriate pressure rating
* Surrounding plastic curtain helps to isolate leaks if present, resulting in harmful gasses being removed by the extraction

Appendix C – Liquid Products GC Analysis Procedure

Sample Preparation

Liquid samples containing C_{6+} hydrocarbons were analysed post run using a Varian CP3800 gas chromatograph using a Varian Factor Four capillary column (30 m x 0.25 mm ID). Hexane was used as the carrier solvent both as a means of dissolving the waxes and diluting the products to a suitable level for good peak resolution. Typically 2-3 mL of hexane was used to dissolve the products in the collection vial. This mixture was then centrifuged to fully separate the polar and non-polar phases and any particles. Following centrifugation, the non-polar phase was extracted by syringe to provide the product for analysis. From the extracted product, 500 μL was sampled and diluted with 1 mL of hexane to create the sample stock solution. To create each of the three analysis samples 150 μL of the sample stock was mixed with a further 1.5 mL of hexane. The excess of hexane prevented the detection products lighter than C_9 as the peaks were masked however the peaks beyond that range are sufficient to establish an ASF distribution.

The GC operation method utilises the conditions listed below and in Table C1.

Injector Temperature: 300 °C

Detector: FID

Split Ratio: Splitless injection, split ratio 5 after 2 minutes

Injection Volume: 1.0 μL

Table C1: Oven Operating Temperatures and Ramping

Temperature °C	Ramp Rate °C·min^{-1}	Hold Time min	Total Time min
35	0	5	5
180	15	0	15
280	30	12	30

Calibration

The GC calibration data for analysing the samples was collected using an aliphatic hydrocarbon standard from Restek (CAT. Number 31459). It consisted of a range of 14 linear alkanes from C_9 to C_{36} at a concentration of 1000 μg/mL in hexane. This was diluted to the range of concentrations given in Table C2 to form calibration curves for each compound. The standard does not contain alkenes which are readily produced by the Fischer-Tropsch synthesis however since the target use is a fuel the distribution of product weight is more important than the alkene/alkane ratio. A peak identification solution was also prepared by adding 40 μL of dodecane (C_{12}) to 1.7 mL of hexane so that a reference peak could be used to identify the peaks in the results.

Table C2: Component concentrations and dilution recipies used for the GC calibration solutions

Solution Name	Description	Conc. mg/mL
Stock	500 μL of Standard in 1.2 mL of Hexane	0.294
Cal. #1	500 μL of Stock in 1.2 mL of Hexane	0.087
Cal. #2	300 μL of Stock in 1.4 mL of Hexane	0.052
Cal. #3	200 μL of Stock in 1.5 mL of Hexane	0.035
Cal. #4	100 μL of Stock in 1.6 mL of Hexane	0.017
Cal. #5	50 μL of Stock in 1.6 mL of Hexane	0.009

Appendix D – Reactor Costing Tables

The tables below outline the costs of manufacturing the microchannel plate reactors. Electronic discharge machining (EDM) is used to produce the cuts in the shim plates used for the inner layers while the cover plates are machined conventionally. The costs of a cooling layer are estimated based on the cost of the distribution layers to attain a similar cut length.

Table D1: Original 0.3 mm microchannel plates

OLD PLATES	EX GST	INC GST	COMMENT
Fittings	$ 20.00	$ 23.00	Four ports
Cover Plates	$ 58.86	$ 67.69	
Channels	$ 32.00	$ 36.80	per plate
Cooling	$ 10.00	$ 11.50	per plate
Distribution	$ 5.00	$ 5.75	per plate
Gaskets	$ 0.02	$ 0.02	per gasket
Single Layer	$ 130.88	$ 150.51	Whole Reactor
5 Layers	$ 338.96	$ 389.80	
10 Layers	$ 599.06	$ 688.92	

Table D2: Recommended 0.9 mm long microchannel plates

OLD PLATES	EX GST	INC GST	COMMENT
Fittings	$ 20.00	$ 23.00	Four ports
Cover Plates	$ 104.85	$ 120.58	
Channels	$ 165.92	$ 190.81	per plate
Cooling	$ 26.57	$ 30.56	per plate
Distribution	$ 13.29	$ 15.28	per plate
Gaskets	$ 0.05	$ 0.06	per gasket
Single Layer	$ 343.96	$ 395.55	Whole Reactor
5 Layers	$ 1,220.40	$ 1,403.46	
10 Layers	$ 2,315.96	$ 2,663.35	

Appendix E: Matlab function for numerical model

This section contains the two functions used to run the numerical model of the system using the computer software package Matlab. The main operations are carried out in the file FTsize which is called as a function using the script file FTsystem which can be used to adjust the input parameters. The notation used in the files is given in Table E1.

Table E1: Matlab script and function notation

VARIABLE	TYPE	PROPERTY REPRESENTED
Xt	Input	Target CO conversion to achieve
V	Input	Feed synthesis gas flowrate in SCCM
alpha	fixed	ASF distribution α parameter from experimental data
dL	fixed	Incremental length change along the reactor channel
Layers	Input	Number of layers of channel plates used
L	Output	Length of reactor (mm) required to achieve Xt
Pt	Fixed	Reactor Pressure (MPa)
wchan	Fixed	Channel width (m) of the microchannels
dchan	Fixed	Depth of the microchannels (m) = plate thickness
nchan	Fixed	Number of channels per plate
nplates	Holding	Holder of value from Layers
yCO	Fixed	CO concentration (mol%) in feed
yH2	Fixed	H_2 concentration (mol%) in feed
yN2	Fixed	N_2 concentration (mol%) in feed
A	Fixed	H_2 to CO consumption ratio from experimental data
n	Fixed	ASF average hydrocarbon chain length
PCO	Calculated	Partial Pressure of CO (MPa)
PH2	Calculated	Partial Pressure of H_2 (MPa)
PN2	Calculated	Partial Pressure of N_2 (MPa)
PProd	Calculated	Partial Pressure of hydrocarbon product (MPa)
PWater	Calculated	Partial Pressure of water (MPa)
Fin	Calculated	Molar feed flowrate (mol/s) calculated by ideal gas law
COfeed	Holding	CO molar flow entering the reactor (mol/s)
H2feed	Holding	H_2 molar flow entering the reactor (mol/s)
FN2	Calculated	Flow of N_2 through the system (mol/s)
Prodin	Calculated	Hydrocarbon entering the system/increment (mol/s)
H2Oin	Calculated	Water entering the system/increment (mol/s)
dV	Calculated	Volume change increment (m^3)
COin	Calculated	CO molar flow entering the increment (mol/s)
H2in	Calculated	H_2 molar flow entering the increment (mol/s)

VARIABLE	TYPE	PROPERTY REPRESENTED
rCO	Calculated	Rate of consumption of CO in the reactor (mol/m^3/s)
rH2	Calculated	Rate of consumption of CO in the reactor (mol/m^3/s)
rProd	Calculated	Rate of generation of product in the reactor (mol/m^3/s)
rH2O	Calculated	Rate of generation of water in the reactor (mol/m^3/s)
FCO	Calculated	CO flow out of the increment (mol/s)
FH2	Calculated	H_2 flow out of the increment (mol/s)
FProd	Calculated	Product flow out of the increment (mol/s)
FH2O	Calculated	Water flow out of the increment (mol/s)
Ft	Calculated	Total flow out of the increment (mol/s)
Xc	Calculated	CO molar conversion (%)
Xh	Calculated	H_2 molar conversion (%)

Function 1: FT System

```
% FTsystem
% Written by: Ben Graham
% Last Updated: 20 March 2016

% Clearing
clear,clc,clf;

% Set Fixed Parameters
Xt = 80;          % Target CO conversion (%) (max may be < 100)
V = 39.95;        % Standard volumetric feed flow (SCCM)
alpha = 0.795;    % ASF distribution parameter

% modifiers
dL = 0.0001;   % length increment (m)
Layers = 1;    % number of layers of reactor channel

% Function 1 - Reactor size
fprintf('CO Conversion\n')
display(Xt)

L = FTSize(Xt,V,dL,Layers);  % length of reactor to achieve desired
                               conversion XT
fprintf('Length in mm\n')
display(L)
```

Function 2: FTsize

```
function Length = FTSize(Xt,V,dL,Layers)

% Calculates the required length (L) in meters of the FT microchannels to
% attain a specified conversion (Xt) of CO with length step (dL)
% Written: Ben Graham
% Last edited: 20 March 2016

% Fixed Variables
Pt = 2;              % Total Pressure (MPa = bar/10)
wchan = 0.0009;      % Adjust >> width in m of channels
dchan = 0.0003;      % depth of channels in m
nchan = 25;          % Adjust >> number of channels
nplates = Layers;    % number of plates
yCO = 0.2940;        % Molar Fraction of CO in syngas cylinder
yH2 = 0.6691;        % Molar Fraction of H2 in syngas cylinder
yN2 = 1-yCO-yH2;     % Molar Fraction of N2 in syngas cylinder

A = 2.29;            % H2 to CO consumption ratio (2.29)
n = 8.75;            % Mean hydrocarbon chain length (8.75)

PCO(1) = yCO*Pt;        % Initial Partial Pressure of CO
PH2(1) = yH2*Pt;        % Initial Partial Pressure of H2
PN2(1) = yN2*Pt;        % Partial Pressure of N2 (Constant)
PProd(1) = 0;           % Initial Partial Pressure of Hydrocarbon Products
PWater(1) = 0;          % Initial partial Pressure of Water

S = 100000;          % Array size

% Initial Flow Rates
Fin = 101325*(V/1000000/60)/8.314/298; % Feed flowrate (mol/s)
COfeed = yCO*Fin;
H2feed = yH2*Fin;
FN2 = Fin*yN2;
Prodin = 0;
H2Oin = 0;

% Preallocating Arrays for the calculations (supress if plotting)
% rCO = zeros(S,1);
% rH2 = zeros(S,1);
% rProd = zeros(S,1);
% rH2O = zeros(S,1);
% FCO = zeros(S,1);
% FH2 = zeros(S,1);
% FProd = zeros(S,1);
% FH2O = zeros(S,1);
% X = zeros(S,1);
% L = zeros(S,1);

% Step change in volume
dV = dL*wchan*dchan*nchan*nplates;

for I = 1:S

if I < 2
COin = COfeed;
H2in = H2feed;
end
```

```
% Calculating the rates of reaction (mol/m³/s)
rCO(I) = 3098*PCO(I)*PH2(I)/((1+21.86*PCO(I))^2);  % CO consumption rate
rH2(I) = A*rCO(I);                                  % H2 consumption rate
rProd(I) = 1/n*rCO(I);                           % Product generation rate
rH2O(I) = rCO(I);                                % H2O generation rate

% Solving the differential equations
FCO(I) = COin - rCO(I)*dV;                    % balance of CO
FH2(I) = H2in - rH2(I)*dV;                    % balance of H2
FProd(I) = Prodin + rProd(I)*dV;              % balance of hydrocarbons
FH2O(I) = H2Oin + rH2O(I)*dV;                 % balance of H2O
Ft(I) = FCO(I)+FH2(I)+FProd(I)+FH2O(I)+FN2; % calculating the total flow

% Calculating the conversion
Xc(I) = (1-(FCO(I)/COfeed))*100;              % Xc is %CO conversion
Xh(I) = (1-(FH2(I)/H2feed))*100;              % Xh is %H2 conversion

% Calculating the reactor length
L(I) = dL*I*1000;



% Stop Condition for achieving the desired conversion
if Xc(I) > Xt
break
end

% looping the iteration to set the values for the start of the next segment
COin = FCO(I);
H2in = FH2(I);
Prodin = FProd(I);
H2Oin = FH2O(I);
PCO(I+1) = FCO(I)*Pt/Ft(I);
PH2(I+1) = FH2(I)*Pt/Ft(I);
PN2(I+1) = PN2(1);
PProd(I+1) = FProd(I)*Pt/Ft(I);
PWater(I+1) = FH2O(I)*Pt/Ft(I);
% Partial pressure calculations run under the experimental situation where
% the total pressure remains 2.0MPa despite the calculation here indicating
% diminishing pressure due to fewer moles of gas after reaction.

end                                           % End the iterations

Length = L(I);
% Plotting
% Use figure(a) to plot in separate figures with number a
% Use subplot(x,y,p) to plot together in a grid of x,y and position p

figure(1)
set(gcf,'color',[1 1 1])  % white background around figures
set(gca,'fontsize',24)    % setting the graph font size
% subplot(2,2,1)
plot(L,FCO,'b-',L,FH2,'r-',L,FProd,'g-',L,FH2O,'c-')
xlabel('Reactor Channel Length (mm)')
ylabel('Species Molar Flow (mol/s)')
legend('CO','H2','Prods','Water','Location','NorthEast')
```

```
figure(2)
set(gcf,'color',[1 1 1])  % white background around figures
set(gca,'fontsize',24)    % setting the graph font size
% subplot(2,2,2)
plot(L,PCO,'b-',L,PH2,'r-',L,PProd,'g-',L,PWater,'c-',L,PN2,'k-')
set(gca,'YGrid','on')
xlabel('Reactor Channel Length (mm)')
ylabel('Species Partial Pressure (MPa)')
legend('CO','H2','Prods','Water','N2','Location','NorthEast')

figure(3)
set(gcf,'color',[1 1 1])  % white background around figures
set(gca,'fontsize',24)    % setting the graph font size
% subplot(2,2,3)
plot(L,rCO,'b-',L,rH2,'r-')
xlabel('Reactor Channel Length (mm)')
ylabel('Reactant Consumption Rate (mol/m^3/s)')
legend('CO','H2','Location','East')

figure(4)
set(gcf,'color',[1 1 1])  % white background around figures
set(gca,'fontsize',24)    % setting the graph font size
% subplot(2,2,4)
plot(L,Xc,'b-',L,Xh,'r-')
set(gca,'YGrid','on')
xlabel('Reactor Channel Length (mm)')
ylabel('Reactant Conversion (mol %)')
legend('CO','H2','Location','East')

end                                          % End the Function
```